The Astrophysical Journal Supplement Series, 220:9 (35pp), 2015 September doi:10.1088/0067-0049/220/1/9

CFAIR2: NEAR-INFRARED LIGHT CURVES OF 94 TYPE Ia SUPERNOVAE

Andrew S. Friedman[1,2], W. M. Wood-Vasey[3], G. H. Marion[1,4], Peter Challis[1], Kaisey S. Mandel[1], Joshua S. Bloom[5], Maryam Modjaz[6], Gautham Narayan[1,7,8], Malcolm Hicken[1], Ryan J. Foley[9,10], Christopher R. Klein[5], Dan L. Starr[5], Adam Morgan[5], Armin Rest[11], Cullen H. Blake[12], Adam A. Miller[13,15], Emilio E. Falco[1], William F. Wyatt[1], Jessica Mink[1], Michael F. Skrutskie[14], and Robert P. Kirshner[1]

[1] Harvard-Smithsonian Center for Astrophysics, 60 Garden Street, Cambridge, MA 02138, USA; asf@mit.edu, pchallis@cfa.harvard.edu, kmandel@cfa.harvard.edu, gnarayan@noao.edu, malcolmhicken@hotmail.com, efalco@cfa.harvard.edu, wfw781kra@gmail.com, jmink@cfa.harvard.edu, rkirshner@cfa.harvard.edu
[2] Center for Theoretical Physics and Department of Physics, Massachusetts Institute of Technology, Cambridge, MA 02139, USA
[3] Department of Physics and Astronomy, University of Pittsburgh, 100 Allen Hall, 3941 O'Hara Street Pittsburgh, PA 15260, USA; wmwv@pitt.edu
[4] Astronomy Department, University of Texas at Austin, Austin, TX 78712, USA; hman@astro.as.utexas.edu
[5] Department of Astronomy, University of California Berkeley, Berkeley, CA 94720, USA; joshbloom@berkeley.edu, cklein@berkeley.edu, dstarr1@gmail.com, amorgan@astro.berkeley.edu
[6] Center for Cosmology and Particle Physics, New York University, Meyer Hall of Physics, 4 Washington Place, Room 529, New York, NY 10003, USA; mmodjaz@nyu.edu
[7] Physics Department, Harvard University, 17 Oxford Street, Cambridge, MA 02138, USA
[8] National Optical Astronomy Observatory, 950 N. Cherry Avenue, Tucson, AZ 85719, USA
[9] Department of Astronomy, University of Illinois at Urbana-Champaign, 1002 W. Green Street, Urbana, IL 61801, USA; rfoley@illinois.edu
[10] Department of Physics, University of Illinois at Urbana-Champaign, 1110 W. Green Street, Urbana, IL 61801, USA
[11] Space Telescope Science Institute, STScI, 3700 San Martin Drive, Baltimore, MD 21218, USA; arest@stsci.edu
[12] University of Pennsylvania, Department of Physics and Astronomy, 209 South 33rd Street, Philadelphia, PA 19104, USA; chblake@sas.upenn.edu
[13] Jet Propulsion Laboratory, California Institute of Technology, Pasadena, CA 91125, USA; amiller@astro.caltech.edu
[14] Department of Astronomy, P.O. Box 400325, 530 McCormick Road, Charlottesville, VA 22904, USA; skrutskie@virginia.edu
Received 2014 August 1; accepted 2015 February 20; published 2015 September 4

ABSTRACT

CfAIR2 is a large, homogeneously reduced set of near-infrared (NIR) light curves (LCs) for Type Ia supernovae (SNe Ia) obtained with the 1.3 m Peters Automated InfraRed Imaging TELescope. This data set includes 4637 measurements of 94 SNe Ia and 4 additional SNe Iax observed from 2005 to 2011 at the Fred Lawrence Whipple Observatory on Mount Hopkins, Arizona. CfAIR2 includes JHK_s photometric measurements for 88 normal and 6 spectroscopically peculiar SN Ia in the nearby universe, with a median redshift of $z \sim 0.021$ for the normal SN Ia. CfAIR2 data span the range from −13 days to +127 days from B-band maximum. More than half of the LCs begin before the time of maximum, and the coverage typically contains ∼13–18 epochs of observation, depending on the filter. We present extensive tests that verify the fidelity of the CfAIR2 data pipeline, including comparison to the excellent data of the Carnegie Supernova Project. CfAIR2 contributes to a firm local anchor for SN cosmology studies in the NIR. Because SN Ia are more nearly standard candles in the NIR and are less vulnerable to the vexing problems of extinction by dust, CfAIR2 will help the SN cosmology community develop more precise and accurate extragalactic distance probes to improve our knowledge of cosmological parameters, including dark energy and its potential time variation.

Key words: cosmology: observations – distance scale – infrared: stars – supernovae: general – techniques: image processing – techniques: photometric

Supporting material: machine-readable tables

1. INTRODUCTION

Optical observations of Type Ia Supernovae (SN Ia) were crucial to the surprising 1998 discovery of the acceleration of cosmic expansion (Riess et al. 1998; Schmidt et al. 1998; Perlmutter et al. 1999). Since then, several independent cosmological techniques have confirmed the SN Ia results (see Frieman et al. 2008a; Weinberg et al. 2013 for reviews), while SN Ia provide increasingly accurate and precise measurements of extragalactic distances and dark energy (see Kirshner 2010, 2013; Goobar & Leibundgut 2011 for reviews). Increasing evidence suggests that SN Ia observations at rest-frame near-infrared (NIR) wavelengths yield more accurate and more precise distance estimates to SN Ia host galaxies than optical data alone (Krisciunas et al. 2004b, 2007; Wood-Vasey et al. 2008; Mandel et al. 2009, 2011, 2014; Contreras et al. 2010; Folatelli et al. 2010; Burns et al. 2011, 2014; Stritzinger et al. 2011; Barone-Nugent et al. 2012; Kattner et al. 2012; Phillips 2012; Weyant et al. 2014).

This work presents CfAIR2, a densely sampled, low-redshift photometric data set including 94 SN Ia NIR JHK_s-band light curves (LCs) observed from 2005 to 2011 with the f/13.5 Peters Automated InfraRed Imaging TELescope (PAIRITEL) 1.3 m telescope at the Fred Lawrence Whipple Observatory (FLWO) on Mount Hopkins, Arizona. Combining low-redshift NIR SN Ia data sets like CfAIR2 with higher-redshift samples will play a crucial role in ongoing and future SN cosmology experiments, from the ground and from space, which hope to reveal whether dark energy behaves like Einstein's cosmological constant Λ or some other phenomenon that may vary over cosmic history.

While SN Ia observed at optical wavelengths have been shown to be excellent *standardizeable* candles using a variety of sophisticated methods correlating luminosity with LC shape and color, SN Ia are very nearly *standard* candles at NIR

[15] Hubble Fellow.

wavelengths, even before correction for LC shape or reddening (e.g., Wood-Vasey et al. 2008; Kattner et al. 2012; hereafter WV08 and K12). Compared to the optical, SN Ia in the NIR are both better standard candles and relatively immune to the effects of extinction and reddening by dust. Systematic distance errors from photometric calibration uncertainties, uncertain dust estimates, and intrinsic variability of un-reddened SN Ia colors are outstanding problems with using SN Ia for precise cosmological measurements of dark energy with optical data alone (Wang et al. 2006; Conley et al. 2007, 2011; Guy et al. 2007, 2010; Jha et al. 2007; Wood-Vasey et al. 2007; Hicken et al. 2009a; Kessler et al. 2009; Campbell et al. 2013; Narayan 2013; Betoule et al. 2014; Rest et al. 2014; Scolnic et al. 2014a, 2014b). By contrast, many of the systematic uncertainties and discrepancies between the most prominent optical LC fitting and distance estimation methods are avoided with the incorporation of NIR data (Mandel et al. 2011; hereafter M11; Folatelli et al. 2010; Burns et al. 2011; K12; Mandel et al. 2014). The most promising route toward understanding the dust in other galaxies and mitigating systematic distance errors in SN cosmology comes from NIR observations.

CfAIR2 JHK_s observations with PAIRITEL are part of a systematic multiwavelength program of CfA SN observations at FLWO. We follow up nearby SN as they are discovered to obtain densely sampled, high signal-to-noise ratio (S/N) optical and NIR LCs of hundreds of nearby low-redshift SN in $UBVRIr'i'JHK_s$. Whenever possible, PAIRITEL NIR data were observed for targets with additional optical photometry at the FLWO 1.2 m, optical spectroscopy at the 1.5 m Tillinghast telescope with the FAST spectrograph, and/or late-time spectroscopy at the MMT (Matheson et al. 2008; Hicken 2009; Hicken et al. 2009b, 2012; Blondin et al. 2012). By obtaining concurrent optical photometry and spectroscopy for many objects observed with PAIRITEL, we considerably increase the value of the CfAIR2 data set. Of the 98 CfAIR2 objects, 92 have complementary optical observations from the CfA or other groups, including unpublished data.[16] Table 1 lists general properties of the 94 SN Ia.

It has only recently become understood that SN 2002cx-like objects, which we categorize as SN Iax (e.g., Foley et al. 2013), are significantly distinct from both normal SN Ia and spectroscopically peculiar SN Ia (Li et al. 2003; Branch et al. 2004; Chornock et al. 2006; Jha et al. 2006a; Phillips et al. 2007; Sahu et al. 2008; Foley et al. 2009, 2010a, 2010b, 2013, 2014a, 2014b, 2015; Maund et al. 2010; McClelland et al. 2010; Narayan et al. 2011; Kromer et al. 2013; McCully et al. 2014b, 2014a; Stritzinger et al. 2015). Throughout, we treat the four SN Iax included in CfAIR2 (SN 2005hk, SN 2008A, SN 2008ae, SN 2008ha) as a separate class of objects from SN Ia (see Table 2).

This work is a report on photometric data from PAIRITEL, which improves upon and supersedes a previously published subset including 20 SN Ia JHK_s LCs from WV08 (implicitly "CfAIR1"), 1 SN Iax LC from WV08 (SN 2005hk), and 1 SN Iax LC from Foley et al. (2009) (SN 2008ha), along with work presented in Friedman (2012, hereafter F12).[17] Data points for these 20 objects have been reprocessed using our newest mosaic and photometry pipelines and are presented as part of this CfAIR2 data release. The CfAIR1 (WV08) and CfAIR2 NIR data sets complement previous CfA optical studies of SN Ia (CfA1: Riess et al. 1999; CfA2: Jha et al. 2006b; CfA3: Hicken et al. 2009b; and CfA4: Hicken et al. 2012) and CfA5 (to be presented elsewhere). CfA5 will include optical data for at least 15 CfAIR2 objects and additional optical LCs for non-CfAIR2 objects.

The 4637 individual CfAIR2 JHK_s data points represent the largest homogeneously observed and reduced set of NIR SN Ia and SN Iax observations to date. Simultaneous JHK_s observing provided nightly cadence for the most densely sampled LCs and extensive time coverage, ranging from 13 days before to 127 days after the time of B-band maximum brightness ($t_{B\,\max}$). CfAIR2 data have means of 18, 17, and 13 observed epochs for each LC in JHK_s, respectively, as well as 46 epochs for the most extensively sampled LC. CfAIR2 LCs have significant early-time coverage. Out of 98 CfAIR2 objects, 55% have NIR observations before $t_{B\,\max}$, while 34% have observations at least 5 days before $t_{B\,\max}$. The highest-S/N LC points for each CfAIR2 object have median uncertainties of $\sim$0.032, 0.053, and 0.115 mag in JHK_s, respectively. The median uncertainties of all CfAIR2 LC points are 0.086, 0.122, and 0.175 mag in JHK_s, respectively.

Of the 98 CfAIR2 objects, 88 are spectroscopically normal SN Ia and 86 will be useful for SN cosmology (SN 2006E and SN 2006mq were discovered late and lack precise $t_{B\,\max}$ estimates). The six spectroscopically peculiar SN Ia and four SN Iax are not standardizable candles using existing LC fitting techniques and currently must be excluded from Hubble diagrams.

1.1. Previous Results with NIR SN Ia

For optical SN Ia LCs, many sophisticated methods are used to reduced the scatter in distance estimates. These include $\Delta m_{15}(B)$ (Phillips 1993; Hamuy et al. 1996; Phillips et al. 1999; Prieto et al. 2006), multicolor LC shape (Riess et al. 1996, 1998; Jha et al. 2006b, 2007), "stretch" (Perlmutter et al. 1997; Goldhaber et al. 2001), Bayesian Adapted Template Match (Tonry et al. 2003), color–magnitude intercept calibration (Wang et al. 2003), spectral adaptive template (Guy et al. 2005, 2007; Astier et al. 2006), empirical methods (e.g., SiFTO; Conley et al. 2008), and `BayeSN`, a novel hierarchical Bayesian method developed at the CfA (M09, M11).

Unlike optical SN Ia, which are *standardizable* candles after a great deal of effort, spectroscopically normal NIR SN Ia appear to be nearly *standard* candles at the ~0.15–0.2 mag level or better, depending on the filter (Meikle 2000; Krisciunas et al. 2004a, 2005a, 2007; Folatelli et al. 2010; Burns et al. 2011; Phillips 2012; WV08; M09; M11). Overall, SN Ia are superior standard candles and distance indicators in the NIR compared to optical wavelengths, with a narrow distribution of peak JHK_s magnitudes and ~5–11 times less sensitivity to reddening than optical B-band data alone.

[16] All 10 spectroscopically peculiar SN Ia and SN Iax have optical data from the CfA or other groups, including unpublished CfA5 optical data. Of the 88 spectroscopically normal CfAIR2 SN Ia in Table 1, 64 have published optical data from the CfA or other groups, and 12 have unpublished CfA5 optical data. An additional four have CfA optical observations but no successfully reduced LCs yet: SN 2010jv, SN 2010ex, SN 2010ew, SN 2009fw. In addition, two objects have unpublished optical data from other groups, PTF10icb (PTF: Parrent et al. 2011: only spectra included), and PTF10bjs (PTF, CfA4: only natural system $r'i'$). Six objects currently have no optical photometry, according to our search of the literature: SN 2010dl, SN 2009im, SN 2008hy, SN 2008fx, SN 2005ch, SN 2005ao.

[17] F12 PDF available at http://search.proquest.com/docview/1027769281.

Table 1
General Properties of 94 PAIRITEL SN Ia

SN Name	R.A.[a] α(2000)	Decl.[a] δ(2000)	Host[b] Galaxy	Morphology[c]	$z_{\rm helio}$[d]	$\sigma_{z_{\rm helio}}$[d]	z[d] Ref.	Discovery[b] Reference	Discoverer(s)[e]	Type[f] Reference	Type[g]
SN 2005ao	266.20653	61.90786	NGC 6462	SABbc	0.038407	0.000417	1	CBET 115	POSS	IAUC 8492	Ia
SN 2005bl	181.05098	20.40683	NGC 4070	···	0.02406	0.00008	1	IAUC 8515	LOSS, POSS	IAUC 8514	Iap
SN 2005bo	192.42099	−11.09663	NGC 4708	SA(r)ab pec?	0.013896	0.000027	1	CBET 141	POSS	CBET 142	Ia
SN 2005cf	230.38906	−7.44874	MCG −01-39-3	S0 pec	0.006461	0.000037	1	CBET 158	LOSS	IAUC 8534	Ia
SN 2005ch	215.52815	1.99316	1	···	0.027	0.005	3	CBET 166	ROTSE-III	CBET 167	Ia
SN 2005el	77.95316	5.19417	NGC 1819	SB0	0.01491	0.000017	1	CBET 233	LOSS	CBET 235	Ia
SN 2005eq.	47.20575	−7.03332	MCG −01-9-6	SB(rs)cd?	0.028977	0.000073	1	IAUC 8608	LOSS	IAUC 8610	Ia
SN 2005eu	36.93011	28.17698	2	···	0.03412	0.000046	1	CBET 242	LOSS	CBET 244	Ia
SN 2005iq	359.63517	−18.70914	MCG −03-1-8	Sa	0.034044	0.000123	1	IAUC 8628	LOSS	CBET 278	Ia
SN 2005ke	53.76810	−24.94412	NGC 1371	(R')SAB(r'l)a	0.00488	0.000007	1	IAUC 8630	LOSS	IAUC 8631	Iap
SN 2005ls	43.56630	42.72480	MCG +07-7-1	Spiral	0.021118	0.000117	1	IAUC 8643	Armstrong	CBET 324	Ia
SN 2005na	105.40287	14.13304	UGC 3634	SB(r)a	0.026322	0.000083	1	CBET 350	POSS	CBET 351	Ia
SN 2006D	193.14111	−9.77519	MCG −01-33-34	SAB(s)ab pec?	0.008526	0.000017	1	CBET 362	BRASS	CBET 366	Ia
SN 2006E	208.36880	5.20619	NGC 5338	SB0	0.002686	0.000005	2	CBET 363	POSS, LOSS, CROSS	ATEL 690	Ia
SN 2006N	92.13021	64.72362	MCG +11-8-12	···	0.014277	0.000083	1	CBET 375	Armstrong	IAUC 8661	Ia
SN 2006X	185.72471	15.80888	NGC 4321	SAB(s)bc	0.00524	0.000003	1	IAUC 8667	Suzuki, CROSS	CBET 393	Ia
SN 2006ac	190.43708	35.06872	NGC 4619	SB(r)b pec?	0.023106	0.000037	1	IAUC 8669	LOSS	CBET 398	Ia
SN 2006ax	171.01434	−12.29156	NGC 3663	SA(rs)bc pec	0.016725	0.000019	2	CBET 435	LOSS	CBET 437	Ia
SN 2006cp	184.81198	22.42723	UGC 7357	SAB(s)c	0.022289	0.000002	1	CBET 524	LOSS	CBET 528	Ia
SN 2006cz	222.15254	−4.74193	MCG −01-38-2	SA(s)cd?	0.0418	0.000213	1	IAUC 8721	LOSS	CBET 550	Ia
SN 2006gr	338.09445	30.82871	UGC 12071	SBb	0.034597	0.00003	1	CBET 638	LOSS	CBET 642	Ia
SN 2006le	75.17457	62.25525	UGC 3218	SAb	0.017432	0.000023	1	CBET 700	LOSS	CBET 702	Ia
SN 2006lf	69.62286	44.03379	UGC 3108	S?	0.013189	0.000017	2	CBET 704	LOSS	CBET 705	Ia
SN 2006mq	121.55157	−27.56262	ESO 494-G26	SAB(s)b pec	0.003229	0.000003	1	CBET 721	LOSS	CBET 724	Ia
SN 2007S	150.13010	4.40702	UGC 5378	Sb	0.01388	0.000033	1	CBET 825	POSS	CBET 829	Ia
SN 2007ca	202.77451	−15.10175	MCG −02-34-61	Sc pec sp	0.014066	0.00001	1	CBET 945	LOSS	CBET 947	Ia
SN 2007co	275.76493	29.89715	MCG +05-43-16	···	0.026962	0.00011	1	CBET 977	Nicolas	CBET 978	Ia
SN 2007cq	333.66839	5.08017	3	···	0.026218	0.000167	3	CBET 983	POSS	CBET 984	Ia
SN 2007fb	359.21827	5.50886	UGC 12859	Sbc	0.018026	0.000007	2	CBET 992	LOSS	CBET 993	Ia
SN 2007if	17.71421	15.46103	4	···	0.0745	0.00015	5	CBET 1059	ROTSE-III	CBET 1059	Iap
SN 2007le	354.70186	−6.52269	NGC 7721	SA(s)c	0.006728	0.000002	1	CBET 1100	Monard	CBET 1101	Ia
SN 2007nq	14.38999	−1.38874	UGC 595	E	0.045031	0.000053	1	CBET 1106	ROTSE-III	CBET 1106	Ia
SN 2007qe	358.55408	27.40916	5	···	0.024	0.001	6	CBET 1138	ROTSE-III	CBET 1138	Ia
SN 2007rx	355.04908	27.42097	6	···	0.0301	0.001	7	CBET 1157	ROTSE-III	CBET 1157	Ia
SN 2007 sr	180.46995	−18.97269	NGC 4038	SB(s)m pec	0.005417	0.000017	2	CBET 1172	CSS	CBET 1173	Ia
SN 2008C	104.29794	20.43723	UGC 3611	S0/a	0.016621	0.000013	1	CBET 1195	POSS	CBET 1197	Ia
SN 2008Z	145.81364	36.28439	7	···	0.02099	0.000226	1	CBET 1243	POSS	CBET 1246	Ia
SN 2008af	224.86846	16.65325	UGC 9640	E	0.033507	0.000153	1	CBET 1248	Boles	CBET 1253	Ia
SNF20080514–002	202.30350	11.27236	UGC 8472	S0	0.022095	0.00009	1	ATEL 1532	SNF	ATEL 1532	Ia
SNF20080522-000	204.19796	5.14200	SDSS?	···	0.04526	0.0002	9	SNF	SNF	B09	Ia
SNF20080522-011	229.99519	4.90454	SDSS?	···	0.03777	0.00006	9	SNF	SNF	B09	Ia
SN 2008fr	17.95488	14.64068	8	···	0.039	0.002	8	CBET 1513	ROTSE-III	CBET 1513	Ia
SN 2008fv	154.23873	73.40986	NGC 3147	SA(rs)bc	0.009346	0.000003	1	CBET 1520	Itagaki	CBET 1522	Ia
SN 2008fx	32.89166	23.87998	9	···	0.059	0.003	3	CBET 1523	CSS	CBET 1525	Ia
SN 2008gb	44.48821	46.86566	UGC 2427	Sbc	0.037626	0.000041	3	CBET 1527	POSS	CBET 1530	Ia
SN 2008gl	20.22829	4.80531	UGC 881	E	0.034017	0.000117	1	CBET 1545	CHASE	CBET 1547	Ia

Table 1
(Continued)

SN Name	R.A.[a] $\alpha(2000)$	Decl.[a] $\delta(2000)$	Host[b] Galaxy	Morphology[c]	z_{helio}[d]	$\sigma_{z_{helio}}$[d]	z[d] Ref.	Discovery[b] Reference	Discoverer(s)[e]	Type[f] Reference	Type[g]
SN 2008hm	51.79540	46.94421	2MFGC 02845	Spiral	0.019664	0.000077	1	CBET 1586	LOSS	CBET 1594	Ia
SN 2008hs	36.37335	41.84311	NGC 910	E+	0.017349	0.000073	2	CBET 1598	LOSS	CBET 1599	Ia
SN 2008hv	136.89178	3.39240	NGC 2765	S0	0.012549	0.000067	1	CBET 1601	CHASE	CBET 1603	Ia
SN 2008hy	56.28442	76.66533	IC 334	S?	0.008459	0.000023	1	CBET 1608	POSS	CBET 1610	Ia
SN 2009D	58.59495	−19.18194	MCG −03-10-52	Sb	0.025007	0.000033	1	CBET 1647	LOSS	CBET 1647	Ia
SN 2009Y	220.59865	−17.24675	NGC 5728	(R 1)SAB(r)a	0.009316	0.000026	2	CBET 1684	PASS, LOSS	CBET 1688	Ia
SN 2009ad	75.88914	6.66000	UGC 3236	Sbc	0.0284	0.000005	1	CBET 1694	POSS	CBET 1695	Ia
SN 2009al	162.84201	8.57833	NGC 3425	S0	0.022105	0.00008	1	CBET 1705	CSS	CBET 1708	Ia
SN 2009an	185.69715	65.85145	NGC 4332	SB(s)a	0.009228	0.000004	2	CBET 1707	Cortini+, Paivinen	CBET 1709	Ia
SN 2009bv	196.83538	35.78433	MCG +06-29-39	⋯	0.036675	0.000063	1	CBET 1741	PIKA	CBET 1742	Ia
SN 2009dc	237.80042	25.70790	UGC 10064	S0	0.021391	0.00007	1	CBET 1762	POSS	CBET 1768	Iap
SN 2009do	188.74310	50.85108	NGC 4537	S	0.039734	0.00008	1	CBET 1778	LOSS, POSS	CBET 1778	Ia
SN 2009ds	177.26706	−9.72892	NGC 3905	SB(rs)c	0.019227	0.000021	2	CBET 1784	Itagaki	CBET 1788	Ia
SN 2009fw	308.07711	−19.73336	ESO 597-6	SA(rs)0-?	0.028226	0.00011	1	CBET 1836	CHASE	CBET 1849	Ia
SN 2009fv	247.43430	40.81153	NGC 6173	E	0.0293	0.00005	1	CBET 1834	POSS	CBET 1846	Ia
SN 2009ig	39.54843	−1.31257	NGC 1015	SB(r)a	0.00877	0.000021	1	CBET 1918	LOSS	CBET 1918	Ia
SN 2009im	53.34204	−4.99903	NGC 1355	S0 sp	0.0131	0.0001	1	CBET 1925	Itagaki	CBET 1934	Ia
SN 2009jr	306.60846	2.90889	IC 1320	SB(s)b?	0.016548	0.00006	1	CBET 1964	Arbour	CBET 1968	Ia
SN 2009kk	57.43441	−3.26447	2MFGC 03182	⋯	0.012859	0.00015	1	CBET 1991	CSS	CBET 1991	Ia
SN 2009kq	129.06316	28.06711	MCG +05-21-1	Spiral	0.011698	0.00002	1	CBET 2005	POSS	ATEL 2291	Ia
SN 2009le	32.32152	−23.41242	ESO 478-6	Sbc	0.017792	0.000009	2	CBET 2022	CHASE	CBET 2025	Ia
SN 2009lf	30.41513	15.33290	10	⋯	0.045	0.002	3	CBET 2023	CSS	CBET 2025	Ia
SN 2009na	161.75577	26.54364	UGC 5884	SA(s)b	0.020979	0.000006	2	CBET 2098	POSS	CBET 2103	Ia
SN 2010Y	162.76658	65.77966	NGC 3392	E?	0.01086	0.000103	1	CBET 2168	Cortini	CBET 2168	Ia
PS1-10w	160.67450	58.84392	Anonymous	⋯	0.031255	0.0001	4	R14	PanSTARRS1	R14	Ia
PTF10bjs	195.29655	53.81604	MCG +09-21-83	⋯	0.030027	0.000073	1	ATEL 2453	PTF	ATEL 2453	Ia
SN 2010ag	255.97330	31.50152	UGC 10679	Sb(f)	0.033791	0.000175	2	CBET 2195	POSS	CBET 2196	Ia
SN 2010ai	194.84999	27.99646	11	E	0.018369	0.000123	1	CBET 2200	ROTSE-III, Itagaki	CBET 2200	Ia
SN 2010cr	202.35442	11.79637	NGC 5177	S0	0.02157	0.000097	1	CBET 2281	Itagaki, PTF	ATEL 2580	Ia
SN 2010dl	323.75440	−0.51345	IC 1391	⋯	0.030034	0.00015	1	CBET 2296	CSS	CBET 2298	Ia
PTF10icb	193.70484	58.88198	MCG +10-19-1	⋯	0.008544	0.000008	2	ATEL 2657	PTF	ATEL 2657	Ia
SN 2010dw	230.66775	−5.92125	12	⋯	0.03812	0.00015	1	CBET 2310	PIKA	CBET 2311	Ia
SN 2010ew	279.29933	30.63026	CGCG 173-018	S	0.025501	0.000127	1	CBET 2345	POSS	CBET 2356	Ia
SN 2010ex	345.04505	26.09894	CGCG 475-019	Compact	0.022812	0.000005	1	CBET 2348	Ciabattari+	CBET 2353	Ia
SN 2010gn	259.45832	40.88128	13	Disk Gal	0.0365	0.0058	1	ATEL 2718	PTF	CBET 2386	Ia
SN 2010iw	131.31205	27.82325	UGC 4570	SABdm	0.021498	0.000017	1	CBET 2505	CSS	CBET 2511	Ia?
SN 2010ju	85.48321	18.49746	UGC 3341	SBab	0.015244	0.000013	1	CBET 2549	LOSS	CBET 2550	Ia
SN 2010jv	111.86051	33.81143	NGC 2379	SA0	0.013469	0.000083	1	CBET 2549	LOSS	CBET 2550	Ia
SN 2010 kg	70.03505	7.34995	NGC 1633	SAB(s)ab	0.016632	0.000007	2	CBET 2561	LOSS	CBET 2561	Ia
SN 2011B	133.95016	78.21693	NGC 2655	SAB(s)0/a	0.00467	0.000003	1	CBET 2625	Itagaki	CBET 262	Ia
SN 2011K	71.37662	−7.34808	14	⋯	0.0145	0.001	3	CBET 2636	CSS	CBET 2636	Ia
SN 2011aa	114.17727	74.44319	UGC 3906	S	0.012512	0.000033	2	CBET 2653	POSS	CBET 2653	Iap?
SN 2011ae	178.70514	−16.86280	MCG −03-30-19	⋯	0.006046	0.000019	1	CBET 2658	CSS	CBET 2658	Ia
SN 2011ao	178.46267	33.36277	IC 2973	SB(s)d	0.010694	0.000002	2	CBET 2669	POSS	CBET 2669	Ia
SN 2011at	142.23977	−14.80573	MCG −02-24-27	SB(s)d	0.006758	0.00002	1	CBET 2676	POSS	CBET 2676	Ia
SN 2011by	178.93951	55.32592	NGC 3972	SA(s)bc	0.002843	0.000005	1	CBET 2708	Jin+	CBET 2708	Ia

Table 1
(Continued)

SN Name	R.A.[a] $\alpha(2000)$	Decl.[a] $\delta(2000)$	Host[b] Galaxy	Morphology[c]	z_{helio}[d]	$\sigma_{z_{helio}}$[d]	z[d] Ref.	Discovery[b] Reference	Discoverer(s)[e]	Type[f] Reference	Type[g]
SN 2011de	235.97179	67.76196	UGC 10018	(R')SB(s)bc	0.029187	0.000017	2	CBET 2728	POSS	CBET 2728	Iap?
SN 2011df	291.89008	54.38632	NGC 6801	SAcd	0.014547	0.000019	2	CBET 2729	POSS	CBET 2729	Ia

Notes.

[a] SN R.A., decl. positions [in decimal degrees] are best-fit SN centroids appropriate for forced DoPHOT photometry at fixed coordinates.

[b] Host galaxy names, discovery references, and discovery group/individual credits from NASA/IPAC Extragalactic Database (NED; http://ned.ipac.caltech.edu/) and NASA/ADS (http://adswww.harvard.edu/abstract_service.html). Also see IAUC List of SNe: http://www.cbat.eps.harvard.edu/lists/Supernovae.html. For SN Ia with non-standard IAUC names, we found the associated host galaxy from IAUC/CBET/ATel notices or the literature and searched for the recession velocity with NED. When the SN Ia is associated with a faint host not named in any major catalogs (NGC, UGC, …) but named in a large galaxy survey (e.g., SDSS, 2MASS), we include the host name from the large survey rather than "Anonymous." However, to accomodate the table width on a single page, long galaxy names are numbered. 1: APMUKS(BJ) B141934.25+021314.0 (SN 2005ch), 2: NSF J022743.32+281037.6 (SN 2005eu), 3: 2MASX J22144070+0504435 (SN 2007cq), 4: J011051.37+152739 (SN 2007if), 5: NSF J235412.09+272432.3 (SN 2007qe), 6: BATC J234012.05+272512.23 (SN 2007rx), 7: SDSS J094315.36+361709.2 (SN 2008Z), 8: SDSS J011149.19+143826.5 (SN 2008fr), 9: 2MASX J02113233+2353074 (SN 2008fx). The machine-readable version of this table has full galaxy names.

[c] Host galaxy morphologies taken from NED where available. Hosts with unknown morphologies denoted by …

[d] Heliocentric redshift z_{helio}, $\sigma_{z_{helio}}$ references are from 1: NED host galaxy name, 2: NED 21 cm or optical with smallest uncertainty, 3: CfA FAST spectrum on Tillinghast 1.5 m telescope, 4: Rest et al. (2014): PanSTARRS1, 5: Childress et al. (2011), 6: CBET 1176, 7: Hicken et al. (2009a), 8: CBET 1513, 9: Childress et al. (2013). For SN 2008fr, the NED redshift incorrectly lists the redshift of SN 2008fs (see CBET 1513). Heliocentric redshifts have not been corrected for any local flow models.

[e] Discovery References/URLs: LOSS: Lick Observatory Supernova Search (see Li et al. 2000; Filippenko 2005, and references therein); Tenagra II (http://www.tenagraobservatories.com/Discoveries.htm); ROTSE-III (Quimby 2006); POSS: Puckett Observatory Supernova Search (http://www.cometwatch.com/search.html); BRASS: (http://brass.astrodatabase.net); SDSS-II: Sloan Digital Sky Survey II (Frieman et al. 2008b); CSS: Catalina Sky Survey (http://www.lpl.arizona.edu/css/); SNF: Nearby Supernova Factory (http://snfactory.lbl.gov/); CHASE: CHilean Automatic Supernova sEarch (http://www.das.uchile.cl/proyectoCHASE/); CRTS: Catalina Real-Time Transient Survey (http://crts.caltech.edu/); Itagaki (http://www.k-itagaki.jp/); Boles: Coddenham Astronomical Observatory, U.K. (http://www.coddenhamobservatories.org/); CROSS (http://wwww.cortinasetelle.it/snindex.htm); LSSS: La Sagra Sky Survey (http://www.minorplanets.org/OLS/LSSS.html); PASS: Perth Automated Supernova Search (http://www.perthobservatory.wa.gov.au/research/spps.html); Williams 1997); PIKA: Comet and Asteroid Search Program (http://www.observatorij.org/Pika.html); PanSTARRS1: (http://pan-starrs.ifa.hawaii.edu/public/); THCA Supernova Survey (http://www.thca.tsinghua.edu.cn/en/index.php/TUNAS).

[f] Spectroscopic type reference. B09—Bailey et al. (2009); Spectroscopic type reference. R14—Rest et al. (2014).

[g] Spectroscopic type of SN Ia—spectroscopically normal SN Ia. Spectroscopically peculiar SN Ia: including 91bg-like and 06gz-like objects. Uncertain spectroscopic types are denoted with a question mark (?): SN 2011de: classified as normal Ia in CBET 2728. But NIR LC morphology is consistent with a slow declining object (e.g., SN 2009dc-like). We classify it as Ia-pec.; SN 2011aa: classified as SN 1998aq-like normal Ia in CBET 2653. But Brown et al. (2014) identified it as a Super Chandrasekhar mass candidate, and NIR LC morphology is consistent with a slow declining object (e.g., SN 2009dc-like). We classify it as Ia-pec. SN 2010iw: classified as SN 2000cx-like, peculiar Ia in CBET 2511. But the NIR LC has the double-peaked morphology of normal Ia. We classify it as a normal Ia.

(This table is available in machine-readable form.)

Table 2
General Properties of 4 PAIRITEL SN Iax

SN Name	R.A.[a] α(2000)	Decl.[a] δ(2000)	Host[b] Galaxy	Morphology[c]	$z_{\mathrm{helio}}^{\mathrm{d}}$	$\sigma_{z_{\mathrm{helio}}}$[d]	z[d] Ref.	Discovery[b] Reference	Discoverer(s)[e]	Type[f] Reference	Type[g]
SN 2005hk	6.96187	−1.19819	UGC 272	SAB(s)d	0.012993	0.000041	1	IAUC 8625	SDSS-II, LOSS	CBET 269; Ph07	Iax
SN 2008A	24.57248	35.37029	NGC 634	Sa	0.016455	0.000007	2	CBET 1193	Ichimura	CBET 1198; F13; Mc14b	Iax
SN 2008ae	149.01322	10.49965	IC 577	S?	0.03006	0.000037	2	CBET 1247	POSS	CBET 1250; F13	Iax
SN 2008 ha	353.71951	18.22659	UGC 12682	Im	0.004623	0.000002	2	CBET 1567	POSS	CBET 1576; F09	Iax

Notes.
[a–e] See Table 1 caption.
[f] Spectroscopic type reference, Ph07: Phillips et al. (2007), F09: Foley et al. (2009), F13: Foley et al. (2013), Mc14b: McCully et al. (2014b).
[g] Spectroscopic type Iax (Foley et al. 2013).

(This table is available in machine-readable form.)

Following Meikle (2000), pioneering work by Krisciunas et al. (2004a) (hereafter K04a) demonstrated that SN Ia have a narrow luminosity range in JHK_s at $t_{B\,\max}$ with smaller scatter than in B and V. Using 16 NIR SN Ia, K04a found no correlation between optical LC shape and intrinsic NIR luminosity. K04a measured JHK_s absolute magnitude distributions with 1σ uncertainties of only $\sigma_J = 0.14$, $\sigma_H = 0.18$, and $\sigma_{K_s} = 0.12$ mag. While K04a used a small, inhomogeneous, sample of 16 LCs, in WV08, we presented 1087 JHK_s photometric observations of 21 objects (including 20 SN Ia and 1 SN Iax), the largest homogeneously observed low-z sample at the time. NIR data from WV08 and the literature strengthened the evidence that normal SN Ia are excellent NIR standard candles, especially in the H band, where absolute magnitudes have an intrinsic rms of 0.15–0.16 mag, without applying any reddening or LC shape corrections, comparable to the scatter in optical data corrected for both.

WV08 suggested that LC shape variation, especially in the J band, might provide additional information for correcting NIR LCs and improving distance determinations. In M09, we applied a novel hierarchical Bayesian framework and a model accounting for variations in the J-band LC shape to NIR SN Ia data, constraining the marginal scatter of the NIR peak absolute magnitudes to 0.17, 0.11, and 0.19 mag in JHK_s, respectively (see Figure 9 of M09). Folatelli et al. (2010) obtained similar dispersions of 0.12–0.16 mag in $YJHK_s$, after correcting for NIR LC shape. Using 13 well-sampled, low-extinction, normal NIR SN Ia LCs from the Carnegie Supernova Project (CSP), K12 find scatters in absolute magnitude of 0.12, 0.12, and 0.09 mag in YJH, respectively. K12 also confirm that NIR LC shape correlates with intrinsic NIR luminosity, finding evidence for a nonzero correlation between the peak absolute JH maxima and the decline rate parameter Δm_{15}, with only marginal dependence in Y. For a set of 12 SN Ia with JH LCs, Barone-Nugent et al. (2012) find a very small JH-band scatter of only 0.116 and 0.085 mag, respectively, although their data set only includes 3–5 LC points for each of the 12 objects. Similarly, Weyant et al. (2014) use only 1–3 data points for each of 13 low-z NIR SN Ia to infer an H-band dispersion of 0.164 mag. Both Barone-Nugent et al. (2012) and Weyant et al. (2014) use auxiliary optical data to estimate $t_{B\,\max}$. All of these results suggest that NIR data will be crucial for maximizing the utility of SN Ia as cosmological distance indicators.

1.2. Organization of Paper

This paper is organized as follows. In Section 2, we discuss the current sample of nearby NIR SN Ia data including CfAIR2, describe the technical specifications of PAIRITEL, and outline our follow-up campaign. In Section 3 we describe the data reduction process, including mosaicked image creation, sky subtraction, host galaxy subtraction, and our photometry pipeline. In Section 4, we present tests of PAIRITEL photometry, emphasizing internal calibration with Two Micron All Sky Survey (2MASS) field star observations, tests for potential systematic errors, and external consistency checks for objects observed by both PAIRITEL and the CSP. Throughout Sections 2–4, we frequently reference F12, where many additional technical details can be found. In Section 5, we present the principal data products of this paper, which include JHK_s LCs of 94 SN Ia and 4 SN Iax. Further analysis of this data will be presented elsewhere. PAIRITEL and CSP comparison is discussed further in Section 6. Conclusions and directions for future work are summarized in Section 7. Additional details are included in a mathematical appendix (also see Section 7 of F12).

2. OBSERVATIONS

In Section 2.1, we provide recent historical context for CfAIR2 by describing the growing low-z sample of NIR SN Ia LCs. In Sections 2.2–2.4, we overview CfA NIR SN observations, describe PAIRITEL's observing capabilities, and detail our follow-up strategy to observe SN Ia in JHK_s.

2.1. Low-z NIR LCs of SN Ia

Technological advances in infrared detector technology have recently made it possible to obtain high-quality NIR photometry for large numbers of SN Ia. Phillips (2012) provides an excellent recent review of the cosmological and astrophysical results derived from NIR SN Ia observations made over the past three decades. Early NIR observations of SN Ia were made by Kirshner et al. (1973), Elias et al. (1981, 1985), and Frogel et al. (1987) and were particularly challenging as a result of the limited technology of the time. In addition, the flux contrast between the host galaxy and the SN Ia is typically smaller in the NIR than at optical wavelengths, making high-S/N observations possible only for the brightest NIR objects with the detectors available in the 1970s and 1980s. While this situation has improved somewhat in the subsequent decades, NIR photometry is still significantly more challenging than at optical wavelengths. Elias et al. (1985) was the first to present an NIR Hubble diagram for six SN Ia. Although these six SN Ia LCs were not classified spectroscopically, Elias et al. (1985) was also the first to use what became the modern spectroscopic nomenclature of Type Ia instead of Type I to distinguish between SN Ia and SN Ib; SN Ib are now thought to be core-collapse SN of stars that have lost their outer hydrogen envelopes (see Modjaz et al. 2014 and references therein).

In the late 1990s and early 2000s, panoramic NIR arrays made it possible to obtain NIR photometry comparable in quantity and quality to optical photometry for nearby SN Ia. The first early-time NIR photometry with modern NIR detectors observed before $t_{B\,\max}$ was presented for SN 1998bu (Jha et al. 1999; Hernandez et al. 2000). Since the first peak in the JHK_s band occurs ~3–5 days *before* $t_{B\,\max}$, depending on the filter, SN Ia must generally be discovered by optical searches at least ~5–8 days before $t_{B\,\max}$ in order to be observed before the NIR maximum (F12; see Section 2.4).

Pioneering early work was performed in the early 2000s in Chile at the Las Campanas Observatory (LCO) and the Cerro Tololo Inter-American Observatory, spearheaded by the work of Krisciunas et al. (2000, 2001, 2003, 2004b, 2004c). K04a presented the largest Hubble diagram of its kind to date with 16 SN Ia. Before WV08 published 21 PAIRITEL NIR LCs observed by the CfA at FLWO, a handful of other NIR observations, usually for individual or small numbers of SN Ia or SN Iax of particular interest, were presented (Cuadra et al. 2002; Di Paola et al. 2002; Candia et al. 2003; Valentini et al. 2003; Benetti et al. 2004; Garnavich et al. 2004; Sollerman et al. 2004; Krisciunas et al. 2005b; Elias-Rosa et al. 2006, 2008; Krisciunas et al. 2006, 2007; Phillips et al. 2006, 2007; Pastorello et al. 2007a, 2007b; Stanishev et al. 2007; Stritzinger & Sollerman 2007; Pignata et al. 2008; Taubenberger et al. 2008; Wang et al. 2008). The largest NIR

SN Ia sample prior to CfAIR2 was obtained by the CSP (Freedman 2005; Hamuy et al. 2006) at LCO, including observations of 59 normal and 14 peculiar NIR SN Ia LCs (Schweizer et al. 2008; Contreras et al. 2010; Stritzinger et al. 2010, 2011; Taubenberger et al. 2011).[18] Other SN Ia or SN Iax papers with published NIR data since WV08 include Krisciunas et al. (2009, 2011), Leloudas et al. (2009), Yamanaka et al. (2009), Barone-Nugent et al. (2012), Biscardi et al. (2012), Matheson et al. (2012), Taddia et al. (2012), Silverman et al. (2013), Amanullah (2014), Cartier et al. (2014), Foley et al. (2014b), Goobar et al. (2014), Stritzinger et al. (2014), Weyant et al. (2014), Marion et al. (2015), and Stritzinger et al. (2015). See Table 3 for a fairly comprehensive listing of SN Ia and SN Iax with NIR observations in the literature or presented in this paper.

Overall, while ∼1000 nearby SN Ia have been observed at optical wavelengths, prior to CfAIR2, only 147 total unique nearby objects have at least one NIR band of published $YJHK_s$ data obtained with modern NIR detectors (from SN 1998bu onward). These include 121 normal SN Ia, 22 peculiar SN Ia, and 4 SN Iax . CfAIR2 adds 66 new unique objects, including 62 normal SN Ia. By this measure, CfAIR2 increases the world published NIR sample of total unique objects by 66/147 ≈ 45% and normal SN Ia by 62/121 ≈ 51%. Twelve additional CfAIR2 objects have new data that supersede previously published PAIRITEL LCs and no data published by other groups. If we include these, CfAIR2 adds 78 total objects and 73 normal SN Ia to the literature. By this measure, CfAIR2 increases the world published sample of NIR objects by 78/135 ≈ 58% and the sample of normal SN Ia by 72/110 ≈ 65%. See Table 3.

2.2. PAIRITEL NIR Supernova Observations

Out of 121 total SN Ia and SN Iax observed from 2005 to 2011 by PAIRITEL, 23 are not included in CfAIR2. CfAIR2 includes improved photometry for 20 of 21 objects from WV08. For SN 2005cf, our photometry pipeline failed to produce a galaxy-subtracted LC, so we include the WV08 LC for SN 2005cf in CfAIR2 and all applicable figures or tables. These 20 objects include additional observations not published in WV08, processed homogeneously using upgraded mosaic and photometry pipelines (see Section 3). Table 1 lists general properties of the 94 CfAIR2 SN Ia, and Table 2 lists these for the 4 CfAIR2 SN Iax.

Heliocentric galaxy redshifts are provided in Tables 1 and 2 and CMB frame redshifts are given in Table 9 to ease construction of future Hubble diagrams including NIR SN Ia data.[19] We obtained recession velocities from identified host galaxies as listed in the NASA/IPAC Extragalactic Database (NED). In cases where NED did not return a host galaxy or the host galaxy had no reported NED redshift, we either obtained redshift estimates from our own CfA optical spectra (Matheson et al. 2008; Blondin et al. 2012) or found redshifts reported in the literature. Figure 1 shows a histogram of CfAIR2 heliocentric galaxy redshifts $z_{\rm helio}$ for 86 normal SN Ia with $t_{B\,\rm max}$ estimates accurate to within less than 10 days.

[18] The CSP work did not yet distinguish SN Iax as a separate subclass from SN Ia.

[19] However, note that none of the redshifts in Tables 1 and 2 or 9 have been corrected for local flow models. Objects with recession velocities $\lesssim$3000 km s^{-1} ($z \lesssim 0.01$) must have their redshifts corrected with local flow models or other distance information before being included in Hubble diagrams.

From 2005 to 2011, we also obtained extensive PAIRITEL NIR observations of 25 SN Ib/c (Bianco et al. 2014) and 20 SN II (to be presented elsewhere). Table 4 references all previously published and in preparation papers using PAIRITEL SN data, including multiwavelength studies of individual objects (Tominaga et al. 2005; Kocevski et al. 2007; Foley et al. 2009; Modjaz et al. 2009; Wang et al. 2009; Drout et al. 2013; Sanders et al. 2013; Fransson et al. 2014; Marion et al. 2014; Margutti et al. 2014) and NIR/optical LC compilations for SN of all types (e.g., Modjaz 2007; WV08; F12; Bianco et al. 2014). The most recent of these papers (Sanders et al. 2013; Bianco et al. 2014; Fransson et al. 2014; Marion et al. 2014; Margutti et al. 2014) used the same mosaic and photometry pipelines also used to produce the CfAIR2 data for this paper (see Section 3). For completeness, we also include information on all other types of SN with published PAIRITEL observations for both current and older pipelines.

2.3. PAIRITEL 1.3 m Specifications

Dedicated in October 2004, PAIRITEL uses the 2MASS (Skrutskie et al. 2006) northern telescope together with the 2MASS southern camera. PAIRITEL is a fully automated robotic telescope with the sequence of observations controlled by an optimized queue-scheduling database (Bloom et al. 2006). Two dichroic mirrors allow simultaneous observing in JHK_s (1.2, 1.6, and 2.2 μm, respectively; Cohen et al. 2003; Skrutskie et al. 2006) with three 256 × 256 pixel HgCdTe NICMOS3 arrays. Figure 1 of WV08 shows a composite JHK_s mosaicked image of SN 2006D (see Section 3.1).

Since the observations are conducted with the instrument that defined the 2MASS JHK_s system, we use the 2MASS point source catalog (Cutri et al. 2003) to establish photometric zero points. Typical 30-minute (1800 s) observations (including slew overhead) reach 10σ sensitivity limits of ∼18, 17.5, and 17 mag for point sources in JHK_s, respectively (F12). For fainter objects, 10σ point source sensitivities of 19.4, 18.5, and 18 mag are achievable with 1.5 hr (5400 s) of dithered imaging in JHK_s, respectively (F12). PAIRITEL thus observes significantly deeper than 2MASS, which used a 7.8 s total exposure time to achieve 10σ point source sensitivities of 15.8, 15.1, and 14.3 mag in JHK_s, respectively (Skrutskie et al. 2006; see Section 4).

2.4. Observing Strategy

Automation of PAIRITEL made it possible to study SN with unprecedented temporal coverage in the NIR, by responding quickly to new SN and revisiting targets frequently (Bloom et al. 2006; WV08; F12). CfAIR2 followed up SN discovered by optical searches at $\delta \gtrsim -30°$ with $V \lesssim 18$ mag, with significant discovery contributions from both amateur and professional astronomers (see Tables 1 and 2). SN candidates with a favorable observation window and airmass <2.5 from Mount Hopkins were considered for the PAIRITEL observation queue. We observed SN of all types but placed highest priority on the brightest SN Ia discovered early or close to maximum brightness. SN candidates meeting these criteria were often added to the queue before spectroscopic typing to observe the early-time LC. Since many optically discovered SN of all types brighter than $V < 18$ mag are spectroscopically typed by our group at the CfA[20] or other groups within

[20] http://www.cfa.harvard.edu/supernova/OldRecentSN.html

Table 3
SN Ia and SN Iax with Published NIR Photometry

SN Name	Type[a]	NIR Photometry References[b]	SN Name	Type[a]	NIR Photometry References[b]	SN Name	Type[a]	NIR Photometry References[b]
SN 2012Z	Iax	S15	SN 2007nq	Ia	CfAIR2; S11	SN 2007as	Ia	S11
SN 2014J	Ia	A14; Go14; F14b	SN 2007le	Ia	CfAIR2; S11	SN 2007ax	Ia-pec	S11
SN 2013bh	Ia-pec	Si13	SN 2007if	Ia-pec	CfAIR2; S11	SN 2007ba	Ia-pec	S11
SN 2011fe	Ia	M12	SN 2007fb	Ia	CfAIR2	SN 2007bc	Ia	S11
SN 2010ae	Iax	S14	SN 2007cq	Ia	CfAIR2; WV08	SN 2007bd	Ia	S11
SN 2008J	Ia	Ta12	SN 2007co	Ia	CfAIR2	SN 2007bm	Ia	S11
SN 2011df	Ia	CfAIR2	SN 2007ca	Ia	CfAIR2; S11	SN 2007hx	Ia	S11
SN 2011de	Ia-pec?	CfAIR2	SN 2007S	Ia	CfAIR2; S11	SN 2007jg	Ia	S11
SN 2011by	Ia	CfAIR2	SN 2006mq	Ia	CfAIR2	SN 2007on	Ia	S11
SN 2011at	Ia	CfAIR2	SN 2006lf	Ia	CfAIR2; WV08	SN 2008R	Ia	S11
SN 2011ao	Ia	CfAIR2	SN 2006le	Ia	CfAIR2; WV08	SN 2008bc	Ia	S11
SN 2011ae	Ia	CfAIR2	SN 2006gr	Ia	CfAIR2; WV08	SN 2008bq	Ia	S11
SN 2011aa	Ia-pec?	CfAIR2	SN 2006cz	Ia	CfAIR2	SN 2008fp	Ia	S11
SN 2011K	Ia	CfAIR2	SN 2006cp	Ia	CfAIR2; WV08	SN 2008gp	Ia	S11
SN 2011B	Ia	CfAIR2	SN 2006ax	Ia	CfAIR2; WV08; C10	SN 2008ia	Ia	S11
SN 2010kg	Ia	CfAIR2	SN 2006ac	Ia	CfAIR2; WV08	SN 2009F	Ia-pec	S11
SN 2010jv	Ia	CfAIR2	SN 2006X	Ia	CfAIR2; WV08; C10; WX08	SN 2004eo	Ia	C10; Pa07b
SN 2010ju	Ia	CfAIR2	SN 2006N	Ia	CfAIR2; WV08	SN 2004S	Ia	K07
SN 2010iw	Ia?	CfAIR2	SN 2006E	Ia	CfAIR2	SN 2003hv	Ia	L09
SN 2010gn	Ia	CfAIR2	SN 2006D	Ia	CfAIR2; WV08; C10	SN 2003gs	Ia-pec	K09
SN 2010ex	Ia	CfAIR2	SN 2005na	Ia	CfAIR2; WV08; C10	SN 2003du	Ia	St07
SN 2010ew	Ia	CfAIR2	SN 2005ls	Ia	CfAIR2	SN 2003cg	Ia	ER06
SN 2010dw	Ia	CfAIR2	SN 2005ke	Ia-pec	CfAIR2; WV08; C10	SN 2002fk	Ia	Ca14
PTF10icb	Ia	CfAIR2	SN 2005iq	Ia	CfAIR2; WV08; C10	SN 2002dj	Ia	P08
SN 2010dl	Ia	CfAIR2	SN 2005hk	Iax	CfAIR2; WV08; Ph07	SN 2002cv	Ia	ER08; DP02
SN 2010cr	Ia	CfAIR2	SN 2005eu	Ia	CfAIR2; WV08	SN 2002bo	Ia	K04c ; B04
SN 2010ai	Ia	CfAIR2	SN 2005eq	Ia	CfAIR2; WV08; C10	SN 2001el	Ia	K03; S07
SN 2010ag	Ia	CfAIR2	SN 2005el	Ia	CfAIR2; WV08; C10	SN 2001cz	Ia	K04c
PTF10bjs	Ia	CfAIR2	SN 2005ch	Ia	CfAIR2; WV08	SN 2001cn	Ia	K04c
PS1-10w	Ia	CfAIR2	SN 2005cf	Ia	CfAIR2; WV08; Pa07a	SN 2001bt	Ia	K04c
SN 2010Y	Ia	CfAIR2	SN 2005bo	Ia	CfAIR2	SN 2001ba	Ia	K04b
SN 2009na	Ia	CfAIR2	SN 2005bl	Ia-pec	CfAIR2; WV08	SN 2001ay	Ia-pec	K11
SN 2009lf	Ia	CfAIR2	SN 2005ao	Ia	CfAIR2; WV08	SN 2000cx	Ia-pec	Ca03; So04; Cu02
SN 2009le	Ia	CfAIR2	SN 2004ef	Ia	C10	SN 2000ce	Ia	K01
SN 2009kq	Ia	CfAIR2	SN 2004ey	Ia	C10	SN 2000ca	Ia	K04b
SN 2009kk	Ia	CfAIR2	SN 2004gs	Ia	C10	SN 2000bk	Ia	K01
SN 2009jr	Ia	CfAIR2	SN 2004gu	Ia-pec	C10	SN 2000bh	Ia	K04b
SN 2009im	Ia	CfAIR2	SN 2005A	Ia	C10	SN 2000E	Ia	V03
SN 2009ig	Ia	CfAIR2	SN 2005M	Ia	C10	SN 1999gp	Ia	K01
SN 2009fv	Ia	CfAIR2	SN 2005ag	Ia	C10	SN 1999ek	Ia	K04c
SN 2009fw	Ia	CfAIR2	SN 2005al	Ia	C10	SN 1999ee	Ia	K04b
SN 2009ds	Ia	CfAIR2	SN 2005am	Ia	C10	SN 1999cp	Ia	K00
SN 2009do	Ia	CfAIR2	SN 2005hc	Ia	C10	SN 1999cl	Ia	K00
SN 2009dc	Ia-pec	CfAIR2; T11; Y09	SN 2005kc	Ia	C10	SN 1999by	Ia-pec	G04
SN 2009bv	Ia	CfAIR2	SN 2005ki	Ia	C10	SN 1999ac	Ia-pec	Ph06
SN 2009an	Ia	CfAIR2	SN 2006bh	Ia	C10	SN 1999aa	Ia-pec	K00
SN 2009al	Ia	CfAIR2	SN 2006eq	Ia	C10	SN 1998bu	Ia	H00; J99
SN 2009ad	Ia	CfAIR2	SN 2006gt	Ia-pec	C10	PTF09dlc	Ia	BN12
SN 2009Y	Ia	CfAIR2	SN 2006mr	Ia-pec	C10	PTF10hdv	Ia	BN12
SN 2009D	Ia	CfAIR2	SN 2006dd	Ia	S10	PTF10mwb	Ia	BN12
SN 2008hy	Ia	CfAIR2	SN 2005hj	Ia	S11	PTF10ndc	Ia	BN12
SN 2008hv	Ia	CfAIR2; S11	SN 2005ku	Ia	S11	PTF10nlg	Ia	BN12
SN 2008hs	Ia	CfAIR2	SN 2006bd	Ia-pec	S11	PTF10qyx	Ia	BN12
SN 2008hm	Ia	CfAIR2	SN 2006br	Ia	S11	PTF10tce	Ia	BN12
SN 2008ha	Iax	CfAIR2; F09	SN 2006bt	Ia-pec	S11	PTF10ufj	Ia	BN12
SN 2008gl	Ia	CfAIR2	SN 2006ej	Ia	S11	PTF10wnm	Ia	BN12
SN 2008gb	Ia	CfAIR2	SN 2006et	Ia	S11	PTF10wof	Ia	BN12
SN 2008fx	Ia	CfAIR2	SN 2006ev	Ia	S11	PTF10xyt	Ia	BN12
SN 2008fv	Ia	CfAIR2; Bi12	SN 2006gj	Ia	S11	SN 2011hr	Ia	W14
SN 2008fr	Ia	CfAIR2	SN 2006hb	Ia	S11	SN 2011gy	Ia	W14
SNF20080522-011	Ia	CfAIR2	SN 2006hx	Ia	S11	SN 2011hk	Ia-pec	W14
SNF20080522-000	Ia	CfAIR2	SN 2006is	Ia	S11	SN 2011fs	Ia	W14
SNF20080514-002	Ia	CfAIR2	SN 2006kf	Ia	S11	SN 2011gf	Ia	W14

Table 3
(Continued)

SN Name	Type[a]	NIR Photometry References[b]	SN Name	Type[a]	NIR Photometry References[b]	SN Name	Type[a]	NIR Photometry References[b]
SN 2008af	Ia	CfAIR2	SN 2006lu	Ia	S11	SN 2011hb	Ia	W14
SN 2008ae	Iax	CfAIR2	SN 2006ob	Ia	S11	SN 2011io	Ia	W14
SN 2008Z	Ia	CfAIR2	SN 2006os	Ia	S11	SN 2011iu	Ia	W14
SN 2008C	Ia	CfAIR2; S11	SN 2006ot	Ia-pec	S11	PTF11qri	Ia	W14
SN 2008A	Iax	CfAIR2	SN 2007A	Ia	S11	PTF11qmo	Ia	W14
SN 2007sr	Ia	CfAIR2; S08	SN 2007N	Ia-pec	S11	PTF11qzq	Ia	W14
SN 2007rx	Ia	CfAIR2	SN 2007af	Ia	S11	PTF11qpc	Ia	W14
SN 2007qe	Ia	CfAIR2	SN 2007ai	Ia	S11	SN 2011ha	Ia	W14

Notes.
[a] SN Spectroscopic Types: Ia—Normal SN Ia including 91T-like, 86G-like, and spectroscopically normal objects; Iap—Peculiar SN Ia including 91bg-like objects and extra-luminous, slow declining 06gz-like objects (Hicken et al. 2007); Iax—SN Iax including 02cx-like objects distinct from peculiar SN Ia (Li et al. 2003; Foley et al. 2013). Spectroscopic type references for CfAIR2 objects are in Tables 1 and 2, and in the references below for non-CfAIR2 objects with NIR photometry. SN with uncertain spectral types (SN 2011de, SN 2011aa, SN 2010iw) are denoted by a question mark (?) (see Table 1 caption).
[b] References for objects with at least one band of $YJHK_s$ photometry. CfAIR2: this paper; WV08: Wood-Vasey et al. (2008), W14: Weyant et al. (2014), S15: Stritzinger et al. (2015), S14: Stritzinger et al. (2014), F14b: Foley et al. (2014b), Go14: Goobar et al. (2014), Ca14: Cartier et al. (2014), A14: Amanullah (2014), Si13: Silverman et al. (2013), Ta12: Taddia et al. (2012), M12: Matheson et al. (2012), Bi12: Biscardi et al. (2012), BN12: Barone-Nugent et al. (2012), T11: Taubenberger et al. (2011), S11: Stritzinger et al. (2011), K11: Krisciunas et al. (2011), S10: Stritzinger et al. (2010), C10: Contreras et al. (2010), Y09: Yamanaka et al. (2009), L09: Leloudas et al. (2009), K09: Krisciunas et al. (2009), F09: Foley et al. (2009), WX08: Wang et al. (2008), T08: Taubenberger et al. (2008), S08: Schweizer et al. (2008), P08: Pignata et al. (2008), ER08: Elias-Rosa et al. (2008), S07: Stritzinger & Sollerman (2007), St07: Stanishev et al. (2007), Ph07: Phillips et al. (2007), Pa07b: Pastorello et al. (2007b), Pa07a: Pastorello et al. (2007a), K07: Krisciunas et al. (2007), Ph06: Phillips et al. (2006), ER06: Elias-Rosa et al. (2006), K05: Krisciunas et al. (2005b), So04: Sollerman et al. (2004), K04c: Krisciunas et al. (2004a), K04b: Krisciunas et al. (2004b), G04: Garnavich et al. (2004), B04: Benetti et al. (2004), V03: Valentini et al. (2003), K03: Krisciunas et al. (2003), Ca03: Candia et al. (2003), DP02: Di Paola et al. (2002), Cu02: Cuadra et al. (2002), K01: Krisciunas et al. (2001), K00: Krisciunas et al. (2000), H00: Hernandez et al. (2000), J99: Jha et al. (1999).

(This table is available in machine-readable form.)

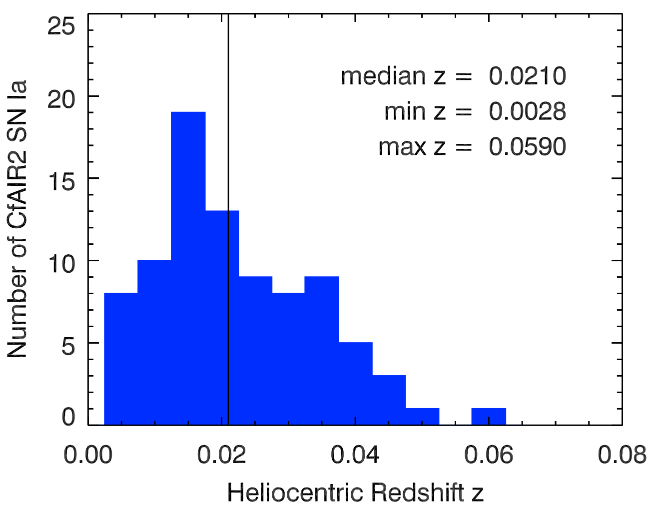

Figure 1. Histogram of heliocentric redshifts $z_{\rm helio}$ for 86 spectroscopically normal CfAIR2 SN Ia from Table 1 with $t_{B\,\rm max}$ estimates accurate to within less than 10 days. Bin size $\Delta z = 0.005$. Redshift statistics for the sample include median (black vertical line, 0.0210), minimum (0.0028), and maximum (0.0590). Heliocentric redshifts have not been corrected for any local flow models.

1–3 days of discovery, we rarely spent more than a few observations on objects we later deactivated after typing. All CfA SNe are spectroscopically classified using the SuperNova IDentification code (SNID; Blondin & Tonry 2007).

From 2005 to 2011, ~20–30 SN per year were discovered that were bright enough to observe with the PAIRITEL 1.3 m, with ~3–6 available on any given night from Mount Hopkins. Since we only perform follow-up NIR observations and are not conducting an NIR search to discover SN with PAIRITEL, we suffer from all the heterogeneous sample selection effects and biases incurred by each of the independent discovery efforts. A full analysis of the completeness of our sample is beyond the scope of this work. Overall, with ~30% of the time on a robotic telescope available for SN observations, effectively amounting to over 6 months on the sky, we observed over 2/3 of the candidate SN that met our follow-up criteria. We also observed galaxy template images (SNTEMP) for each SN to enable host subtraction (see Section 3.4).

3. DATA REDUCTION

Since WV08, we have substantially upgraded our data reduction software, including both pipelines for combining the raw data into mosaics and for performing photometry on the mosaicked images. All CfAIR2 data were processed homogeneously with a single mosaicking pipeline (hereafter `p3.6`) that adds and registers PAIRITEL raw images into mosaics (Section 3.1). The mosaics, as well as their associated noise and exposure maps, were then fed to a single photometry pipeline (hereafter `photpipe`), originally developed to handle optical data for the ESSENCE and SuperMACHO projects (Rest et al. 2005; Garg et al. 2007; Miknaitis et al. 2007) and modified to perform host galaxy subtraction and photometry on the NIR mosaicked images (Sections 3.4–3.8). Earlier mosaic and `photpipe` versions have been used for previously published PAIRITEL SN LCs (see Table 4), with recent modifications by A. Friedman and W. M. Wood-Vasey to produce compilations of SN Ia and SN Iax (CfAIR2; this work) and SN Ib and SN Ic (Bianco et al. 2014). `Photpipe` now takes as input improved noise mosaics to estimate the noise in the mosaicked images (Section 3.2), registers the images to a common reference frame with `SWarp` (Bertin et al. 2002), subtracts host galaxy light at the SN position using reference images with `HOTPANTS` (Becker et al. 2004, 2007),

Table 4
SN with Published or Forthcoming PAIRITEL Data

Object or *Compilation*	Type(s)	Reference	Comments
SN 2005bf	Ic-Ib	Tominaga et al. (2005)	Unusual core-collapse object
SN 2006aj	Ic-BL	Modjaz et al. (2006), Kocevski et al. (2007)	Associated with GRB 060281
SN 2006jc	Ib/c	Modjaz (2007)	Unusual core-collapse object; in M. Modjaz PhD thesis
SN 2008D	Ib	Modjaz et al. (2009)	Associated with *Swift* X-ray transient XRT 080109
SN 2005cf	Ia	Wang et al. (2009)	Normal SN Ia, significant multiwavelength data
SN 2008ha	Iax	Foley et al. (2009)	Extremely low luminosity SN Iax[a]
WV08	Ia, Ia-pec, Iax	Wood-Vasey et al. (2008)	Compilation of 20 SN Ia and 1 SN Iax NIR LCs[a]
F12	Ia, Ia-pec, Iax	Friedman (2012)	Compilation of SN Ia and SN Iax in A. Friedman PhD thesis[a]
M07	Ib,Ic	Modjaz (2007)	Compilation of SN Ib and SN Ic in M. Modjaz PhD thesis[b]
PS1-12sk	Ibn	Sanders et al. (2013)	Pan-STARRS1 project observations
SN 2005ek	Ic	Drout et al. (2013)	Photometry from Modjaz (2007)[b]
SN 2011dh	IIb	Marion et al. (2014)	SN in M51
SN 2009ip	LBV	Margutti et al. (2014)	Luminous blue variable with outbursts. Not a SN
SN 2010jl	IIn	Fransson et al. (2014)	Unusual core-collapse object
B14	Ib, Ic	Bianco et al. (2014)	Compilation of PAIRITEL SN Ib and SN Ic[b]
CfAIR2	Ia, Ia-pec, Iax	Friedman et al. (2015a)	This paper; compilation of PAIRITEL SN Ia, SN Ia-pec, SN Iax[a]
SN 2012cg	Ia	G. H. Marion et al. (2015b, in preparation)	Bright Ia with multiwavelength data

Notes.
[a] Photometry in this paper supersedes PAIRITEL LCs from Wood-Vasey et al. (2008) (except SN 2005cf), SN 2008ha LC in Foley et al. (2009), and F12.
[b] B14 supersedes M. Modjaz PhD thesis.

and performs point-spread function (PSF) photometry using DoPHOT (Schechter et al. 1993). Photometry is extracted from either the unsubtracted or the subtracted images by forcing DoPHOT to measure the PSF-weighted flux of the object at a fixed position in pixel coordinates (see Section 3.4; F12).

In Section 3.1, we describe our p3.6 mosaic pipeline. In Section 3.2, we describe sky subtraction and our improved method to produce noise mosaics corresponding to the mosaicked images. In Section 3.3, we discuss the undersampling of the PAIRITEL NIR camera. In Sections 3.4–3.7 we detail the host galaxy subtraction process and describe our method for performing photometry on the subtracted or unsubtracted images. Major photpipe improvements are summarized in Section 3.8. See F12 for additional details.

3.1. Mosaics

All CfAIR2 images were processed into mosaics at the CfA using p3.6 implemented in Python version 2.6.[21] F12 and references in Table 4 describe older mosaic pipelines. Klein & Bloom (2014) provide a more detailed description of p3.6 as used for PAIRITEL observations of RR Lyrae stars. Figures 3–5 show sample p3.6 *J*-band mosaics for all 98 CfAIR2 objects.

Including slew overhead for the entire dither pattern, typical exposure times range from 600 to 3600 s, yielding ~50–150 raw images for mosaicking. Excluding slew overhead, effective exposure times are generally ~40%–70% of the time on the sky, yielding typical actual exposure times of ~250 to ~2500 s. Raw images are obtained with standard double-correlated reads with the long-exposure (7.8 s) minus short-exposure (51 ms) frames in each filter treated as the "raw" frame input to p3.6. These raw 256 × 256 pixel images are of ~7.8 s duration with a plate scale of 2″ pixel^{-1} and an 8′.53 × 8′.53 field of view (FOV). To aid with reductions, the telescope is dithered after each set of three exposures with a step size <2′ based on a randomized dither pattern covering a typical ~12′ × 12′ FOV. The three raw images observed at each dither position are then added into "triplestacks" before mosaicking. The p3.6 pipeline processes all raw images by flat correction, dark current and sky subtraction, registration, and stacking to create final JHK_s mosaics using SWarp (Bertin et al. 2002). Bad pixel masks are created dynamically, and flat fields—which are relatively stable —were created from archival images. Since the short-timescale seeing also remains roughly constant in the several seconds of slew time between dithered images, we did not find it necessary to convolve the raw images to the seeing of a raw reference image before mosaicking. The seeing over long time periods (several months) remains relatively constant at 0″.77–0″.85.[22] The raw images are resampled from a raw image scale of 2″ pixel^{-1} into final mosaics with 1″ pixel^{-1} sampling with SWarp (Bertin et al. 2002). The typical FWHM in the final PAIRITEL mosaics is ~2″.5–3″.0, consistent with the average image quality obtained by 2MASS (Skrutskie et al. 2006).

The desired telescope pointing center for all dithered images is set to the SN R.A. and decl. coordinates from the optical discovery images. Unfortunately, as a result of various software and/or mechanical issues—for example, problems with the R. A. drive—the PAIRITEL 1.3 m telescope pointing accuracy can vary by ~1′–30′ from night to night. Catastrophic pointing errors can result in the SN being absent in all of the raw images and missing in the ~12′ × 12′ mosaic FOV. More often, nonfatal pointing errors result in the SN being absent or off-center in some, but not all, raw images. In p2.0 used for WV08, the mosaic center was constrained to be the SN coordinates and the mosaic size in pixels was fixed. This resulted in a significant fraction of failed or low-S/N mosaics using an insufficient number of raw images. For p3.0–p3.6, the constraint fixing the SN at the mosaic center was relaxed

[21] p1.0-p3.6 was developed at UC Berkeley and the CfA by J. S. Bloom, C. Blake, C. Klein, D. Starr, and A. Friedman.

[22] For typical seeing at FLWO since 2003, see https://www.mmto.org/node/249.

and the mosaic center was allowed to be the center of all imaging. This resulted in ∼15% more mosaic solutions than `p2.0`. Mosaics that failed processing at intermediate `photpipe` stages were excluded from the LC automatically. Some mosaics that succeeded to the end of `photpipe` were excluded based on visual inspection or by identifying outlier LC points during post-processing.

3.2. Sky Subtraction and Noise Maps

The PAIRITEL camera has no cold shutter, so dark current cannot be measured independently, and background frames include both sky and dark photons ("skark"). Fortunately, the thermal dark current counts across the raw frames are *negligible* in JHK_s for the NICMOS3 arrays on timescales comparable to the individual, raw, 7.8 s exposures (Skrutskie et al. 2006). Furthermore, the dark current rate does not detectably vary across the 1.5 hr of the maximum dither pattern used in these observations. Background frames also include an electronic bias, characterized by shading in each of the four raw image quadrants, which produces no noise, and amplifier glow, which peaks at the corners of the quadrants, and which, like thermal dark current, does produce Poisson noise. These intrinsic detector and sky noise contributions get smeared out over the mosaic dither pattern, producing characteristic patterns in the skark mosaics and mosaic noise maps (see Figure 2).[23]

PAIRITEL SN observations did not include on-off pointings alternating between the source and a nearby sky field, so skark frames were created for each raw image in the mosaic by applying a pixel-by-pixel average through the stack of a time series of unregistered raw frames, after removing the highest and lowest pixel values in the stack. The stack used a time window of 5 minutes before and after each raw image. This approximation assumes that the sky is constant on timescales less than 10 minutes. For reference, typical dithered image sequences have effective exposure times of 10–30 minutes. Figure 2 shows that for J band, where the sky counts are small compared to the various sources of detector noise, the skark and noise mosaics are dominated by the cumulative effect of the intrinsic detector features over the entire dither pattern, including dark current, shading, and amplifier glow.[24] By contrast, the H- and K_s-band skark and noise mosaics in Figure 2 are dominated by sky counts and sky noise, respectively, which combine with the various detector imprints and spatiotemporal sky variation to produce the large-scale patterns smeared across the dither pattern.

Although the telescope is dithered ($<2'$) after three exposures at the same dither position, for host galaxies with large angular size $\gtrsim 2'$–$5'$ (in the $8\rlap{.}'53$ raw image FOV), host galaxy flux contamination introduces additional systematic uncertainty by biasing skark count estimates toward larger values, leading to *oversubtraction* of sky light in those pixels (F12). Still, the relatively large PAIRITEL $8\rlap{.}'53$ FOV combined with a dither step size comparable or greater than the $\sim 1'$–$2'$ angular size of typical galaxies at $z \sim 0.02$ allows us to safely estimate the sky from the raw frames in most cases.

[23] The shading is an electronic bias that technically produces no noise. Shading was subtracted out as part of the skark counts for each corresponding raw image. However, the shading was included as a generic background contribution along with thermal dark current, amplifier glow, and sky counts and thus effectively contributes to the noise mosaics in Figure 2.

[24] For further information on these features of NICMOS arrays, also used on the *Hubble Space Telescope* (*HST*), see http://documents.stsci.edu/hst/nicmos/documents/handbooks/v10/c07_detectors4.html or http://www.stsci.edu/hst/nicmos/documents/handbooks/DataHandbookv8/nic_ch4.8.3.html.

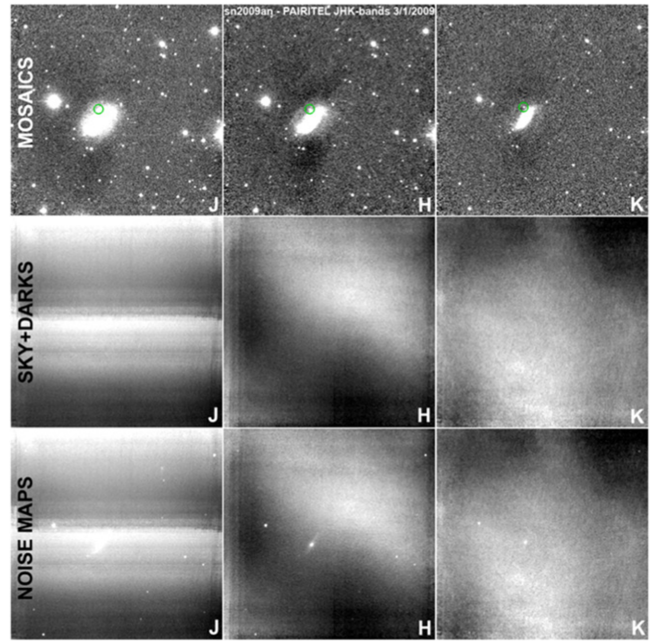

Figure 2. PAIRITEL Source, Skark, & Noise Mosaics. Mosaics (first row), skark mosaics (second row), and noise mosaics (third row) for the PAIRITEL JHK_s images of SN 2009an from 2009 March 1. The SN is marked with green circles. Images are displayed in SAOimage ds9 with zscale scaling, in grayscale with counts increasing from black to white. The skark images contain the number of sky + dark current + bias counts (skark counts) subtracted from each mosaic pixel. Median skark counts for these images were ∼800, 6700, and 19,600 counts in JHK_s, respectively, reflecting the sky noise increase toward longer NIR wavelengths, which is worst in K_s band. The large-scale patterns in the skark mosaics come from arcminute-scale spatial variations in the sky brightness of the raw frames, and both thermal dark current and amplifier glow, which peak at the corners of each detector quadrant, and which both contribute Poisson noise. The skark mosaics also show signatures of the relatively stable electronic bias shading patterns in each quadrant of the raw JHK_s detectors, which differ by bandpass. All of these contributions get smeared out over the mosaic dither pattern. Noise mosaics use source counts from the mosaic, skark counts from the skark mosaics, and noise from other sources (see Section 7.1 of F12 for assumptions used to estimate the noise per pixel). The large-scale patterns in the J-band skark and noise mosaics are dominated by the cumulative detector noise contributions, including thermal dark current, shading, and amplifier glow. By contrast, the H and K_s skark and noise mosaics are dominated by sky counts and sky noise, respectively, which combine with the various detector imprints and spatiotemporal sky variation across the dither pattern to form the large-scale patterns in those bandpasses.

This observing strategy also gives us more time on target compared to on-off pointing. While our approach can lead to systematic sky oversubtraction for SN and stars near larger galaxies, by testing the radial dependence of PAIRITEL photometry of 2MASS stars within $3'$ of the SN (and close to the host galaxy), we estimate this systematic error to be negligible compared to our photometric errors, biasing SN photometry fainter by $\lesssim 0.01$ mag in JH and $\lesssim 0.02$ in K_s (F12). By comparison, mean photometric errors for each of the highest-S/N LC points from the set of SN in CfAIR2 are ∼0.03, 0.05, and 0.12 mag in JHK_s, respectively (with larger mean statistical errors for all LC points of ∼0.09, 0.12, and 0.18 mag in JHK_s, respectively). We thus choose to ignore systematic errors from sky oversubtraction in this work.

Since three raw frames are taken at each dither position and co-added into triplestacks before mosaicking, `p3.6` now also constructs "tripleskarks," by co-adding the three associated skark frames taken at each dither position. To remove the estimated background counts, `p3.6` now subtracts the associated tripleskark from each triplestack before creating final mosaics and new skark and noise mosaics (see Figure 2). Since the estimated skark noise can vary by ∼10%–100% across individual skark mosaics, modeling the noise in each pixel provides more reliable *differential* noise estimates at the positions of all 2MASS stars and the SN, although our *absolute* noise estimate is still underestimated since the noise mosaics do not model all sources of uncertainty (see Section 7.1 of F12). To account for this, we also use 2MASS star photometry to empirically calculate inevitable noise underestimates and correct for them in SN photometry on subtracted or unsubtracted images (see F12; Section 4).

3.3. The PAIRITEL NIR Camera Is Undersampled

The PAIRITEL infrared camera is undersampled because the 2″ detector pixels are larger than the sub-arcsecond atmospheric seeing disk at FLWO. This means that we cannot fully sample the PSF of the detected image. To achieve some subpixel sampling, PAIRITEL implements a randomized dither pattern. While dithering can help recover some of the image information lost from undersampling, large pixels with dithered imaging cannot fully replace a fully sampled imaging system (Lauer 1999; Fruchter & Hook 2002; Rowe et al. 2011), and in practice, dithering does not always reliably produce the desired sub-pixel sampling. When we subtract host galaxy light, which requires PSF matching SN and SNTEMP mosaics, under-sampling leads to uncertainty in photometry for individual subtractions that can underestimate or overestimate the flux at the SN position. We correct for this by averaging many subtractions and removing bad subtractions, when producing CfAIR2 LCs (see Sections 3.4–3.7).

3.4. Host Galaxy Subtraction

We obtain SNTEMP images after the SN has faded below detection for the PAIRITEL infrared camera, typically $\gtrsim$6–12 months after the last SN observation. We use SNTEMP images to subtract the underlying host galaxy light at the SN position for each SN image that meets our image quality standards (see Sections 3.5–3.6). To limit the effects of variable observational conditions and sensitivity to individual template observations of poor quality and to minimize the photometric uncertainty from individual subtractions, we try to obtain at least $N_T = 2$, and as many as $N_T = 11$ SNTEMP images that satisfy our image quality requirements (see Section 3.7). In practice, we obtained medians of $N_T = 4$, 4, and 3 usable SNTEMP images in JHK_s, respectively (Figure 6). In cases with only $N_T = 1$ SNTEMP image, galaxy-subtracted LCs are deemed acceptable only for bright, well-isolated SN that are consistent with the unsubtracted LCs (see Sections 3.5, 4.2.2).

3.5. Forced DoPHOT on Unsubtracted Images

Forced DoPHOT photometry (Schechter et al. 1993) at a fixed position was performed on the unsubtracted SN images as an initial step for all PAIRITEL SN. Forced DoPHOT LCs on unsubtracted images provide an excellent approximation to the final galaxy-subtracted LCs for SN that were clearly separated from their host galaxy (F12). Approximately 30% of SN of all types observed by PAIRITEL are well isolated from the host galaxy and bright enough so that the measured galaxy flux at the SN position is $\lesssim$10% of the SN flux at peak brightness. We use 20 of these bright, well-isolated SN to perform internal consistency checks to test for errors incurred from host galaxy subtraction (see Section 4.2; F12).

3.6. Forced DoPHOT on Difference Images

We perform galaxy subtraction on all CfAIR2 objects to reduce the data with a homogeneous method.[25] We used subtraction-based photometry following Miknaitis et al. (2007). The SN flux in the difference images is measured with forced DoPHOT photometry at fixed pixel coordinates, determined by averaging SN centroids from *J*-band or CfA optical *V*-band difference images with photometric detections of the object that had an S/N > 5. SN centroids are typically accurate to within $\lesssim 0\farcs2$. Tests show no systematic LC bias for forced DoPHOT photometry as a result of SN astrometry errors if the SN centroid is accurate to within $\lesssim 0\farcs5$ (F12). The R.A. and decl. values in Tables 1 and 2 show best-fit SN centroid coordinates. These are typically more accurate than optical discovery coordinates from IAU/CBET notices, which may only be accurate to within $\lesssim 1''$–$2''$. Forced DoPHOT photometry at this fixed position in the difference images employs the DoPHOT PSF calculated from standard stars in the unconvolved image. For the difference images the calibrated zero point from the template is used, with suitable correction for the convolution of the SNTEMP image as detailed by Miknaitis et al. (2007).

3.7. Averaging Subtractions: NNT Method

We use NNT, an alternative galaxy subtraction method for CfAIR2, which uses fewer individual subtractions than the NN2 method (Barris et al. 2005) used in WV08. With NNT, for each of the N_{SN} mosaicked SN images, we subtract each of the usable N_T SNTEMP images, yielding at most $N_{NNT} = N_{SN} \times N_T$ individual subtractions. NNT yields N_T realizations of the LC that can be combined into a final galaxy-subtracted LC with a night-by-night weighted flux average after robust 3σ rejection and manual checks to exclude individual bad subtractions.[26] SN or SNTEMP images that failed our image quality requirements were also excluded from NNT via automatic photpipe tests and manual checks, yielding fewer bad subtractions than the purely automated process used in WV08.

By obtaining $1 \lesssim N_T \leqslant 11$ usable SNTEMP images, including additional observations since WV08, most CfAIR2 SN Ia have $N_T \gtrsim 4$ SNTEMP images suitable for galaxy subtraction (see Figure 6). NNT allowed us to exclude individual bad subtractions, average over variance across subtractions from different templates, and produce CfAIR2 SN Ia LCs with more accurate flux measurements compared to NN2 for WV08. We discuss the statistical and systematic uncertainty incurred from NNT host galaxy subtraction in Section 4.2. CfAIR2 NNT LCs also show better agreement with CSP photometry for the same objects compared to WV08 (see Section 4.3).[27]

[25] Only SN 2008A (and the SN 2005cf LC retained from WV08) use forced DoPHOT and no host subtraction. NNT failed for SN 2008A as a result of poor-quality SNTEMP images (see Section 3.7).

[26] Weighted mean flux values on each night are weighted by the corrected DoPHOT uncertainties. An S/N >1 cut is employed for individual subtractions before NNT. An S/N >3 cut is employed for final LC points. N_T can differ nightly and by bandpass and is often smallest in K_s. See Sections 4.1.2, 4.2.2, Table 6, and the Appendix.

[27] Some fainter SN Ia LCs that used NN2 in WV08 showed significant systematic deviations from the published CSP photometry for the same objects. These discrepancies exceeded deviations expected from small bandpass differences without S-corrections (Contreras et al. 2010; M. Phillips 2009–2010, private communication).

3.8. Photpipe Improvements

Since WV08, we have implemented several improvements to photpipe. Photpipe now takes p3.6 mosaics as input (see Section 3.1). To use SN that are not in the p3.6 mosaic center, photpipe uses larger-radius photometric catalogs and improved image masks (see F12). In WV08, our "skark" noise estimate was assumed to be constant throughout the mosaic (see Section 3.2). Figure 2 shows that this is a bad approximation. Instead, p3.6 noise mosaics are used by photpipe and fed as inputs to DoPHOT (Schechter et al. 1993), our point source photometry module, and HOTPANTS (Becker et al. 2004, 2007), our difference imaging module (see Section 3.4), leading to improved image subtraction. See F12 for details on the computational implementation of photpipe and p3.6.

As a result of improvements discussed throughout Section 3, CfAIR2 supersedes WV08 photometry for 20 out of 21 LCs (excluding SN 2005cf). CfAIR2 and WV08 photometry agree best for the brightest, well-isolated SN with little galaxy light at the SN position. Fainter SN that required significant host galaxy subtraction show the most disagreement between CfAIR2 and WV08 due mainly to the differences between NN2 and NNT (see Section 4.3.1 of F12). Problems with WV08 NN2 photometry are most evident in the set of nine WV08 SN also observed by the CSP, which are discussed in Section 4.3. The improved agreement between CfAIR2 and CSP (see Section 6) gives evidence that CfAIR2 photometry is superior to WV08.

Although individual LCs show differences between CfAIR2 and WV08 data, we do not expect the revised photometry to significantly affect the overall conclusions of WV08. Preliminary analysis, which will be presented elsewhere, will derive mean NIR LC templates and mean absolute magnitudes using only normal CfAIR2 SN Ia and compare these to mean templates derived using only 18 normal PAIRITEL SN Ia from WV08.

4. PHOTOMETRIC CALIBRATION AND VERIFICATION

We now discuss the methods used to calibrate PAIRITEL photometry and test the calibration, including internal consistency checks and comparison with external data sets with NIR photometry for the same objects. In Section 4.1, we present PAIRITEL photometry for 2MASS stars, which we use to test for systematic problems with PAIRITEL DoPHOT photometry. In Section 4.2, we investigate potential systematic photometry errors from host galaxy subtraction. In Section 4.3, we compute approximate color terms describing offsets between PAIRITEL and CSP J and H bandpasses using 2MASS field stars observed by both groups. In Section 4.4, we compare CfAIR2 data with an overlapping subset of CSP SN Ia photometry, demonstrating overall agreement between the data sets. Throughout, we refer to F12 for additional details.

4.1. Photometric Calibration

We organize Section 4.1 as follows. In Section 4.1.1, we present PAIRITEL mean photometric measurements and uncertainties for all 2MASS stars for 118 out of 121 SN Ia and SN Iax fields observed from 2005 to 2011. In Section 4.1.2, we test whether DoPHOT is correctly estimating photometric uncertainties for PAIRITEL point sources. In Section 4.1.3, we assess whether PAIRITEL DoPHOT photometry globally agrees with 2MASS star photometry. Overall, Sections 4.1.2 and 4.1.3 test the precision and accuracy of DoPHOT photometry on unsubtracted PAIRITEL images. We find no significant systematic differences with 2MASS.

4.1.1. PAIRITEL Photometry of 2MASS Standard Stars

For 121 PAIRITEL SN fields observed from 2005 to 2011, including 23 objects not in CfAIR2, we performed DoPHOT photometry on all 2MASS stars to measure the photometric zero point for each image. In a typical $12' \times 12'$ p3.6 mosaic FOV, there were between 6 and 92 2MASS stars in each filter (see Figures 3–5). While the exact coverage for a mosaic during a given night varies (see Section 3.1), the majority of the 2MASS stars are covered by each observation of a given SN field. Fewer 2MASS stars are detected by DoPHOT as wavelength increases from J to H to K_s. For all SN Ia or SN Iax fields with at least five mosaic images, the mean number of 2MASS stars was 39, 38, and 34 in JHK_s, respectively (see Table 4.1 of F12).

We interpret the error on the weighted mean of the PAIRITEL photometric measurements to be the uncertainty in the measurement of the mean PAIRITEL magnitude for that 2MASS star (see Sections 4.1.2 and 7.3 of F12 for mathematical details). Table 5 presents weighted mean PAIRITEL photometric measurements and uncertainties for all 2MASS stars in 118 SN fields observed by PAIRITEL. A global comparison of PAIRITEL and 2MASS star measurements is presented in Sections 4.1.2 and 4.1.3.

4.1.2. Photometric Precision

We assess the repeatability of DoPHOT measurements of 2MASS stars to quantify the photometric precision of PAIRITEL. This tests whether we have correctly estimated our *uncertainties* for point sources measured on individual nights. Although a small fraction of 2MASS stars are variable (Plavchan et al. 2008; Quillen et al. 2014), by averaging over $\gtrsim$4000 2MASS stars for each filter (see Table 5) and removing outlier points, we do not expect this to significantly affect our results. Assuming that 2MASS stars have constant brightness, the measured scatter indicates whether the PAIRITEL DoPHOT uncertainties are under- or overestimated. Because we do not model all known sources of uncertainty in computing our noise mosaics (see Sections 3.2 and 7.1 of F12), we expect to underestimate our photometric errors. Empirical tests using DoPHOT photometry of 2MASS stars in the unsubtracted images confirm that we are underestimating our photometric magnitude uncertainties by factors of ~1.5–3, depending on the brightness of the point source and the filter (F12). We then multiply the uncorrected DoPHOT magnitude uncertainties ($\sigma_{\rm do}$) for individual points in the SN Ia LCs by this empirically measured, magnitude-dependent correction factor C. Corrected DoPHOT magnitude uncertainties are given by $\tilde{\sigma}_{\rm do} = C \times \sigma_{\rm do}$ (see Section 4 of F12).

4.1.3. Photometric Accuracy

We test whether PAIRITEL and 2MASS star photometries are consistent within the estimated uncertainties *after* correcting the PAIRITEL DoPHOT uncertainties as discussed in Section 4.1.2. This tests the photometric accuracy of PAIRITEL to identify any statistically significant systematic offsets from 2MASS. We expect mean PAIRITEL and 2MASS photometry to agree when averaged over many stars *by construction*, so this is a self-

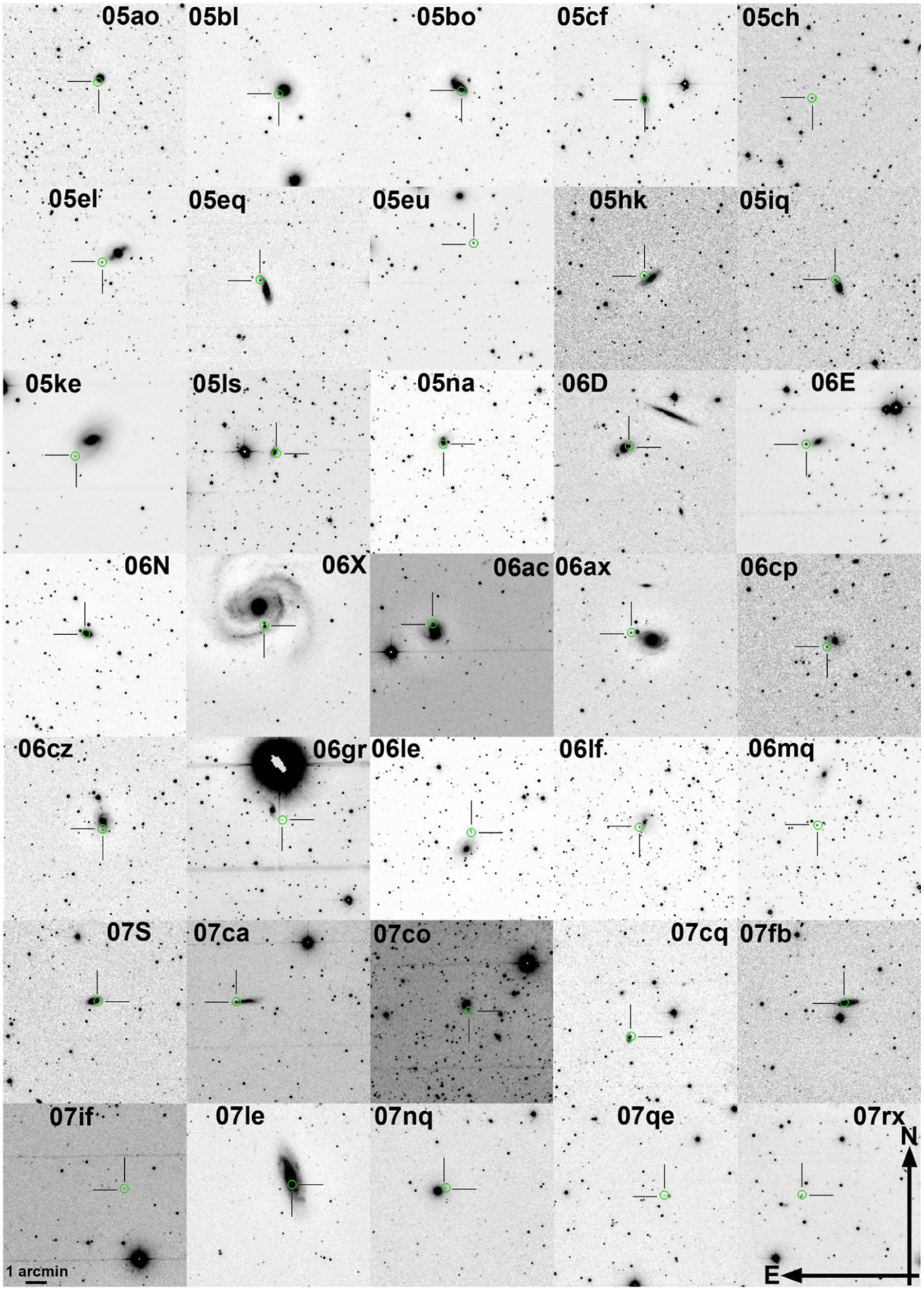

Figure 3. Gallery of 35 PAIRITEL *J*-band Mosaics. A subset of 35 PAIRITEL *J*-band mosaics from the set of 94 CfAIR2 SN Ia and 4 SN Iax observed with PAIRITEL from 2005 to 2011. SN Ia or SN Iax are marked by green circles and crosshairs. SN names are of the shortened form 06X = SN 2006X. North and east axes for all mosaics are indicated in the lower right corner of the figure.

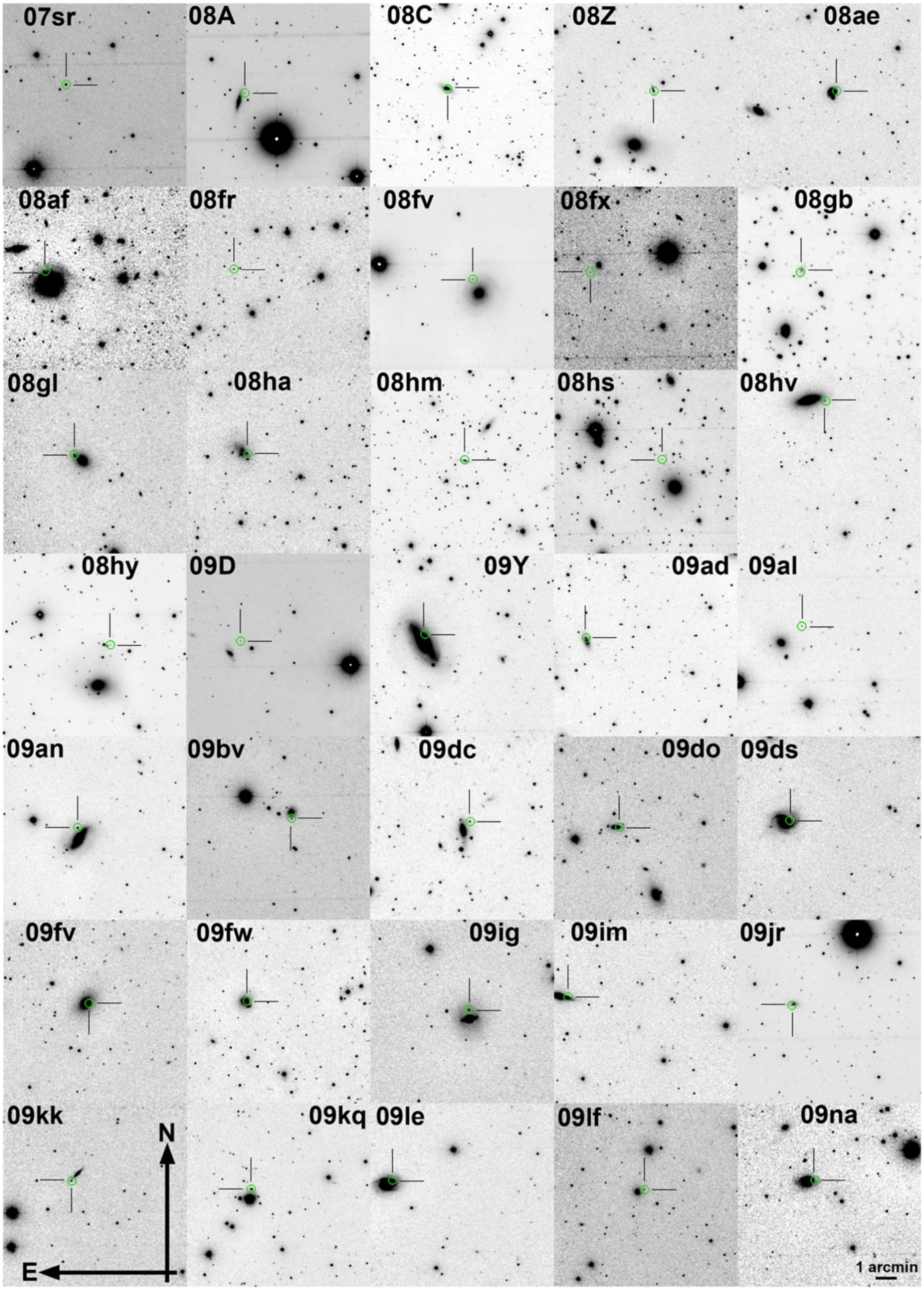

Figure 4. Gallery of 35 PAIRITEL *J*-band Mosaics. A subset of 35 PAIRITEL *J*-band mosaics from the set of 94 CfAIR2 SN Ia and 4 SN Iax observed with PAIRITEL from 2005 to 2011. SN Ia or SN Iax are marked by green circles and crosshairs. SN names are of the shortened form 09an = SN 2009an. North and east axes for all mosaics are indicated in the lower left corner of the figure.

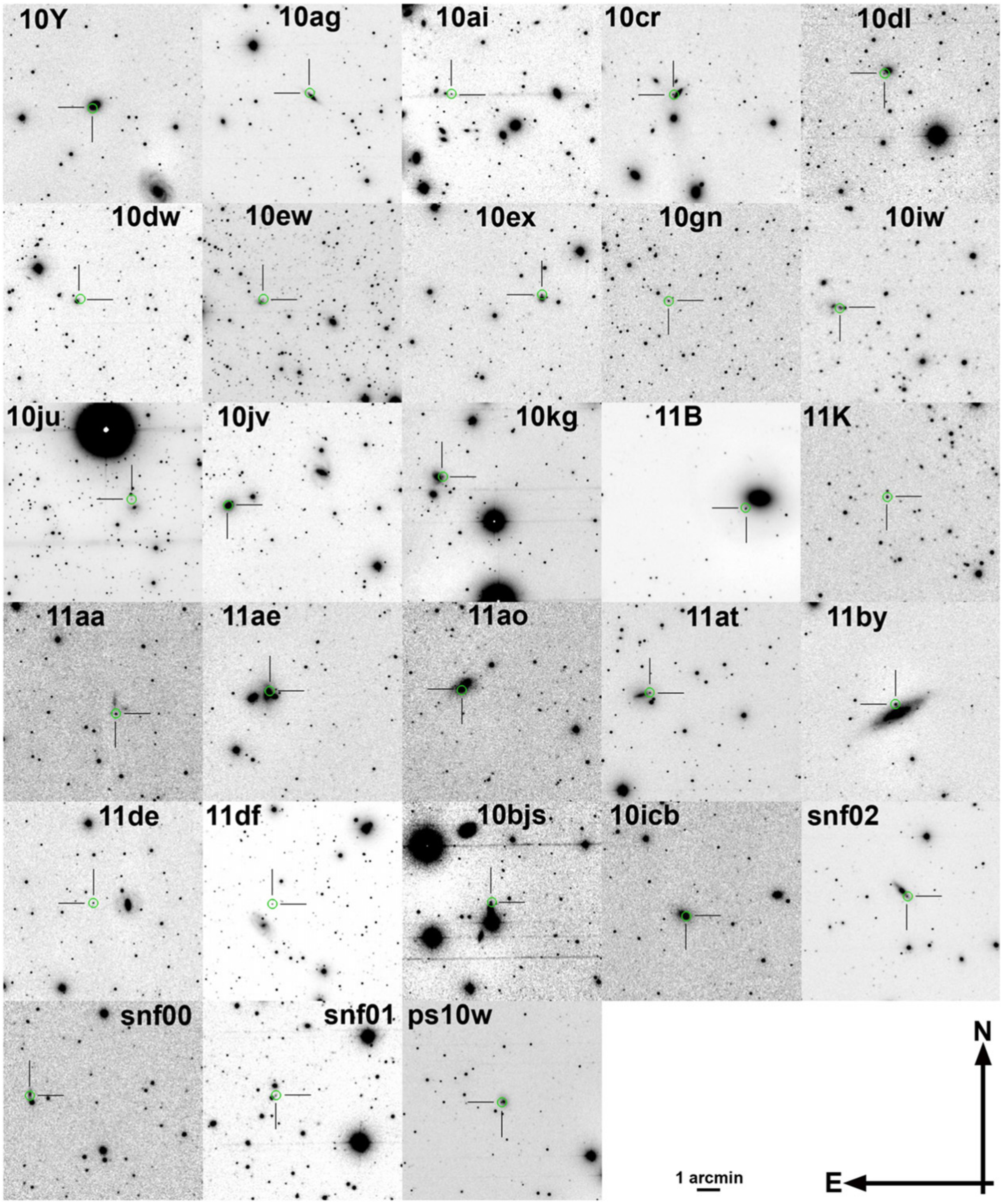

Figure 5. Gallery of 28 PAIRITEL *J*-band Mosaics. A subset of 28 PAIRITEL *J*-band mosaics from the set of 94 CfAIR2 SN Ia and 4 SN Iax observed with PAIRITEL from 2005 to 2011. SN Ia or SN Iax are marked by green circles and crosshairs. SN names are of the shortened form 06X = SN 2006X. North and east axes for all mosaics are indicated in the lower right corner of the figure. Non-IAUC SN names include: 10bjs = PTF10bjs, 10icb = PTF10icb, snf02 = SNF20080514-002, snf00 = SNF20080522-000, snf01 = SNF20080522-011, ps10w = PS1-10w.

consistency check to rule out any glaring systematic problems with PAIRITEL DoPHOT photometry. For these tests, we measure the difference between the weighted mean PAIRITEL magnitudes for each star and the 2MASS catalog magnitudes in Table 5. Because PAIRITEL photometry goes deeper than 2MASS for each image and the weighted mean PAIRITEL magnitude of each 2MASS star is determined from measurements over many nights, we do not expect the 2MASS catalog magnitude and the weighted mean PAIRITEL magnitude to be strictly equal for all standard stars. We expect greatest agreement for the brightest 2MASS stars with decreasing agreement and increased scatter as the 2MASS catalog brightness decreases, consistent with measurements drawn from a distribution with Gaussian uncertainties. See Section 4 of F12.

Table 5
PAIRITEL JHK_s Photometry of 2MASS Standard Stars in SN Ia Fields

SN[a]	Star[b]	α(2000)[c]	δ(2000)[c]	N_J	$m_J^{\rm PTL}$ (mag)[e]	$\sigma_{mJ}^{\rm PTL}$[d] (mag)[f]	$m_J^{\rm 2M}$ (mag)[g]	$\sigma_{mJ}^{\rm 2M}$ (mag)[g]	N_H[d]	$m_H^{\rm PTL}$ (mag)[e]	$\sigma_{mH}^{\rm PTL}$ (mag)[f]	$m_H^{\rm 2M}$ (mag)[g]	$\sigma_{mH}^{\rm 2M}$ (mag)[g]	N_K[d]	$m_K^{\rm PTL}$ (mag)[e]	$\sigma_{mK}^{\rm PTL}$ (mag)[f]	$m_K^{\rm 2M}$ (mag)[g]	$\sigma_{mK}^{\rm 2M}$ (mag)[g]
SN 2005ak	01	14:40:18.45	+03:30:55.44	34	16.549	0.007	16.504	0.159	35	15.940	0.009	16.024	0.183	30	15.675	0.012	15.251	0.173
SN 2005ak	02	14:40:18.56	+03:34:12.76	34	15.918	0.006	15.858	0.097	33	15.230	0.008	15.230	0.105	33	15.024	0.010	15.075	0.148
SN 2005ak	03	14:40:19.41	+03:30:22.95	34	15.112	0.006	15.118	0.056	35	14.768	0.007	14.822	0.085	33	14.686	0.008	14.814	0.112
SN 2005ak	04	14:40:20.77	+03:27:36.99	34	16.404	0.006	16.430	0.150	35	15.793	0.009	16.057	0.219	34	15.549	0.012	15.326	0.197
SN 2005ak	05	14:40:20.94	+03:33:41.82	33	15.013	0.006	15.071	0.049	34	14.408	0.007	14.511	0.071	34	14.301	0.007	14.285	0.074
SN 2005ak	06	14:40:22.26	+03:31:18.61	33	17.032	0.007	16.521	0.147	33	16.386	0.010	16.101	0.215	29	16.153	0.014	15.598	0.255
SN 2005ak	07	14:40:22.58	+03:32:56.39	35	15.637	0.006	15.665	0.066	35	15.001	0.007	15.133	0.089	34	14.765	0.008	14.946	0.148
SN 2005ak	08	14:40:26.00	+03:31:41.52	34	13.255	0.005	13.233	0.024	35	12.617	0.006	12.608	0.030	35	12.406	0.007	12.404	0.032
SN 2005ak	09	14:40:26.55	+03:30:58.65	34	14.780	0.006	14.762	0.037	35	14.212	0.007	14.121	0.035	35	13.967	0.007	14.003	0.071
SN 2005ak	10	14:40:29.45	+03:32:34.68	35	16.402	0.006	16.596	0.163	35	15.757	0.008	15.736	0.152	32	15.571	0.011	15.228	0.173
SN 2005ak	11	14:40:29.89	+03:28:05.44	33	14.455	0.006	14.444	0.038	34	14.160	0.006	14.114	0.035	33	14.055	0.007	14.095	0.072
SN 2005ak	12	14:40:30.02	+03:30:15.93	34	15.424	0.005	15.319	0.072	33	14.958	0.007	15.021	0.090	35	14.793	0.008	14.624	0.123
SN 2005ak	13	14:40:31.33	+03:28:33.93	24	15.472	0.010	15.589	0.082	28	14.814	0.011	15.169	0.100	31	14.488	0.010	14.898	0.150
SN 2005ak	14	14:40:31.52	+03:32:31.31	36	14.373	0.005	14.367	0.036	36	14.171	0.007	14.212	0.042	36	14.145	0.007	14.277	0.086
SN 2005ak	15	14:40:31.74	+03:29:10.30	35	15.420	0.006	15.304	0.056	34	14.804	0.007	14.823	0.070	35	14.574	0.008	14.704	0.116
SN 2005ak	16	14:40:32.31	+03:31:13.54	34	16.087	0.006	15.902	0.090	36	15.501	0.008	15.476	0.132	…	…	…	…	…
SN 2005ak	17	14:40:32.43	+03:33:34.39	28	14.766	0.010	14.756	0.056	26	14.069	0.012	14.143	0.085	29	13.836	0.011	13.802	0.070

Notes.
[a] Tables like the above sample are provided online for 118 out of 121 SN Ia and SN Iax fields observed with PAIRITEL from 2005 to 2011 (SN 2005ak-SN 2011df), including 23 SN Ia without CfAIR2 photometry (e.g., SN 2005ak above). Tables include weighted mean PAIRITEL photometry and uncertainties for all 2MASS stars in each SN Ia field. Three SN Ia are not included in Table 5 as a result of unresolved software errors: SN 2008fv, SN 2008hs (in CfAIR2), and SN 2011ay (not in CfAIR2).
[b] Superscripts PTL and 2M denote PAIRITEL and 2MASS, respectively. Missing data are denoted by ….
[c] R.A. (α) and decl. (δ) for Epoch 2000 in sexagesimal coordinates.
[d] N_X is the number of PAIRITEL SN images in band $X = J$, H, K with this standard star used to measure $m_X^{\rm PTL}$ and $\sigma_{mX}^{\rm PTL}$.
[e] PAIRITEL apparent brightness in magnitudes $m_X^{\rm PTL}$ is computed as the weighted mean PAIRITEL magnitude over all N_X SN images with that 2MASS star.
[f] PAIRITEL magnitude uncertainty $\sigma_{mX}^{\rm PTL}$ is computed as the error on the weighted mean of the N_X measurements, each of which has already been corrected for DoPHOT uncertainty estimates as described in Section 4.1.2 and F12. (See Section 7.3 of F12.)
[g] The 2MASS magnitudes $m_X^{\rm 2M}$ and uncertainties $\sigma_{mX}^{\rm 2M}$ for each star are from the 2MASS point source catalog (Cutri et al. 2003).

(This table is available in its entirety in machine-readable form.)

Aggregated PAIRITEL-2MASS residuals for all 2MASS stars in 121 PAIRITEL SN fields yield weighted mean residuals of 0.0014 ± 0.0006, 0.0014 ± 0.0007, and -0.0055 ± 0.0007 in JHK_s, respectively (uncertainties are standard errors of the mean). Thus, when averaging over thousands of stars observed over a 6 yr span from 2005 to 2011, PAIRITEL and 2MASS agree to within a few thousandths of a magnitude in JHK_s, with evidence for small but statistically significant PAIRITEL-2MASS offsets of ~0.001, 0.001, and −0.006 mag in JHK_s, respectively, at the ~2–3σ level. If we correct for the slight underestimate of our uncertainties in the PAIRITEL-2MASS residuals, we find that ~68%, ~95%, and ~99% of the standard stars have PAIRITEL-2MASS residuals consistent within 0 to 1, 2, and 3σ respectively, as expected with correctly estimated Gaussian errors (see Section 7.4 of F12).

4.2. Photometry Systematics

In Section 4.2, we discuss internal consistency tests to assess other potential statistical and systematic errors with the photometry. In Sections 4.2.1–4.2.3, we evaluate our most important systematic and statistical uncertainty from the NNT host galaxy subtraction process, both for bright, well-isolated objects and for objects superposed on the nucleus or spiral arms of host galaxies. See Section 4 of F12 for discussions of systematic errors from sky subtraction and astrometric errors in the best-fit SN centroid position.

4.2.1. Galaxy Subtraction: Statistical and Systematic Errors

When subtracting SN and SNTEMP images observed under different seeing conditions, undersampling of the PAIRITEL NIR camera introduces uncertainties into both the estimates of the PSF and convolution kernel solution when attempting to transform the SN or SNTEMP image to the PSF of the other. This leads to flux being added or subtracted from photometry on individual subtractions. While NNT attempts to correct for this by averaging over many subtractions, there is always remaining uncertainty as a result of undersampling (see Section 3).

For an individual night of photometry, we conservatively estimate the statistical uncertainty from NNT, $\sigma_{\rm NNT}$, as the error-weighted standard deviation of the input flux measurements, weighted by the corrected DoPHOT flux uncertainties for each of the $N_{\rm T}$ subtractions (for details see Section 3 and the Appendix). For cases where only $N_{\rm T} = 1$ or 2 subtractions survive both the pipeline's cuts and any manual rejection, NNT flux estimates can be biased high or low and either the weighted standard deviation cannot be computed or it is not a reliable estimate of the statistical uncertainty. To ensure accurate photometric uncertainties for these cases—at the expense of reduced photometric precision—we adopt a conservative systematic error floor of 0.25 and 0.175 mag for $N_{\rm T} = 1$ and $N_{\rm T} = 2$, respectively. Final galaxy-subtracted uncertainties $\tilde{\sigma}_{\rm NNT}$ are computed as in Table 6, which includes a final S/N cut of >3. Thus, when a given LC point has an uncertainty larger than its neighbors, either only one or two good subtractions were used or the scatter among the surviving three-plus subtractions was large.

In Sections 4.2.2 and 4.2.3, both for bright, well-isolated objects and SN superposed on the host galaxy, NNT produces no net systematic bias given $N_{\rm T} \gtrsim 3$–4 usable host galaxy templates. For fainter objects, SN superposed on the host galaxy nucleus, or SN with insufficient high-quality SNTEMP images, the additional uncertainty from host galaxy subtraction can yield many LC points that are excluded based on S/N cuts, outlier rejection, or final quality checks, sometimes yielding LCs of insufficient quality for publication or cosmological analysis.

Table 6
Computing NNT Errors

$N_{\rm T}$	$\tilde{\sigma}_{\rm NNT}$ mag Error	S/N	Note
1	max(0.25 mag, $\sigma_{\rm NNT}$)	3 < S/N < ~4.2	a
2	max(0.175 mag, $\sigma_{\rm NNT}$)	3 < S/N < ~5.5	
3+	$\sigma_{\rm NNT}$	3 < S/N	b

Notes.
[a] If $N_{\rm T} = 1$, $\sigma_{\rm NNT} = \tilde{\sigma}_{\rm do}$, the corrected DoPHOT error for a single subtraction.
[b] An S/N >1 cut is used before NNT averaging. An S/N > 3 cut is placed on the final NNT LC points.

4.2.2. Galaxy Subtraction for Bright, Well-Isolated Objects

To test whether NNT biases the photometry, we first use SN that are well isolated from their host galaxy nuclei. In these cases, photometry on the unsubtracted images gives a good approximation to the final galaxy-subtracted LC at most phases, providing an internal consistency check of NNT. We use bright SN for which the host galaxy flux at the SN position is a small fraction of the SN flux in the [−10, 50] day phase range, including 20 bright and/or well-isolated SN of all types (see Section 4 of F12). We test whether the weighted mean residuals of the unsubtracted and subtracted LCs are consistent with zero to within the standard deviation of the residuals in this phase range, which are each only ~0.001–0.002 mag, depending on the filter. After removing 3σ outliers and S/N < 3 points, the weighted means of the aggregated residuals for all 20 SN are consistent with 0 by this measure, with weighted means and standard deviations of the residuals of -0.0009 ± 0.0016, 0.0006 ± 0.0019, and 0.0007 ± 0.0026 magnitudes in JHK_s, respectively. At least for bright, well-isolated objects with sufficient host galaxy templates, NNT does not introduce a net bias in the photometry.

4.2.3. Galaxy Subtraction for Superposed SN

For SN superposed on the host galaxy, we cannot make the same comparison in the absence of a suitable unsubtracted reference LC. In these cases, we test the subtraction process by performing forced DoPHOT NNT photometry on the galaxy-subtracted difference images at positions near the host galaxy. We perform forced photometry on a 3 × 3 grid of positions with evenly spaced increments of 15″ = 15 pixels centered around the SN position. At least some of these nine grid positions are likely to be superposed on the galaxy. If the subtraction process is working correctly (no net bias), the difference image LCs should have a weighted mean of zero flux at all grid positions *except* for the central position with the SN, albeit with larger scatter for grid positions superposed on the galaxy (see Section 4 of F12).

We performed this test for all SN fields. The standard deviation of the difference image flux values for each LC is used to estimate the uncertainty in the measured flux at each grid position.[28] For all CfAIR2 objects, grid positions offset from the SN showed weighted mean flux consistent with zero to within 1–3 standard deviations. Highly embedded SN fainter than $J \sim 18$–19 mag at the brightest LC point are often too faint for PAIRITEL, and NNT can yield LCs with inaccurate flux values that are not suitable for publication. However, if $N_{\rm T} \gtrsim$ 3–4 host galaxy template images are obtained for sufficiently bright SN that reach $J \lesssim 18$ mag, NNT galaxy subtraction yields a net bias of $\lesssim$0.01 mag even at positions clearly superposed on host galaxies.

4.2.4. NNT versus Forced DoPHOT Errors

NNT can lead to larger reported errors ($\sigma_{\rm NNT}$) compared to corrected DoPHOT point source photometry without galaxy subtraction ($\tilde{\sigma}_{\rm do}$) for cases with $N_{\rm T} \lesssim$ 2–3, owing primarily to our imposed systematic error floor for these cases (see Table 6). However, for cases with $N_{\rm T} \gtrsim$ 3–4 templates, $\sigma_{\rm NNT} \lesssim \tilde{\sigma}_{\rm do}$ and NNT performs as well as or better than DoPHOT without host subtraction as a result of the effective division by $\sim \sqrt{N_{\rm T}}$ inside the error-weighted standard deviation used to compute $\sigma_{\rm NNT}$ (see the Appendix). Figure 7 shows median magnitude uncertainties for both the highest-S/N LC points for each SN and all LC points for both forced DoPHOT and NNT photometry. The spikes in the NNT error distributions are artifacts of our systematic error floor chosen for cases with $N_{\rm T} = 1$–2 SNTEMP images.

4.3. Comparing PAIRITEL and CSP Photometry

Comparing PAIRITEL CfAIR2 NNT LCs with published CSP photometry for the same SN Ia provides an important external consistency check. Although CfA and CSP observatories with NIR detectors are in the northern and southern hemispheres, respectively, an overlapping subset of 18 CfAIR2 objects in the declination range $-24.94410 < \delta < 25.70778$ were observed in JHK_s by both groups (see Table 7 and Figures 10–12).[29] Similar to Tables 1 and 2 of this paper, Table 1 of Contreras et al. (2010, hereafter C10) and Table 1 of Stritzinger et al. (2011, hereafter S11) present general properties of 35 and 50 SN Ia observed by the CSP, respectively. Some CSP SN Ia had only optical observations and no NIR data.[30] The 18 CSP NIR objects independently observed by PAIRITEL include 14 normal SN Ia, 1 peculiar, fast-declining object, 2 overluminous, slowly declining objects, and 1 SN Iax . Of these, 9 had data published in WV08 and 9 are new to CfAIR2. See Table 7.

4.3.1. CSP–PAIRITEL Offsets and Color Terms

Cohen et al. (2003) and Skrutskie et al. (2006) describe the 2MASS JHK_s filter system, while Carpenter (2001) and Leggett et al. (2006) provide color transformations from other widely used photometric systems to 2MASS. The PAIRITEL/2MASS JHK_s bandpasses are very similar to the CSP JHK_s filters, so it is a reasonable approximation to compare the LCs directly, without first attempting to transform the CSP data to the 2MASS system. However, to justify this approximation, following C10, we investigate whether there exist non-negligible zero-point offsets or color terms between PAIRITEL and CSP NIR filters using 2MASS stars in fields observed by both groups. While C10 compared CSP measurements of 2MASS stars to the 2MASS point source catalog (Cutri et al. 2003), here we also compare CSP and PAIRITEL measurements of 2MASS stars from Table 5 to derive zero-point estimates and color terms to approximately transform CSP natural system data to the 2MASS system. Although PAIRITEL is on the 2MASS natural system, PAIRITEL observations are deeper than 2MASS, so PAIRITEL measurements of 2MASS stars are more appropriate than 2MASS catalog data for estimating differences between PAIRITEL and CSP photometry.

4.3.2. Zero-point Offsets from 2MASS Star Photometry

C10 used CSP photometric measurements of 984 J- and H-band 2MASS stars in their SN fields, finding these mean zero point offsets between the CSP Swope 1.0 m natural system and the 2MASS J and H filters:

$$J_{\rm CSP} - J_{\rm 2M} = 0.010 \pm 0.003 \text{ mag},$$
$$H_{\rm CSP} - H_{\rm 2M} = 0.043 \pm 0.003 \text{ mag}. \quad (1)$$

C10 did not derive zero-point offsets in K_s because they had only 41 CSP 2MASS star observations in K_s.

For 19 objects observed by both PAIRITEL and CSP (including SN 2006is, which is not in CfAIR2), we obtained CSP standard-star photometry for the local sequences for 16 objects from the literature (C10; S11; Taubenberger et al. 2011) and three additional objects from the CSP (M. Stritzinger 2012–2013;, private communication; see Section 4.33 of F12). In these 19 SN fields, we used 269, 264, and 24 2MASS stars observed by both PAIRITEL and CSP in JHK_s, respectively, limited to the color range $0.2 < (J-H)_{\rm CSP} < 0.7$ mag also used by C10. We compute CSP–PAIRITEL residuals for each 2MASS star in JHK_s and interpret the weighted mean residuals and the error on the weighted mean as our estimate of the zero-point offset and uncertainty between the CSP natural system (JH Swope, K_s du Pont) and the PAIRITEL/2MASS JHK_s system. Although column 6 of Table 5 reports uncertainties on the weighted mean PAIRITEL magnitudes of 2MASS stars as the error on the weighted mean, we follow the method reported by the CSP here and instead use the rms to estimate our local sequence uncertainties (C10; S11), which yield larger, more conservative error estimates.

Using the rms error for PAIRITEL measurements of 2MASS stars, we find zero-point offsets of

$$J_{\rm CSP} - J_{\rm PTL} = 0.018 \pm 0.002 \text{ mag},$$
$$H_{\rm CSP} - H_{\rm PTL} = 0.038 \pm 0.003 \text{ mag},$$
$$K_{s\,\rm CSP} - K_{s\,\rm PTL} = 0.077 \pm 0.011 \text{ mag}. \quad (2)$$

The JHK_s CSP–PAIRITEL zero-point offsets from Equation (2) are also shown in Figure 8 and agree with those from C10 in Equation (1) to within 2σ in J and 1σ in H. While C10

[28] The scatter also increases toward longer wavelength since the S/N decreases from J to H to K as a result of the presence of additional contaminating sky noise (see Section 3.2).

[29] The latitudes and longitudes of the PAIRITEL and CSP observatories are (FLWO: 31.6811°N, 110.8783°W) and (LCO: 29.0146°S, 70.6926°W), respectively. PAIRITEL observes objects with $\delta \gtrsim -30°$.

[30] All PAIRITEL and CSP SN Ia with NIR overlap are included in CfAIR2 except SN 2006is (CSP NIR data in S11) and SN 2005mc (CSP optical data in C10), which had poor-quality PAIRITEL LCs. Two other SN Ia (SN 2005bo, SN 2005bl) have PAIRITEL JHK_s observations in CfAIR2 and CSP optical observations but no CSP NIR data (SN 2005bl: Taubenberger et al. 2008; SN 2005bo: C10) and are not included in the PAIRITEL and CSP NIR comparison set. SN 2005bl was also included in WV08.

Table 7
18 NIR SN Ia Observed by PAIRITEL and CSP

SN[a]	Type[b]	ΔJ (mag)[c]	ΔH (mag)[c]	ΔK_s (mag)[c]	Agree?[d]	CSP Refs[e]
SN 2005el	Ia	0.032 ± 0.026	0.042 ± 0.018	0.078 ± 0.024	234	(1)
SN 2005eq	Ia	−0.010 ± 0.030	−0.003 ± 0.024	−0.034 ± 0.030	112	(1)
SN 2005hk	Iax	−0.031 ± 0.027	−0.012 ± 0.028	0.050 ± 0.048	212	(3)
SN 2005iq	Ia	−0.025 ± 0.029	0.080 ± 0.060	−0.077 ± 0.045	122	(1)
SN 2005ke	Iap	−0.001 ± 0.014	−0.001 ± 0.014	0.010 ± 0.020	111	(1)
SN 2005na	Ia	−0.059 ± 0.030	−0.000 ± 0.023	⋯	21	(1)
SN 2006D	Ia	0.003 ± 0.011	−0.006 ± 0.014	0.000 ± 0.010	111	(1)
SN 2006X	Ia	0.009 ± 0.018	0.006 ± 0.011	−0.007 ± 0.010	111	(1)
SN 2006ax	Ia	−0.026 ± 0.014	0.003 ± 0.005	0.007 ± 0.018	211	(1)
SN 2007S	Ia	0.029 ± 0.023	0.015 ± 0.020	0.006 ± 0.024	211	(2)
SN 2007ca	Ia	0.004 ± 0.012	0.036 ± 0.025	⋯	12	(2)
SN 2007if	Iap	0.058 ± 0.033	0.053 ± 0.038	⋯	22	(2)
SN 2007le	Ia	0.015 ± 0.013	0.006 ± 0.008	⋯	21	(2)
SN 2007nq	Ia	0.004 ± 0.020	0.000 ± 0.054	⋯	11	(2)
SN 2007sr	Ia	0.022 ± 0.017	0.017 ± 0.012	⋯	22	(4)
SN 2008C	Ia	−0.004 ± 0.018	−0.001 ± 0.018	⋯	11	(2)
SN 2008hv	Ia	0.024 ± 0.024	0.011 ± 0.020	⋯	21	(2)
SN 2009dc	Iap	−0.004 ± 0.019	−0.006 ± 0.015	−0.002 ± 0.019	111	(5)

Notes.
[a] All SN LCs use NNT galaxy subtraction (see Section 3.7). The horizontal line in the middle of the table divides the nine PAIRITEL SN with CfAIR2 data that supersede WV08 data (top: SN 2005el-SN 2006ax) from the nine SN with PAIRITEL data new to this work (bottom: SN 2007S-SN 2009dc).
[b] Ia: spectroscopically normal. Iap: peculiar, underluminous (SN 2005ke), peculiar overluminous (SN 2007if, SN 2009dc). Iax: 02cx-like (SN 2005hk).
[c] Weighted mean CSP–CfAIR2 residuals and 1σ errors, estimated by the error-weighted standard deviation of the residuals divided by 3. K_s-band data not available for some CSP SN Ia.
[d] Do CSP–CfAIR2 weighted mean residuals agree within 1, 2, or 3σ for JHK_s, respectively? For example, 132 would mean the NIR LCs agree in J within 1σ, H within 3σ, and K_s within 2σ. All 18 LCs in JH and all 8 in K_s agree within at least 3σ by this metric (except for SN 2005el, K_s, which agrees at 4σ).
[e] CSP References: (1) Contreras et al. (2010), (2) Stritzinger et al. (2011), (3) Phillips et al. (2007), (4) Schweizer et al. (2008), (5) Taubenberger et al. (2011).

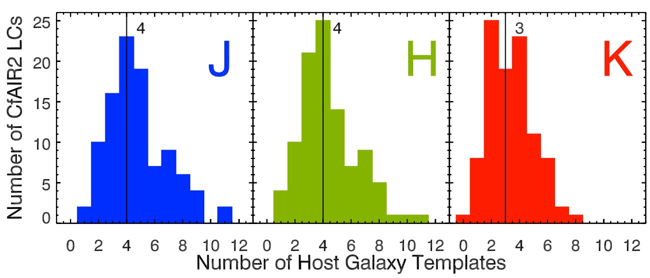

Figure 6. Histograms of JHK_s SNTEMP Subtractions. Histogram of the number of host galaxy template images N_T in each bandpass used for each SN. N_T is the maximum number of SNTEMP subtractions used over all nights per LC and bandpass. Some subtractions fail during `photpipe` or are rejected as bad subtractions on individual nights during post-processing. We generally obtain $>N_T$ host galaxy images, but some images fail the mosaicking pipeline (especially in K_s band) prior to `photpipe`. We tried to obtain at least $N_T = 2$, and as many as $N_T = 11$ usable SNTEMP images, with medians of $N_T = 4$, 4, and 3 SNTEMP images in JHK_s, respectively. For some SN, only $N_T = 1$ template images were usable and SN 2008A had no usable SNTEMP images.

used ~3–4 times as many 2MASS stars, Equation (1) technically estimates the offsets between CSP and 2MASS, not the offsets between CSP and PAIRITEL given by Equation (2). Since we are most interested in the latter, and since we do not consider the slight differences between Equations (1) and (2) to be significant, we simply use our own offsets from Equation (2) as needed. We do not consider the zero-point offset for K_s in Equation (2) to be reliable, since it is based on only 24 2MASS stars measured by both groups.

4.3.3. CSP–PAIRITEL Color Terms

Considering only 2MASS stars in the color range $0.2 < (J-H)_{\rm CSP} < 0.7$ mag, C10 obtained the following linear fits for the JH bands:

$$\begin{aligned} J_{\rm CSP} - J_{\rm 2M} &= (-0.045 \pm 0.008) \times (J-H)_{\rm CSP}, \\ &\quad + (0.035 \pm 0.067)\ {\rm mag}, \\ H_{\rm CSP} - H_{\rm 2M} &= (0.005 \pm 0.006) \times (J-H)_{\rm CSP} \\ &\quad + (0.038 \pm 0.080)\ {\rm mag}. \end{aligned} \quad (3)$$

C10 thus find some evidence for a small color term slope in J, a negligible color term in H, and do not attempt to derive any color terms involving K_s.

Following C10, we test for linear color terms between CSP and PAIRITEL filters using 263 2MASS stars with both J- and H-band data. We use the Carpenter (2001) color terms for K_s.[31] We find the following JH linear color term fits using the rms error for the PAIRITEL uncertainties of 2MASS stars (also see

[31] Carpenter (2001) finds these fits for the LCO K_s band using the Persson standard stars: $K_{s_{\rm CSP}} - K_{s_{\rm 2M}} = (-0.015 \pm 0.004) \times (J - K_s)_{\rm CSP} + (0.002 \pm 0.004)$ mag. The Carpenter (2001) color transformations have been updated at http://www.astro.caltech.edu/jmc/2mass/v3/transformations/ as of 2003. Carpenter (2001) find a fairly small color term for K_s (the CSP K_s filter is on the 2.5 m du Pont telescope at LCO).

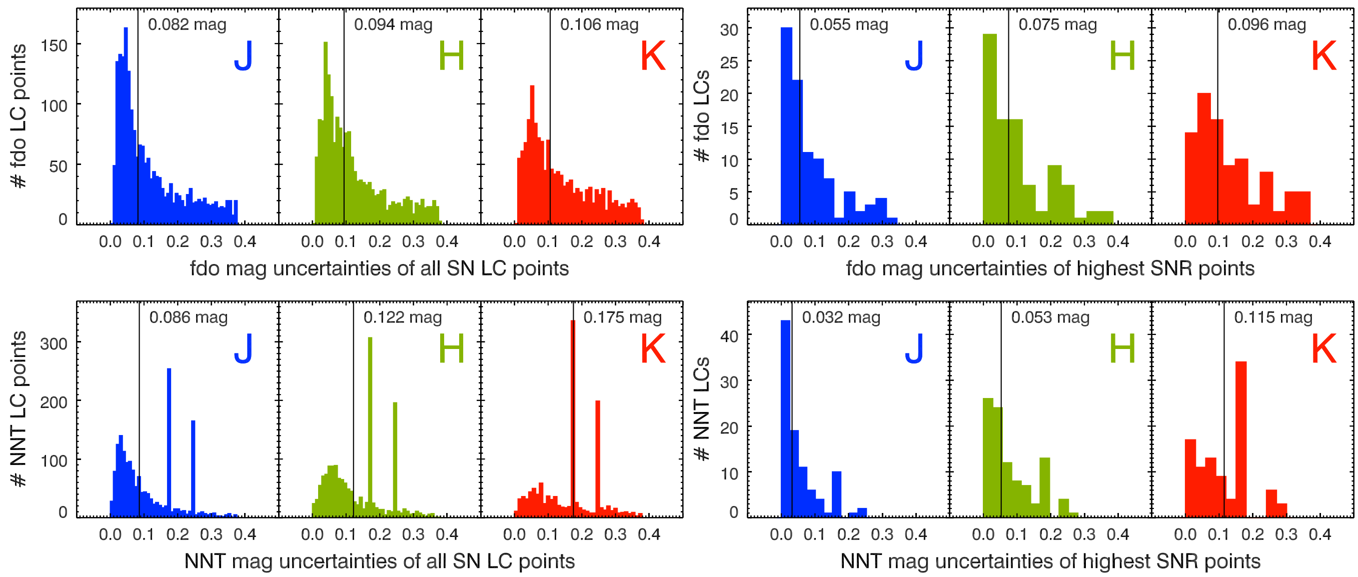

Figure 7. Magnitude uncertainty histograms for (Row 1) forced DoPHOT photometry (fdo) on unsubtracted images and (Row 2) host-galaxy-subtracted photometry (NNT). Median values are indicated with vertical lines and plot annotations. Left columns show errors for all CfAIR2 LC points. Right columns show errors for only the highest-S/N points for each CfAIR2 LC. Spikes at 0.25 and 0.175 mag (lower left figure) and at 0.175 mag (lower right figure) reflect the conservative systematic error floor imposed for cases with $N_T = 1$ or 2 usable subtractions (see Table 6). The highest-S/N LC points have median uncertainties of $\sim$ 0.032, 0.053, and 0.115 mag in JHK_s, respectively (lower right plot). Even in these cases, the systematic error floor skews histograms toward larger median errors; for JHK_s, there are ~10–35 LCs with only $N_T = 2$ usable subtractions, leading to spikes at 0.175 mag. All CfAIR2 NNT LC points have median uncertainties of 0.086, 0.122, and 0.175 mag in JHK_s, respectively (lower left plot). NNT errors are generally comparable to or less than forced DoPHOT errors on unsubtracted images provided $N_T \gtrsim$ 3–4. This again reflects the systematic error floor for $N_T = 1$ or 2. For the highest-S/N points for each LC, the median NNT photometric precision is smaller than forced DoPHOT for J and H, but not in K_s, again as a result of the systematic error floor (see right column figures).

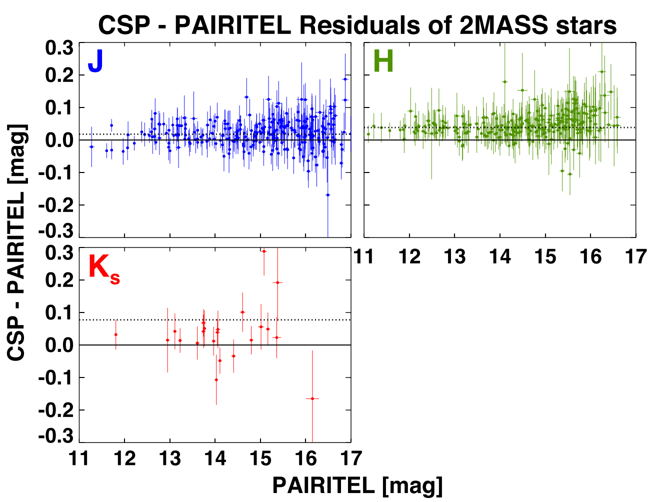

Figure 8. PAIRITEL and CSP JHK_s Offsets. For 19 NIR SN fields, we use 269, 264, and 24 2MASS stars observed by both PAIRITEL and the CSP in JHK_s, respectively, in the color range $0.2 < (J-H)_{\rm CSP} < 0.7$ mag also used by C10. Plots show CSP–PAIRITEL JHK_s magnitude residuals on the y-axis vs. the PAIRITEL star magnitude on the x-axis. Errors on the residuals are the quadrature sum of the quoted CSP errors and the PAIRITEL errors on the weighted mean magnitude of 2MASS stars, given by the rms errors for PAIRITEL (not shown in Table 5; see Section 4.3.1). The weighted mean zero-point offsets (dotted lines) in each panel are the values given in Equation (2).

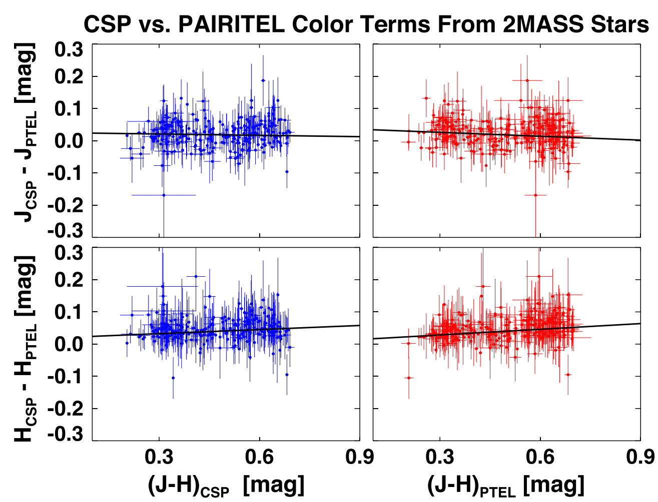

Figure 9. PAIRITEL and CSP $J-H$ Color Terms. Linear fits for JH color terms using 2MASS stars observed by PAIRITEL and CSP, given by Equation (4). Following C10, we include only stars in the color range $0.2 < (J-H)_{\rm CSP} < 0.7$ mag, yielding 263 2MASS stars with $(J-H)_{\rm CSP}$ data (blue, left panels) and 259 stars with $(J - H)_{\rm PTL}$ data (red, right panels). Error bars assume rms errors for PAIRITEL (not shown in Table 5; see Section 4.3.1). Linear fits have χ^2/doF $= \chi^2_\nu < 1$ ($\chi^2_\nu = 0.79$, 0.35, left panels and $\chi^2_\nu = 0.79$, 0.33, right panels, both top to bottom).

Figure 9):

$$\begin{aligned} J_{\rm CSP} - J_{\rm PTL} &= (-0.014 \pm 0.017) \times (J-H)_{\rm CSP} \\ &\quad + (0.025 \pm 0.009)\ {\rm mag}, \\ H_{\rm CSP} - H_{\rm PTL} &= (0.042 \pm 0.022) \times (J-H)_{\rm CSP} \\ &\quad + (0.020 \pm 0.011)\ {\rm mag}. \end{aligned} \quad (4)$$

Linear color term fits yield $\chi^2_\nu < 1$, indicating that while the fits are good, the errors are slightly overestimated by using the rms. For all panels in Figure 9, the probability that a correct model would give the observed χ^2_ν is ~1. JH color term fits from Equation (4) and from C10 in Equation (3) agree in the slopes at 2σ and the intercepts at 1σ. Both fits also yield the same signs for the slopes and indicate at most small JH color terms.

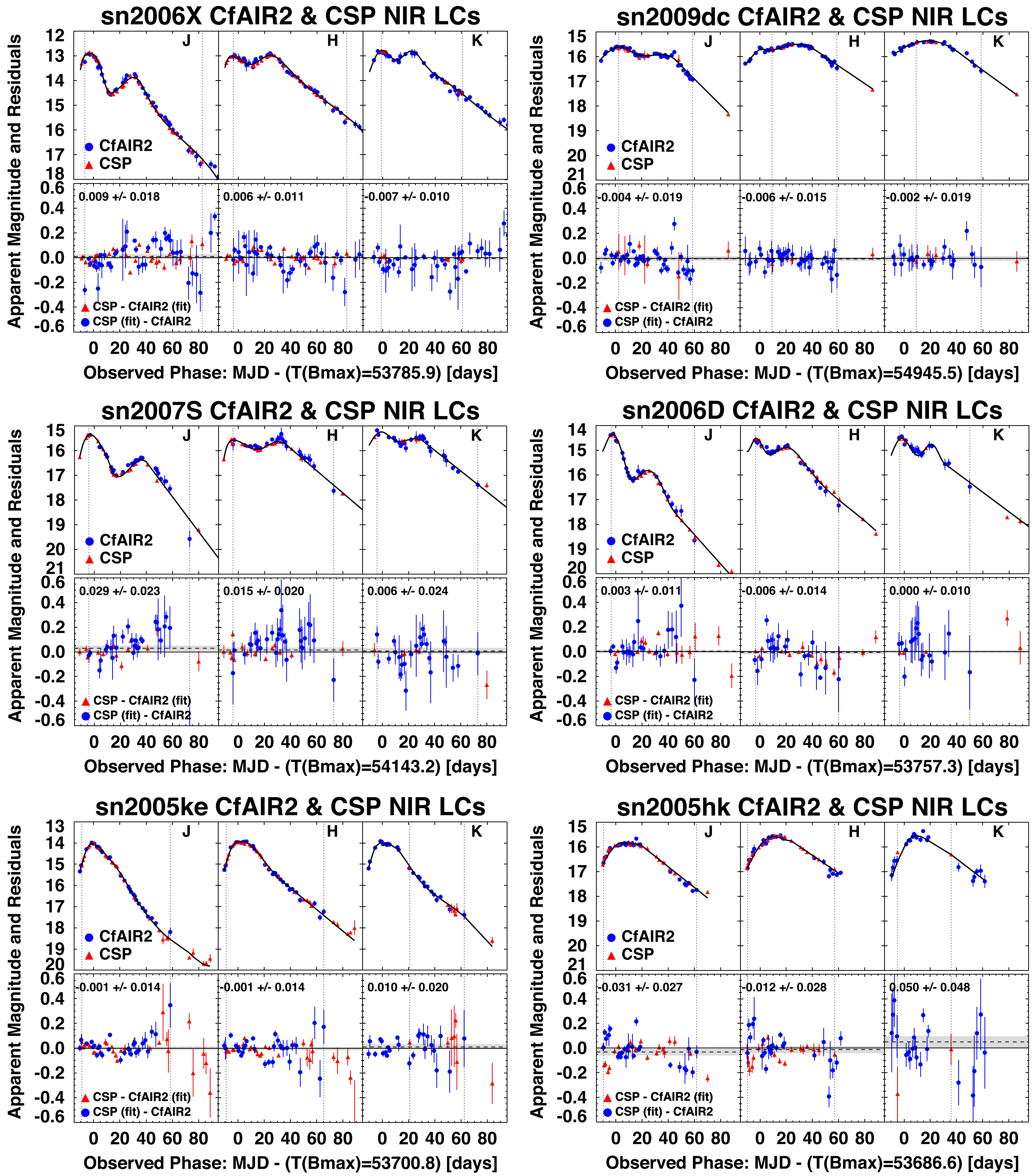

Figure 10. Comparing CfAIR2 to CSP Photometry. Top panels: Plot shows 6 example NIR SN Ia LCs out of the 18 CfAIR2 objects observed by both PAIRITEL and CSP. JHK_s SN Ia LCs are shown from PAIRITEL CfAIR2 galaxy-subtracted photometry (blue circles) and CSP LCs (red triangles) after applying color terms from Equation (4) of this paper (see Section 4.3.3). Vertical dotted lines show regions of temporal overlap for both LCs. The black line is a cubic spline model fit to the joint PAIRITEL+CSP data with a simple linear fit applied $\gtrsim$30–40 days in specific cases. For normal SN Ia, the WV08 mean template LC is used to help fit for missing data (not for Ia-pec or Iax: SN 2009dc, SN 2005ke, SN 2005hk). Bottom panels: CSP–CfAIR2 residuals are computed as either (CSP data minus CfAIR2 joint model fit) or (CSP joint model fit–CfAIR2 data) for each epoch, using the same plot symbols as above for differences computed using CSP or CfAIR2 data. While the CSP (fit)–CfAIR2 residuals (blue circles) are above the zero residual line when the corresponding CfAIR2 data point has a larger magnitude value than the joint model fit in the top row panels, since we are computing CSP–CfAIR2 residuals, the CSP–CfAIR2 (fit) (red triangles) residuals behave in the opposite sense. For example, when the CSP data have a larger magnitude than the joint model fit in the top row panels, the corresponding residual lies *below* the zero residual line. Weighted mean residuals and 1σ uncertainties for CSP–CfAIR2 data in the phase range [−10, 60] days, as listed in Table 7, are also shown in the upper left corner of each panel and indicated by the dashed line and the gray strip, respectively.

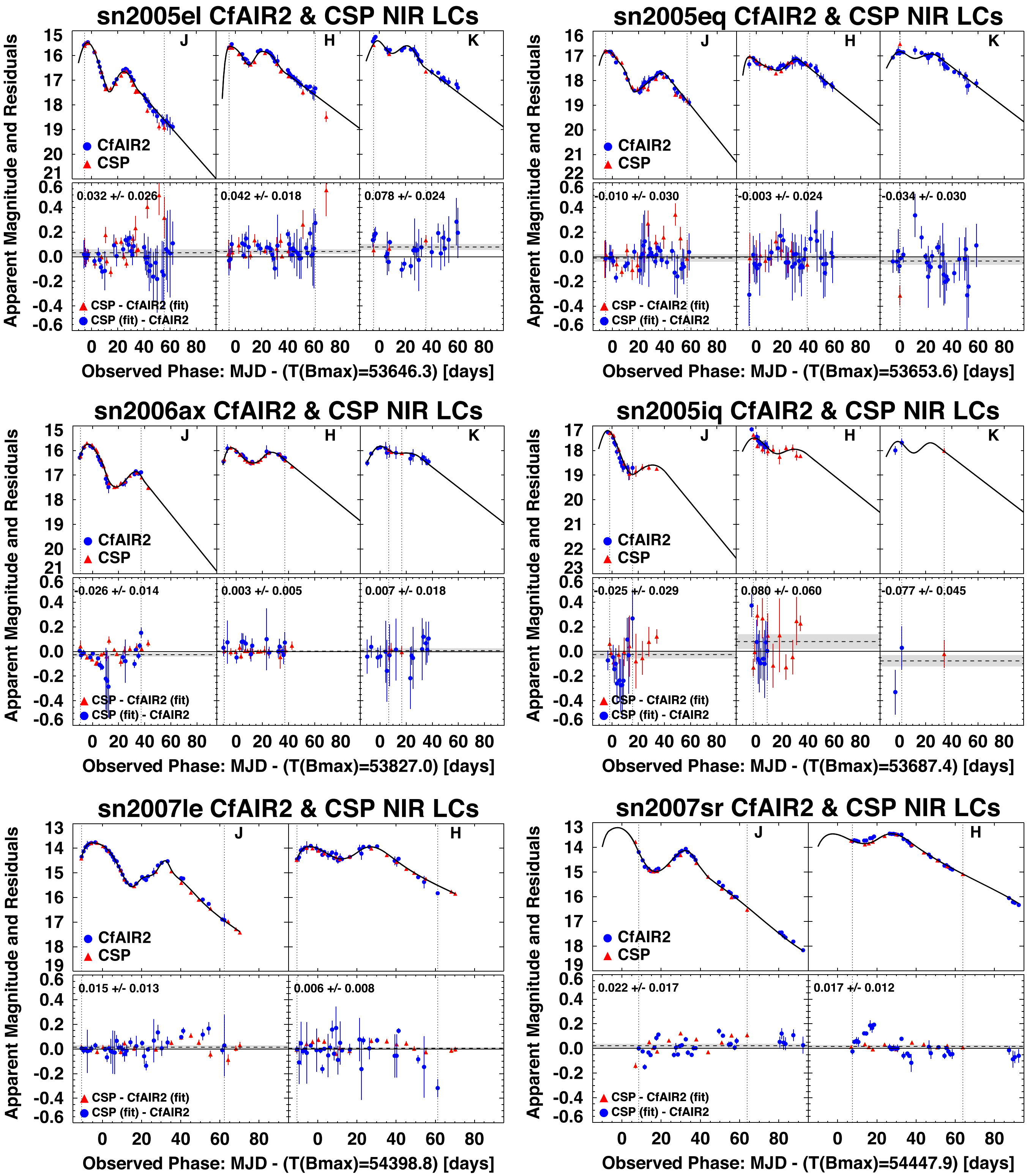

Figure 11. Comparing CfAIR2 to CSP Photometry. Top panels: Plot shows 6 example NIR SN Ia LCs out of the 18 CfAIR2 objects observed by both PAIRITEL and CSP. JHK_s SN Ia LCs are shown from PAIRITEL CfAIR2 galaxy-subtracted photometry (blue circles) and CSP LCs (red triangles) after applying color terms from Equation (4) of this paper (see Section 4.3.3). Vertical dotted lines show regions of temporal overlap for both LCs. The black line is a cubic spline model fit to the joint PAIRITEL+CSP data with a simple linear fit applied $\gtrsim$30–40 days in specific cases. For normal SN Ia, the WV08 mean template LC is used to help fit for missing data. CSP K_s band is missing for some SN Ia (e.g., SN 2007le and SN 2007sr). Bottom panels: CSP–CfAIR2 residuals are computed as either (CSP data minus CfAIR2 joint model fit) or (CSP joint model fit–CfAIR2 data) for each epoch, using the same plot symbols as above for differences computed using CSP or CfAIR2 data. While the CSP (fit)–CfAIR2 residuals (blue circles) are above the zero residual line when the corresponding CfAIR2 data point has a larger magnitude value than the joint model fit in the top row panels, since we are computing CSP–CfAIR2 residuals, the CSP–CfAIR2 (fit) (red triangles) residuals behave in the opposite sense. For example, when the CSP data have a larger magnitude than the joint model fit in the top row panels, the corresponding residual lies *below* the zero residual line. Weighted mean residuals and 1σ uncertainties for CSP–CfAIR2 data in the phase range [−10, 60] days, as listed in Table 7, are also shown in the upper left corner of each panel and indicated by the dashed line and the gray strip, respectively.

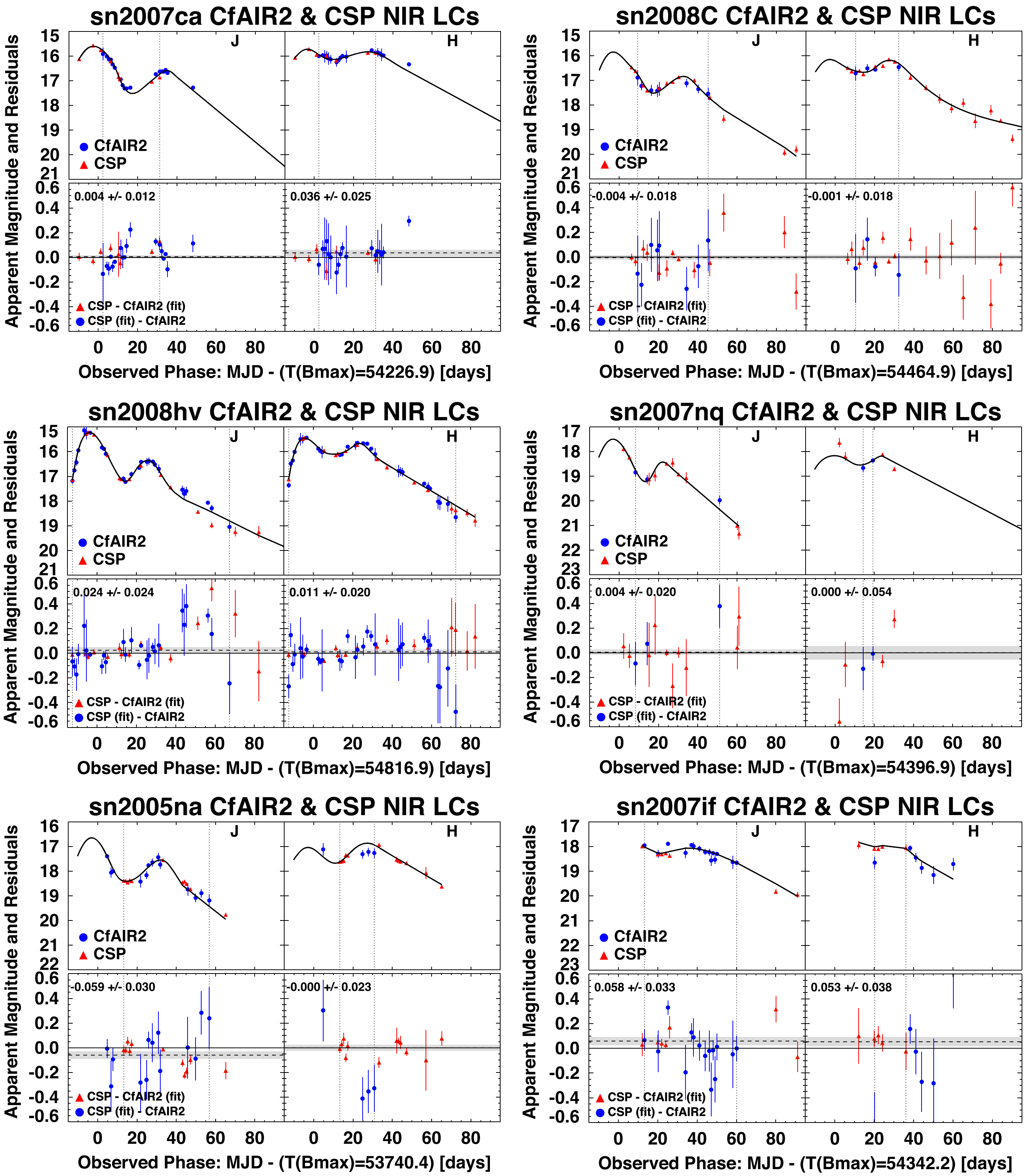

Figure 12. Comparing CfAIR2 to CSP Photometry. Top panels: Plot shows 6 example NIR SN Ia LCs out of the 18 CfAIR2 objects observed by both PAIRITEL and CSP. JHK_s SN Ia LCs are shown from PAIRITEL CfAIR2 galaxy-subtracted photometry (blue circles) and CSP LCs (red triangles) after applying color terms from Equation (4) of this paper (see Section 4.3.3). Vertical dotted lines show regions of temporal overlap for both LCs. The black line is a cubic spline model fit to the joint PAIRITEL+CSP data with a simple linear fit applied $\gtrsim$30–40 days in specific cases. For normal SN Ia, the WV08 mean template LC is used to help fit for missing data. CSP K_s band is missing for all the above SN. Bottom panels: CSP–CfAIR2 residuals are computed as either (CSP data minus CfAIR2 joint model fit) or (CSP joint model fit–CfAIR2 data) for each epoch, using the same plot symbols as above for differences computed using CSP or CfAIR2 data. While the CSP (fit)–CfAIR2 residuals (blue circles) are above the zero residual line when the corresponding CfAIR2 data point has a larger magnitude value than the joint model fit in the top row panels, since we are computing CSP–CfAIR2 residuals, the CSP–CfAIR2 (fit) (red triangles) residuals behave in the opposite sense. For example, when the CSP data have a larger magnitude than the joint model fit in the top row panels, the corresponding residual lies *below* the zero residual line. Weighted mean residuals and 1σ uncertainties for CSP–CfAIR2 data in the phase range [−10, 60] days, as listed in Table 7, are also shown in the upper left corner of each panel and indicated by the dashed line and the gray strip, respectively.

Again, although the C10 fits used ~3–4 times as many 2MASS stars, we consider the color terms from either Equation (3) or (4) to be equally reliable. For SN LCs with sufficient sampling to compute reliable colors, applying either set of color terms produced comparable results, since both color terms are small. In summary, either set of color terms (or no color terms) are reasonable choices to approximately put CSP data on the PAIRITEL/2MASS system. Still, to compare CSP and CfAIR2 data on the same footing, for the analysis in Section 4.4, we apply our own JH color terms from Equation (4) and K_s color terms from Carpenter (2001) as needed.

4.4. Comparing CfAIR2 and CSP LCs

Because CfAIR2 and CSP observations were generally performed at slightly different phases, it is usually not possible to compute direct LC data differences. We thus require a smooth model fit to interpolate from to compute residuals, which we apply to all 18 overlap objects.[32] The purpose of these model fits is not to estimate LC shape parameters, but merely to provide a baseline with which to compute residuals. Figures 10–12 overplot all 18 example CfAIR2 and CSP SN Ia LCs for comparison. Applying either set of color terms from Section 4.3.3 (or no color terms) had a negligible effect on the CSP LCs, model fits, and weighted mean residuals for the CSP-CfAIR2 data in Table 7.

For all CfAIR2 and color-term-corrected CSP LC points at similar phases, the scatter in the residuals arises from both statistical photometric uncertainties and systematic uncertainties as a result of imperfect model fits, which can dominate, especially at late times. For individual SN Ia, we compute the weighted mean of the residuals about the joint model fit in the phase range [−10, 60] days where the model fit is generally valid. To include systematic uncertainty from the joint model fit, we conservatively estimated the 1σ uncertainty on the weighted mean CSP–CfAIR2 residual as the error-weighted standard deviation of the residuals, which we then divided by a factor of 3 to avoid overestimating the uncertainty. We then compute whether the mean CSP–CfAIR2 residuals are consistent with zero to within 1, 2 or 3σ in the selected phase range. We find that nearly all CfAIR2 and color-term-corrected CSP SN Ia LCs (18 JH and 8 K_s LCs) are consistent to within 3σ by this metric.[33] See Figures 10–12 and Table 7.

While this method is useful to compare entire LCs, we note that some CSP and CfAIR2 LCs in specific bands do show significant ~0.1–0.4 mag deviations for individual data points at similar phases or ranges of data points over smaller phase ranges, beyond what can be explained from poor model fits alone. For example, these discrepancies were noted: SN 2005iq, H, <0 days; SN 2005na, H, 20–40 days; SN 2007if, JH, 20–30 days; SN 2008hv, J, >40 days; SN 2006D, H, >40 days; SN 2005el, JH, >40 days; SN 2007sr, H, 10–20 days. Nevertheless, many of these differences come from ~1–2, individual outlier CfAIR2 data points, and most of the LCs show broad agreement by the above metric across a broad range of phases. See Figures 10–12.

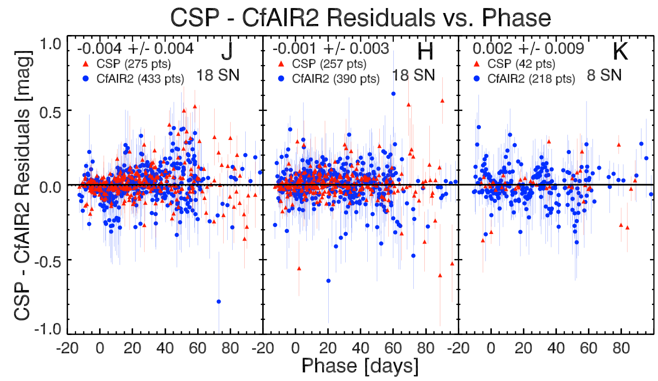

Figure 13. CfAIR2/CSP Aggregated Residuals. Aggregated residuals and errors from LC model fits in Section 4.4, Figures 10–12, for CSP (red filled triangles) and CfAIR2 (blue filled circles) data from [−15,100] days after applying the color terms from Equation (4) to CSP data. Outlier residuals from bad fits were removed with conservative 10σ clipping. There are 18 SN with joint JH data and 8 with K_s data. Aggregated residuals include the following number of data points for CfAIR2: 433, 390, and 218, and CSP: 275, 257, and 42, in JHK_s, respectively. The weighted means of the aggregated CSP–CfAIR2 residuals are -0.004 ± 0.004, -0.001 ± 0.003, and 0.002 ± 0.009 for JHK_s, respectively. Applying the C10 color terms from Equation (3) or applying no color terms had a negligible effect on the results. In all cases, differences between the JHK_s CSP and CfAIR2 global weighted mean residuals have absolute values of only ~0.001–0.004 mag and are consistent with zero to within 1σ, where the 1σ error is given by the standard error on the mean. PAIRITEL CfAIR2 data thus show excellent global agreement with CSP.

We can also test whether CfAIR2 and CSP are consistent for the entire overlap sample, rather than just individual objects. Figure 13 shows aggregated residuals in the phase range [−15,100] days after applying color terms from Equation (4) to the CSP data. Using 433, 390, and 218 CfAIR2 LC points, and 275, 257, and 42 CSP LC points, each in JHK_s, respectively, we find that the global weighted mean of the aggregated residuals is consistent with zero in each case (see Figure 13). Applying color terms from C10 (or no color terms) did not affect the results. We conclude that both for individual LCs and for the global aggregated sample, PAIRITEL CfAIR2 photometry and CSP photometry show satisfactory overall agreement.

5. FINAL CFAIR2 DATA SET

Final, host-galaxy-subtracted JHK_s LCs for 94 spectroscopically normal and peculiar CfAIR2 SN Ia and 4 SN Iax are presented in Figure 14 and Table 8.[34] No K-corrections or Milky Way dust extinction corrections have been applied to the final CfAIR2 LCs (see Section 6). PAIRITEL flux and magnitude measurements and errors are listed in Table 8 (see Section 4.2.2). Figure 15 shows CfAIR2 data for two peculiar SN Ia and one SN Iax with the WV08 mean LC template shown to emphasize how easily these objects can be distinguished from normal SN Ia using NIR LC shape alone. A new mean normal SN Ia NIR LC template using CfAIR2

---

[32] Model fits to joint CfAIR2 +CSP data all use cubic splines, with some LCs using simple linear fits at late epochs $\gtrsim$30 days. All fits are boxcar-smoothed with a 5-day moving window. These steps avoid spline overfitting. All fits to normal SN Ia use the WV08 normal SN Ia template LC to inform the fit for missing data, with data given greater weight than the template to account for intrinsic variation of the NIR LC shapes. Re-fitting the mean template LC using spectroscopically normal CfAIR2 SN Ia yielded very similar results to the WV08 template, so we did not find it necessary to construct a new mean template LC for the purposes of these LC fits. This will be presented elsewhere. Fits to peculiar SN Ia or SN Iax are direct fits to data only.

[33] Except for SN 2005el in K_s, which agrees at 4σ.

[34] Only SN Iax SN 2008A and the SN 2005cf LC from WV08 used forced DoPHOT photometry, without galaxy subtraction.

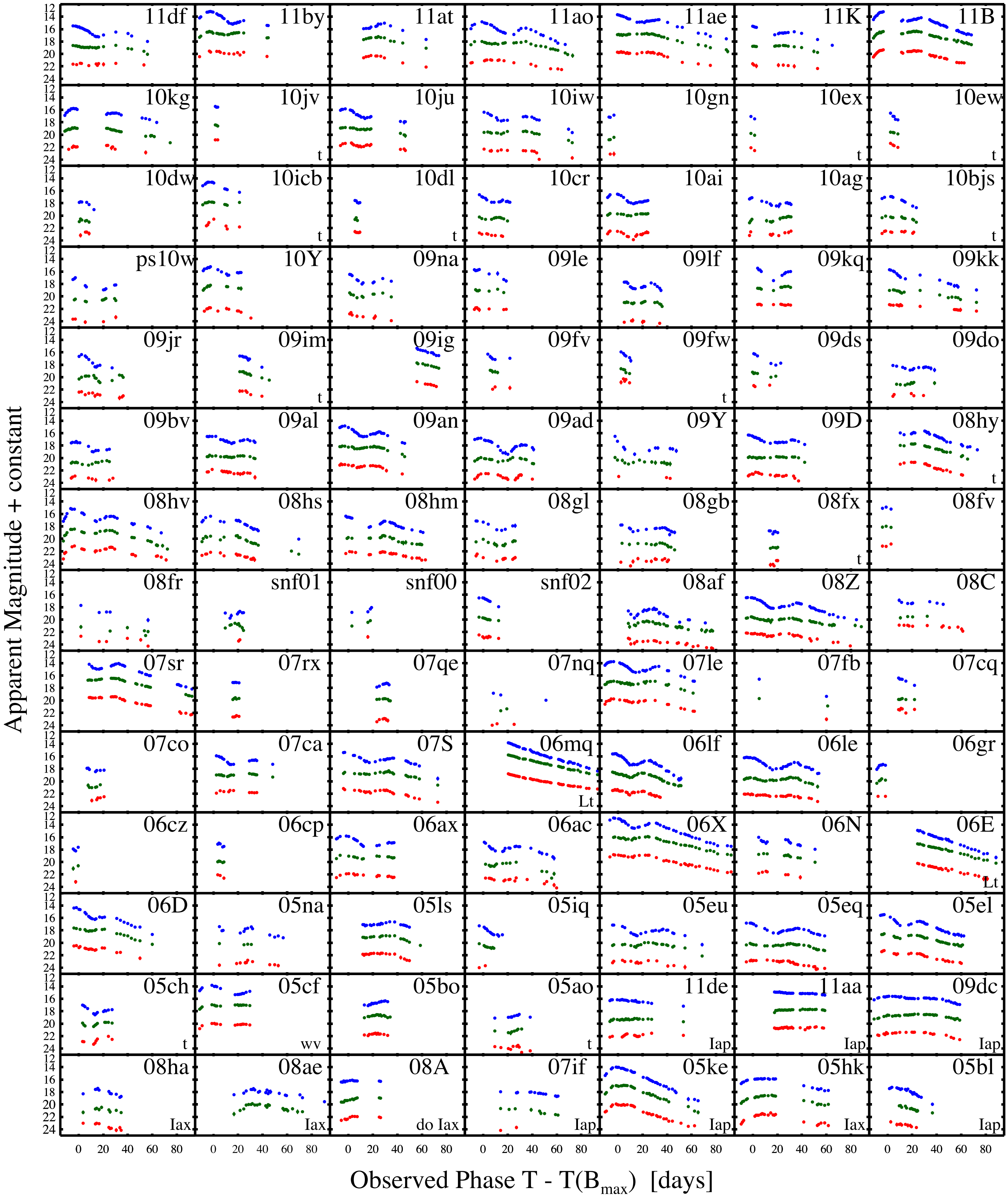

Figure 14. PAIRITEL CfAIR2 NIR LCs: 94 SN Ia and 4 SN Iax LCs in JHK_s. Data points in magnitudes are shown for J (blue), $H + 3$ (green), and $K_s + 6$ (red). Uncertainties are comparable to the sizes of the plot symbols. Plots are for the 88 spectroscopically normal SN Ia *except* for 6 peculiar SN Ia and 4 SN Iax (also see Figure 15) marked in the lower right of each panel with Iap or Iax, which are displayed last starting with SN 2011de. The following notes apply to the lower right corner of some LC plots: *t*: $t_{B\,\mathrm{max}}$ estimated from optical spectra and cross checked with NIR LC features in lieu of early-time optical photometry (see Table 9). Lt: SN 2006E and SN 2006mq were discovered late, so lack precise $t_{B\,\mathrm{max}}$ estimates (see Table 9). Iap: Peculiar objects, which clearly differ from the mean JHK_s LC templates (see Figure 15). Iax: see Foley et al. (2013) for a description of this distinct class of objects. wv: SN 2005cf is included in CfAIR2 but uses the same forced DoPHOT LC as in WV08, without host galaxy subtraction. do: SN 2008A used forced DoPHOT photometry, not the NNT host galaxy subtraction used for all other CfAIR2 LCs except SN 2005cf.

Table 8
PAIRITEL CfAIR2 JHK_s Photometry

SN	Type	Telescope	Band	Date	MJD (days)[a]	f_{25}[b]	$\sigma_{f_{25}}$[c]	JHK_s (mag)[d]	σ_{JHK_s} (mag)[d]
SN 2005ao	Ia	PAIRITEL	J	2005 Mar 22	53451.48	227.592	17.306	19.11	0.08
SN 2005ao	Ia	PAIRITEL	J	2005 Apr 02	53462.51	255.056	21.694	18.98	0.09
SN 2005ao	Ia	PAIRITEL	J	2005 Apr 04	53464.39	263.369	29.603	18.95	0.12
SN 2005ao	Ia	PAIRITEL	J	2005 Apr 05	53465.39	266.528	72.947	18.94	0.30
SN 2005ao	Ia	PAIRITEL	J	2005 Apr 07	53467.39	311.257	40.449	18.77	0.14
SN 2005ao	Ia	PAIRITEL	J	2005 Apr 09	53469.42	341.932	12.230	18.67	0.04
SN 2005ao	Ia	PAIRITEL	J	2005 Apr 10	53470.38	343.194	25.402	18.66	0.08
SN 2005ao	Ia	PAIRITEL	J	2005 Apr 11	53471.38	395.464	65.052	18.51	0.18
SN 2005ao	Ia	PAIRITEL	J	2005 Apr 20	53480.35	259.901	17.128	18.96	0.07
SN 2005ao	Ia	PAIRITEL	H	2005 Mar 22	53451.48	535.150	44.485	18.18	0.09
SN 2005ao	Ia	PAIRITEL	H	2005 Apr 02	53462.51	416.466	50.697	18.45	0.13
SN 2005ao	Ia	PAIRITEL	H	2005 Apr 04	53464.39	393.065	120.604	18.51	0.34
SN 2005ao	Ia	PAIRITEL	H	2005 Apr 05	53465.39	475.528	75.989	18.31	0.18
SN 2005ao	Ia	PAIRITEL	H	2005 Apr 07	53467.39	526.212	113.705	18.20	0.24
SN 2005ao	Ia	PAIRITEL	H	2005 Apr 09	53469.42	596.101	72.917	18.06	0.13
SN 2005ao	Ia	PAIRITEL	H	2005 Apr 10	53470.38	695.897	83.084	17.89	0.13
SN 2005ao	Ia	PAIRITEL	H	2005 Apr 13	53473.36	713.816	114.068	17.87	0.18
SN 2005ao	Ia	PAIRITEL	K_s	2005 Mar 22	53451.48	833.517	126.880	17.70	0.17
SN 2005ao	Ia	PAIRITEL	K_s	2005 Mar 27	53456.43	723.626	127.287	17.85	0.19
SN 2005ao	Ia	PAIRITEL	K_s	2005 Apr 02	53462.51	622.584	126.942	18.01	0.22
SN 2005ao	Ia	PAIRITEL	K_s	2005 Apr 04	53464.39	550.997	88.049	18.15	0.18
SN 2005ao	Ia	PAIRITEL	K_s	2005 Apr 06	53466.39	862.798	125.926	17.66	0.16
SN 2005ao	Ia	PAIRITEL	K_s	2005 Apr 09	53469.42	871.012	138.486	17.65	0.17
SN 2005ao	Ia	PAIRITEL	K_s	2005 Apr 10	53470.38	1004.776	132.201	17.49	0.14
SN 2005ao	Ia	PAIRITEL	K_s	2005 Apr 11	53471.38	776.477	73.523	17.77	0.10
SN 2005ao	Ia	PAIRITEL	K_s	2005 Apr 13	53473.36	354.654	56.674	18.63	0.18
SN 2005ao	Ia	PAIRITEL	K_s	2005 Apr 20	53480.35	446.927	102.060	18.37	0.25

Notes.
[a] Modified Julian Date.
[b] f_{25}: Flux normalized to a magnitude of 25. JHK_s mag $= -2.5\log_{10}(f_{25}) + 25$ mag.
[c] $\sigma_{f_{25}}$: Symmetric 1σ error on f_{25}, computed as the error-weighted standard deviation of the flux measurements for each host galaxy subtraction on a given night, weighted by photometric errors corrected for DoPHOT underestimates. See Table 6 and the Appendix. σ_{JHK_s} mag $= [-2.5\log_{10}(f_{25} - \sigma_{f_{25}}) + 2.5\log_{10}(f_{25} + \sigma_{f_{25}})]/2$.
[d] JHK_s magnitude and 1σ uncertainty.

(This table is available in its entirety in machine-readable form.)

and literature data will be presented elsewhere. Preliminary results show that the mean template using only CfAIR2 data is very similar to the WV08 template. We thus felt the WV08 template LC was sufficient for the purposes of this work, where it was used only to help fit PAIRITEL and CSP LCs for comparing normal SN Ia (Section 4.3) and to provide a visual comparison to peculiar objects (Figure 15).

Table 9 shows fits of the observed JHK_s properties for 88 CfAIR2 spectroscopically normal SN Ia. We determined $t_{B\,\max}$ and the LC shape parameter Δ using MLCS2k2.v007 (Jha et al. 2007) fits to our own CfA optical CCD observations (Hicken 2009; Hicken et al. 2009a, 2009b, 2012, CfA5 in preparation) combined with other optical data from the literature where available (e.g., Ganeshalingam et al. 2010; C10; S11), and approximate $t_{B\,\max}$ estimates from optical spectra in discovery and follow-up notices as needed (see Table 9). Table 9 also lists the CMB frame redshift, $z_{\rm CMB}$, the JHK_s apparent magnitudes at the brightest LC point, and the number of epochs in each LC.

Note that the JHK_s magnitudes listed in Table 9 are *not* necessarily the apparent magnitudes at $t_{B\,\max}$ or the relevant

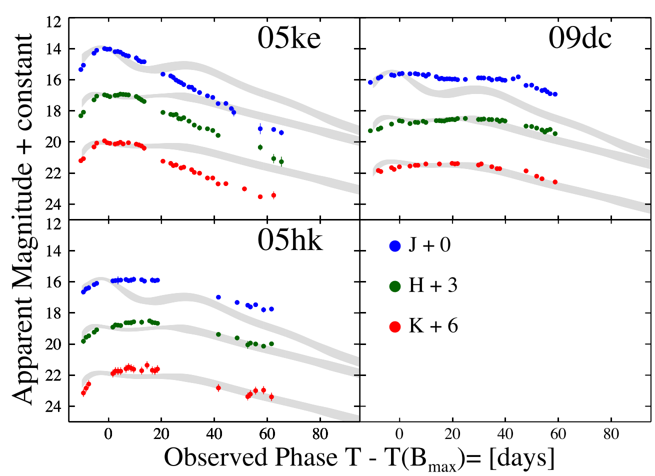

Figure 15. Peculiar SN Ia or SN Iax NIR LC Morphology. CfAIR2 NIR LCs of two peculiar SN Ia (SN 2005ke, SN 2009dc) and one SN Iax (SN 2005hk) with the WV08 mean JHK_s LC templates for spectroscopically normal SN Ia overplotted. Such objects can easily be distinguished from normal SN Ia based on NIR LC morphology alone.

Table 9
JHK_s Light-curve Properties for 88 Spectroscopically Normal PAIRITEL CfAIR2 SN Ia

SN	$t_{B\,\mathrm{max}}$ [a]	σ_{t_B} [a]	Optical Ref.[b]	z_{CMB} [c]	$\sigma_{z\mathrm{CMB}}$ [c]	Δ [d]	σ_Δ [d]	J_p [e]	σ_{J_p} [e]	H_p [e]	σ_{H_p} [e]	K_p [e]	σ_{K_p} [e]	N_J [f]	N_H [f]	N_K [f]
SN 2005ao	53442	2	IAUC 8492	0.03819	0.00099	⋯	⋯	18.51	0.18	17.87	0.18	17.49	0.14	9	8	10
SN 2005bo	53477.99	0.53	C10, G10	0.01502	0.00108	0.146	0.060	16.33	0.04	15.55	0.07	15.53	0.12	15	16	13
SN 2005cf	53533.56	0.11	CfA3, Pa07a, WX09, G10	0.00702	0.00109	−0.108	0.032	13.83	0.04	13.96	0.02	13.97	0.02	17	17	15
SN 2005ch	53536	3	CBET 167	0.02782	0.00103	⋯	⋯	17.02	0.03	16.79	0.08	16.05	0.06	13	11	8
SN 2005el	53646.33	0.17	CfA3, G10	0.01490	0.00100	0.256	0.044	15.46	0.03	15.54	0.05	15.24	0.05	35	34	24
SN 2005eq	53653.73	0.19	CfA3, G10	0.02837	0.00098	⋯	⋯	16.83	0.03	17.08	0.06	16.77	0.18	31	33	29
SN 2005eu	53659.70	0.16	CfA3, G10	0.03334	0.00098	−0.153	0.039	17.14	0.07	16.96	0.10	16.81	0.17	23	23	14
SN 2005iq	53687.45	0.22	CfA3, C10	0.03191	0.00097	0.157	0.049	17.26	0.08	17.14	0.09	17.68	0.18	12	9	2
SN 2005ls	53714	2	CfA3	0.02051	0.00097	⋯	⋯	16.61	0.17	15.85	0.25	15.67	0.25	21	19	19
SN 2005na	53740.57	0.36	CfA3, C10, G10	0.02683	0.00102	⋯	⋯	17.40	0.07	17.12	0.25	16.80	0.26	13	4	10
SN 2006D	53757.30	0.21	CfA3, C10, G10	0.00965	0.00113	⋯	⋯	14.34	0.02	14.61	0.04	14.45	0.06	23	21	17
SN 2006E	53729	10	ATEL 690	0.00364	0.00134	⋯	⋯	14.91	0.01	14.08	0.01	14.22	0.06	30	29	25
SN 2006N	53760.44	0.50	CfA3	0.01427	0.00100	0.468	0.066	16.02	0.09	15.65	0.23	15.49	0.04	14	12	7
SN 2006X	53785.90	0.11	CfA3, C10, WX08, G10	0.00627	0.00121	−0.040	0.030	12.92	0.01	12.90	0.02	12.81	0.03	45	44	37
SN 2006ac	53781.38	0.30	CfA3, G10	0.02412	0.00104	0.230	0.062	16.82	0.12	17.03	0.11	16.55	0.17	22	15	16
SN 2006ax	53826.98	0.14	CfA3, C10	0.01797	0.00107	⋯	⋯	15.82	0.01	15.92	0.17	15.87	0.08	19	15	16
SN 2006cp	53896.76	0.14	CfA3, G10	0.02332	0.00105	−0.166	0.048	16.96	0.08	16.84	0.08	16.06	0.14	5	5	3
SN 2006cz	53903	3	CfA3, CBET 550	0.04253	0.00102	⋯	⋯	17.63	0.06	17.61	0.28	17.17	0.30	4	2	1
SN 2006gr	54012.07	0.15	CfA3, G10	0.03348	0.00097	−0.257	0.032	17.30	0.25	16.61	0.18	16.43	0.16	7	5	2
SN 2006le	54047.36	0.14	CfA3, G10	0.01727	0.00099	−0.219	0.031	16.14	0.02	16.36	0.08	16.04	0.08	39	36	31
SN 2006lf	54044.79	0.13	CfA3, G10	0.01297	0.00098	0.304	0.059	15.57	0.17	15.53	0.06	15.35	0.25	40	41	28
SN 2006mq	54031	10	CBET 724, CBET 731	0.00405	0.00125	⋯	⋯	13.82	0.01	12.78	0.01	12.81	0.00	45	45	45
SN 2007S	54143.25	0.17	CfA3, S11	0.01505	0.00108	−0.303	0.028	15.36	0.02	15.32	0.25	15.18	0.04	29	27	25
SN 2007ca	54226.80	0.15	CfA3, S11, G10	0.01511	0.00107	⋯	⋯	15.92	0.25	15.77	0.07	15.47	0.18	18	18	10
SN 2007co	54264.61	0.24	CfA3, G10	0.02657	0.00099	−0.035	0.046	17.89	0.17	17.57	0.18	16.50	0.22	7	6	5
SN 2007cq	54280.50	0.25	CfA3, G10	0.02503	0.00095	⋯	⋯	16.40	0.04	16.70	0.19	15.29	0.25	6	6	6
SN 2007fb	54287	3	CfA4, CBET 993	0.01681	0.00093	0.348	0.076	16.58	0.25	16.70	0.18	17.03	0.28	2	2	1
SN 2007le	54398.83	0.14	CfA4, S11, G10	0.00551	0.00082	−0.111	0.033	13.76	0.02	13.91	0.01	13.76	0.18	35	31	25
SN 2007nq	54396.94	0.47	CfA4, S11	0.04390	0.00098	0.361	0.063	18.84	0.17	18.36	0.06	17.76	0.19	3	2	3
SN 2007qe	54428.87	0.15	CfA3, G10	0.02286	0.00095	−0.215	0.035	17.22	0.06	16.71	0.05	16.91	0.17	8	8	7
SN 2007rx	54441	3	CfA4, CBET 1157	0.02890	0.00096	−0.249	0.080	17.10	0.07	16.56	0.06	16.45	0.08	5	5	5
SN 2007sr	54447.92	0.51	CfA3, S08, G10	0.00665	0.00122	−0.083	0.040	14.06	0.02	13.44	0.03	13.39	0.03	30	32	32
SN 2008C	54464.79	0.59	CfA4, S11, G10	0.01708	0.00103	−0.038	0.046	16.89	0.31	16.46	0.17	14.89	0.25	8	4	12
SN 2008Z	54514.66	0.19	CfA4, G10	0.02183	0.00104	−0.176	0.038	16.45	0.03	16.55	0.18	16.16	0.10	45	44	32
SN 2008af	54500.47	1.02	CfA3	0.03411	0.00102	0.275	0.092	18.16	0.25	17.24	0.25	17.01	0.25	23	31	21
SNf20080514-002	54611.55	0.42	G10	0.02306	0.00104	0.275	0.068	16.51	0.11	16.61	0.12	16.47	0.18	9	9	8
SNf20080522-000	54621.28	0.48	CfA4	0.04817	0.00102	−0.137	0.075	18.06	0.17	17.17	0.25	16.79	0.30	4	3	1
SNf20080522-011	54617	2	CfA4	0.04026	0.00101	−0.141	0.053	18.68	0.08	17.59	0.12	17.24	0.18	8	9	2
SN 2008fr	54732	2	CfA4	0.04793	0.00098	−0.126	0.046	17.72	0.05	18.18	0.32	16.68	0.17	5	6	6
SN 2008fv	54749.80	0.20	CfA5, Bi12	0.00954	0.00102	⋯	⋯	14.91	0.25	14.98	0.25	14.84	0.25	3	3	3
SN 2008fx	54729	3	CBET 1525	0.05814	0.00099	⋯	⋯	18.72	0.12	18.37	0.10	17.50	0.18	6	5	5
SN 2008gb	54745.42	1.09	CfA4	0.03643	0.00098	−0.093	0.073	17.78	0.21	17.67	0.25	17.19	0.28	19	14	12
SN 2008gl	54768.13	0.27	CfA4	0.03297	0.00097	0.311	0.081	17.14	0.17	17.08	0.18	16.45	0.17	9	12	10
SN 2008hm	54804.33	0.41	CfA4	0.01918	0.00098	−0.122	0.052	16.36	0.03	16.48	0.21	16.06	0.18	26	22	23
SN 2008hs	54812.64	0.15	CfA4	0.01664	0.00096	0.927	0.070	16.37	0.07	16.49	0.05	16.17	0.12	20	21	17
SN 2008hv	54816.91	0.11	CfA4, S11	0.01359	0.00108	0.376	0.051	15.14	0.25	15.44	0.04	15.15	0.08	26	29	24
SN 2008hy	54803	5	AAVSO 392, CBET 1610	0.00821	0.00097	⋯	⋯	15.67	0.03	14.72	0.02	14.68	0.06	27	23	20
SN 2009D	54842	2	CfA4, CBET 1647	0.02467	0.00099	−0.106	0.058	16.31	0.01	16.78	0.25	16.29	0.25	27	24	19
SN 2009Y	54875.89	0.48	CfA4	0.01007	0.00108	−0.116	0.051	16.52	0.22	16.93	0.25	16.98	0.25	11	15	3
SN 2009ad	54886.05	0.24	CfA4	0.02834	0.00100	⋯	⋯	16.82	0.08	16.92	0.10	16.51	0.14	27	20	19
SN 2009al	54896.41	0.31	CfA4	0.02329	0.00105	⋯	⋯	16.52	0.03	16.55	0.04	15.84	0.14	22	22	19
SN 2009an	54898.21	0.24	CfA4	0.00954	0.00104	0.350	0.079	14.85	0.06	15.08	0.04	14.97	0.03	31	29	22
SN 2009bv	54926.33	0.38	CfA4	0.03749	0.00102	−0.180	0.056	17.34	0.07	17.43	0.09	16.91	0.20	13	13	8
SN 2009do	54945	2	CfA4, CBET 1778	0.04034	0.00102	0.079	0.072	18.12	0.13	17.84	0.18	16.64	0.25	14	9	5
SN 2009ds	54960.50	0.38	CfA4	0.02045	0.00106	−0.120	0.056	16.22	0.23	16.20	0.17	15.29	0.25	6	6	3
SN 2009fw	54993	3	CBET 1849	0.02739	0.00097	⋯	⋯	15.94	0.09	15.65	0.25	14.27	0.18	6	5	5
SN 2009fv	54998	3	CfA4, CBET 1846	0.02937	0.00100	0.238	0.188	16.30	0.16	15.90	0.25	15.57	0.26	6	5	3

Table 9
(Continued)

SN	$t_{B\,\max}$[a]	σ_{t_B}[a]	Optical Ref.[b]	$z_{\rm CMB}$[c]	$\sigma_{z_{\rm CMB}}$[c]	Δ[d]	σ_{Δ}[d]	J_p[e]	σ_{J_p}[e]	H_p[e]	σ_{H_p}[e]	K_p[e]	σ_{K_p}[e]	N_J[f]	N_H[f]	N_K[f]
SN 2009ig	55079.43	0.25	CfA4	0.00801	0.00091	−0.238	0.038	15.34	0.18	14.70	0.17	14.72	0.25	11	9	7
SN 2009im	55074	3	CBET 1934	0.01256	0.00096	…	…	16.60	0.07	16.11	0.03	16.21	0.02	9	11	6
SN 2009jr	55119.83	0.49	CfA4	0.01562	0.00094	−0.167	0.058	16.37	0.17	16.66	0.18	16.34	0.25	11	14	11
SN 2009kk	55125.83	0.73	CfA4	0.01244	0.00097	0.237	0.069	15.72	0.05	15.96	0.06	15.33	0.18	17	17	16
SN 2009kq	55154.61	0.35	CfA4	0.01236	0.00107	−0.030	0.052	15.47	0.18	15.38	0.04	15.27	0.17	10	11	11
SN 2009le	55165.41	0.23	CfA4	0.01704	0.00096	−0.096	0.106	15.68	0.06	15.85	0.17	15.81	0.18	9	7	8
SN 2009lf	55148	2	CfA4, CBET 2025	0.04409	0.00098	0.338	0.085	17.70	0.08	17.81	0.18	17.86	0.36	18	16	7
SN 2009na	55201.31	0.28	CfA4	0.02202	0.00105	0.052	0.060	16.47	0.25	16.44	0.18	16.61	0.17	11	10	8
SN 2010Y	55247.76	0.14	CfA4	0.01126	0.00103	0.826	0.063	15.23	0.02	15.20	0.18	15.82	0.23	15	10	12
PS1-10w	55248.01	0.11	R14	0.03176	0.00102	…	…	17.00	0.06	17.34	0.17	17.35	0.34	10	10	5
PTF10bjs	55256	3	CfA4, ATEL 2453	0.03055	0.00102	…	…	16.95	0.06	17.09	0.07	16.48	0.17	11	12	10
SN 2010ag	55270.23	0.63	CfA4	0.03376	0.00100	−0.249	0.051	17.13	0.01	17.14	0.26	16.50	0.25	15	15	9
SN 2010ai	55276.84	0.13	CfA4	0.01927	0.00105	0.358	0.074	16.56	0.04	16.67	0.11	16.49	0.10	22	17	17
SN 2010cr	55315	3	CfA4, ATEL 2580	0.02253	0.00104	…	…	16.65	0.01	17.24	0.17	16.80	0.17	15	12	8
SN 2010dl	55341	3	CBET 2298	0.02892	0.00096	…	…	17.58	0.11	17.35	0.18	16.59	0.28	5	3	5
PTF10icb	55360	3	Pa11	0.00905	0.00105	…	…	14.63	0.02	14.80	0.17	14.58	0.25	12	12	7
SN 2010dw	55357.75	0.65	CfA4	0.03870	0.00102	−0.146	0.088	17.78	0.05	17.55	0.25	16.66	0.25	6	6	4
SN 2010ew	55379	3	CBET 2356	0.02504	0.00098	…	…	16.53	0.25	16.59	0.25	15.39	0.25	5	4	4
SN 2010ex	55386	3	CBET 2353	0.02164	0.00095	…	…	17.06	0.11	16.79	0.23	16.10	0.17	2	2	2
SN 2010gn	55399	3	CfA5, CBET 2386	0.03638	0.00100	0.023	0.099	16.85	0.18	17.42	0.23	17.09	0.37	3	3	2
SN 2010iw	55492	6	CfA5, CBET 2511	0.02230	0.00104	−0.169	0.056	16.38	0.05	16.41	0.10	16.31	0.17	18	18	13
SN 2010ju	55523.80	0.44	CfA5	0.01535	0.00101	0.054	0.110	15.83	0.02	15.84	0.06	15.32	0.18	21	20	19
SN 2010jv	55516	3	CBET 2550	0.01395	0.00104	…	…	15.44	0.05	15.42	0.10	14.82	0.17	3	3	2
SN 2010kg	55543.48	0.13	CfA5	0.01644	0.00099	0.281	0.069	15.76	0.07	15.86	0.11	15.71	0.17	25	27	12
SN 2011B	55582.92	0.13	CfA5	0.00474	0.00101	0.142	0.054	13.21	0.17	13.33	0.18	13.34	0.18	46	43	37
SN 2011K	55578	3	CfA5, CBET 2636	0.01438	0.00099	−0.138	0.076	15.54	0.01	15.63	0.09	15.59	0.28	16	16	8
SN 2011ae	55619	3	CfA5	0.00724	0.00120	−0.235	0.063	13.69	0.02	13.70	0.03	13.65	0.25	32	32	26
SN 2011ao	55638.26	0.15	CfA5	0.01162	0.00109	−0.157	0.037	14.83	0.03	14.99	0.03	14.95	0.08	28	29	16
SN 2011at	55635	5	CfA5, CBET 2676	0.00787	0.00116	0.321	0.398	15.04	0.02	14.21	0.17	14.25	0.04	13	14	10
SN 2011by	55690.60	0.15	CfA5	0.00341	0.00120	−0.007	0.046	13.17	0.14	13.37	0.03	13.55	0.18	28	27	13
SN 2011df	55716.08	0.41	CfA5	0.01403	0.00096	−0.157	0.070	15.49	0.03	15.62	0.06	15.50	0.17	24	25	11

Notes.
[a] MJD of $t_{B\,\max}$ and error from MLCS2k2.v007 (Jha et al. 2007) fits to B-band LCs from the CfA or the literature, where available. $t_{B\,\max}$ fits from the literature are used for SN 2008fv (Biscardi et al. 2012), and PS1-10w (Rest et al. 2014). For objects with no optical data or bad MLCS fits with reduced $\chi^2 > 3$, $t_{B\,\max}$ is estimated from any or all of: the MJD of the brightest point (rounded to the nearest day), optical spectra in listed CBET/IAUC/ATEL notices, and cross-checked with fitted phases of NIR LC features, where possible (see F12). This applies to all SN in Table 9 with $t_{B\,\max}$ and error rounded to the nearest day, with most assuming a $\pm$2–3 day uncertainty. Of these we observed SN 2009fw, SN 2010ew, SN 2010ex, and SN 2010jv at the CfA but do not have successfully reduced optical LCs for these objects, which are marked CfA? and may or may not be included in CfA5. Two objects, SN 2006E and SN 2006mq, were discovered several weeks after maximum and have only late-time optical data and only rough $t_{B\,\max}$ estimates from optical spectra (these assume a $\pm$10 day uncertainty). Other objects with $t_{B\,\max}$ from early optical data but with only late-time NIR data where the first PAIRITEL observation is at a phase $\gtrsim$20 days after $t_{B\,\max}$ include SN 2007qe, SN 2009ig, and SN 2009im.
[b] Optical LC References: CfA5: in preparation, CfA4: Hicken et al. (2012), CfA3: Hicken et al. (2009b), CfA2: Jha et al. (2006b), CfA1: Riess et al. (1999), F09: Foley et al. (2009), R14: Rest et al. 2014, Br12: Bryngelson (2012), Bi12: Biscardi et al. (2012), S11: Stritzinger et al. (2011), Pa11: Parrent et al. (2011), C10: Contreras et al. (2010), G10: Ganeshalingam et al. (2010), WX09: Wang et al. (2009), WX08: Wang et al. (2008), S08: Schweizer et al. (2008).
[c] Redshift $z_{\rm CMB}$ and error converted to CMB frame with apex vectors from Fixsen et al. (1996) (see NED: http://ned.ipac.caltech.edu/help/velc_help.html). Redshifts have not been corrected with any galactic flow models. Heliocentric redshifts (and references) and galactic coordinates are in Tables 1 and 2.
[d] Δ parameter from MLCS2k2.v007 (Jha et al. 2007) fits to optical data from the CfA and/or the literature, where available. Only fits with reduced $\chi^2 < 3$ are included. The following objects were not run through MLCS2k2: PS1-10w (PanSTARRS1: $t_{B\,\max}$ from SALT fit in Rest et al. 2014), SN 2008fv ($t_{B\,\max}$ in Biscardi et al. 2012). PTF10icb (Parrent et al. 2011, PTF) has unpublished optical data; PTF10bjs (PTF) has unpublished data and is in CfA4, but only in the r' i' natural system and not standard system magnitudes (Hicken et al. 2009b); SN 2006E (Bryngelson 2012) and SN 2006mq (CfA3) have only late-time optical data.
[e] Magnitudes and 1σ uncertainties in JHK_s LCs at the brightest LC point (this is not necessarily the JHK_s magnitude at the first NIR maximum or at $t_{B\,\max}$).
[f] Number of epochs with S/N > 3 in the JHK_s light curves, respectively.

(This table is available in machine-readable form.)

NIR first peaks, but simply the apparent magnitude of the brightest observed data point, which is very sensitive to data coverage. Also note that the $z_{\rm CMB}$ values in Table 9 have *not* been corrected for any local flow models, which would provide more accurate redshift estimates for objects with $z_{\rm CMB} \lesssim 0.01$ ($\lesssim$3000 km s^{-1}). The apparent magnitudes and redshifts in Table 9 should thus not be naively used to estimate galaxy distances or naively combined with high-redshift data to estimate cosmological parameters.

6. DISCUSSION

The 94 CfAIR2 NIR SN Ia and 4 SN Iax LCs obtained in the northern hemisphere with PAIRITEL are matched only by the comparable, excellent quality, southern hemisphere CSP data set, which includes 72 SN Ia LCs (and 1 SN Iax) with at least one band of published $YJHK_s$ data (see Table 10). The CfAIR2 and CSP data sets are quite complementary, observing mostly different objects with varying observation frequencies in individual NIR bandpasses (see Section 4.3). CfAIR2 includes more than twice as many *JH* observations and more than 10 times as many K_s observations as CSP. By contrast, the CSP *Y*-band observations form a unique data set, since no CfA telescopes at FLWO currently have *Y*-band filters (see Table 10).

While CfAIR2 presents more total NIR SN Ia and SN Iax LCs than the CSP (98 vs. 73) and more unique LCs (78 vs. 73) and includes ~3–4 times the number of individual NIR observations, CSP photometric uncertainties are typically ~2–3 times smaller than for CfAIR2 (see Table 10), as a result of key differences between the NIR capabilities at CfA and CSP observing sites (see Table 2.1 of F12). These include better seeing at LCO versus FLWO, a newer, higher-resolution camera on the Swope 1.0 m telescope compared to the 2MASS south camera on the PAIRITEL-1.3 m telescope, and CSP host galaxy template images sometimes taken with the 2.5 m du Pont telescope compared to CfAIR2 template images taken with the 1.3 m PAIRITEL using an undersampled camera. Overall, the CSP JHK_s photometric precision for observations of the *same objects* at the brightest LC point is generally a factor of ~2–3 better than PAIRITEL, with median JHK_s uncertainties of ~0.01–0.02 mag for CSP and ~0.02–0.05 mag for PAIRITEL (see Table 10). More specifically, while CSP has fewer K_s-band measurements, the peak photometric precision is ~3 times better than PAIRITEL mainly because the CSP K_s filter is on the du Pont 2.5 m telescope, as compared to the PAIRITEL 1.3 m. What the CSP lacks in quantity compared to CfAIR2, it makes up for in quality.

However, unlike the CSP NIR data, since PAIRITEL photometry is *already on* the standard 2MASS JHK_s system, no zero-point offsets or color term corrections (e.g., Carpenter 2001; Leggett et al. 2006) or *S*-corrections based on highly uncertain NIR SN Ia SEDs (e.g., Stritzinger et al. 2002) are needed to transform CfAIR2 data to the 2MASS passbands. Avoiding additional systematic uncertainty from *S*-corrections is a significant advantage for PAIRITEL CfAIR2 data, since the published spectral sample of only 75 NIR spectra of 33 SN Ia is still quite limited (Hsiao et al. 2007; Marion et al. 2009; Boldt et al. 2014). This advantage also applies to future cosmological uses of PAIRITEL data that would employ state-of-the-art NIR *K*-corrections to transform LCs to the rest-frame 2MASS filter system as the current world NIR spectral sample is increased. Even for relatively nearby $z \sim 0.08$ objects, NIR *K*-corrections in $YJHK_s$ currently contribute uncertainties of ~0.04–0.10 mag to distance estimates (Boldt et al. 2014). Since NIR K-corrections at $z \sim 0.08$ can themselves have values ranging from ~−0.8 to ~0.4 mag, depending on the filter and phase, they can yield significant systematic distance errors if ignored (Boldt et al. 2014).

7. CONCLUSIONS

This work presents the CfAIR2 data set, including 94 NIR JHK_s-band SN Ia and 4 SN Iax LCs observed from 2005 to 2011 with PAIRITEL. The 4637 individual CfAIR2 data points represent the largest homogeneously observed and reduced set of NIR SN Ia and SN Iax observations to date, nearly doubling the number of individual JHK_s photometric observations from the CSP, surpassing the number of unique CSP objects, and increasing the total number of spectroscopically normal SN Ia with published NIR LCs in the literature by ~65%.[35] CfAIR2 presents revised photometry for 20 out of 21 WV08 objects (and SN 2008 ha from Foley et al. 2009) with more accurate flux measurements and increased agreement for the subset of CfAIR2 objects also observed by the CSP, as a result of greatly improved data reduction and photometry pipelines, applied nearly homogeneously to all CfAIR2 SN.[36]

Previous studies have presented evidence that SN Ia are more standard in NIR luminosity than at optical wavelengths, less sensitive to dimming by host galaxy dust, and crucial to reducing systematic galaxy distance errors as a result of the degeneracy between intrinsic SN color variation and reddening of light by dust, the most dominant source of systematic error in SN Ia cosmology (K04a; WV08; M09; F10; Burns et al. 2011, 2014; M11; K12). Combining PAIRITEL WV08 SN Ia data with optical and NIR data from the literature has already demonstrated that including NIR data helps to break the degeneracy between reddening and intrinsic color, making distance estimates less sensitive to model assumptions of individual LC fitters (M11; Mandel et al. 2014). CfAIR2 photometry will allow the community to further test these conclusions.

The addition of CfAIR2 to the literature presents clear new opportunities. A next step for the community is to combine CfAIR2, CSP, and other NIR and optical low-redshift SN Ia LC databases together using *S*-corrections, or color terms like those derived in this paper, to transform all the LCs to a common filter system. These optical and NIR data can be used to compute optical–NIR colors, derive dust and distance estimates, and construct optical and NIR Hubble diagrams for the nearby universe that are more accurate and precise than studies with optical data alone (e.g., M11). Empirical LC fitting and SN Ia inference methods that handle both optical and NIR data (e.g., `BayeSN`: M09; M11; and `SNooPy`: Burns et al. 2011) can be extended to utilize low- and high-*z* SN Ia samples to obtain cosmological inferences and dark energy constraints that take full advantage of CfAIR2, CSP, and other benchmark NIR data sets.

Increasingly large, homogeneous data sets like CfAIR2 raise hopes that SN Ia, especially in the rest-frame *YH* bands, can be

[35] Including revised photometry for 12 PAIRITEL objects with no CSP or other NIR data.

[36] With the exception of SN 2005cf and SN 2008A (see Sections 3 and 4). SN of other types were also reduced using the same mosaicking and photometry pipelines as the CfAIR2 data set and are presented elsewhere (e.g., Bianco et al. 2014).

Table 10
PAIRITEL and CSP NIR Data Census

Project	SN[a]	NIR[b]	Y^{b}	J^{b}	H^{b}	K_s[b]	σ (mag)[c]
CfAIR2	98	4637	0	1733	1636	1268	0.02–0.05
CSP	73	2434	829	776	705	124	0.01–0.03

Notes.
[a] Number of SN Ia and SN Iax with NIR *YJH* or K_s observations in CfAIR2 (this paper) or CSP (C10; S11; Phillips et al. 2007; Schweizer et al. 2008; Stritzinger et al. 2010; Taubenberger et al. 2011).
[b] Number of epochs of photometry.
[c] Median magnitude uncertainties for CfAIR2 and CSP for same objects at the brightest LC pt.

developed into the most precise and accurate of cosmological distance probes. This hope is further bolstered by complementary progress modeling SN Ia NIR LCs theoretically (e.g., Kasen 2006; Jack et al. 2012) and empirically (M09; M11; Burns et al. 2011). Combining future $IJHYK_s$ data with $\gtrsim$200 NIR SN Ia LCs from CfAIR2, the CSP, and the literature will provide a growing low-z training set to study the intrinsic NIR properties of nearby SN Ia. These NIR data can better constrain the parent populations of host galaxy dust and extinction, elucidating the properties of dust in external galaxies, and allowing researchers to disentangle SN Ia reddening from dust and intrinsic color variation (M11).

CfAIR2 data should be further useful for a number of cosmological and other applications. Improved NIR distance measurements could also allow mapping of the local velocity flow independent of cosmic expansion to understand how peculiar velocities in the nearby universe affect cosmological inferences from SN Ia data (Davis et al. 2011; Turnbull et al. 2011). NIR data should also provide the best SN Ia set with which to augment existing optical measurements of the Hubble constant (e.g., Riess et al. 2011). See Cartier et al. (2014) for a specific use of NIR SN Ia data to measure H_0. Future work can compare NIR LC features and host galaxy properties, which have been shown to correlate with Hubble diagram residuals for optical SN Ia (Kelly et al. 2010). Adding NIR spectroscopy to optical and infrared photometry can also help test physical models of exploding white dwarf stars (e.g., Kasen 2006; Jack et al. 2012) and investigate NIR spectral features that correlate with SN Ia luminosity, helping to achieve improved SN Ia distance estimates, similar to what has already been demonstrated with optical spectra (Bailey et al. 2009; Blondin et al. 2011; Mandel et al. 2014).

Our work emphasizing the intrinsically standard and relatively dust-insensitive nature of NIR SN Ia has highlighted the rest-frame NIR as a promising wavelength range for future space-based cosmological studies of SN Ia and dark energy, where reducing systematic uncertainties from dust extinction and intrinsic color variation become more important than simply increasing the statistical sample size (e.g., Beaulieu et al. 2010; Gehrels 2010; Astier et al. 2011). Although ground-based NIR data can be obtained for low-redshift objects, limited atmospheric transmission windows require that rest-frame NIR observations of high-z SN Ia be done from space. Currently, rest-frame SN Ia Hubble diagrams of high-z SN Ia have yet to be constructed beyond the *I* band (Freedman 2005; Nobili et al. 2005; Freedman et al. 2009), with limited studies of SN Ia and their host galaxies conducted in the mid-infrared with *Spitzer* (Chary et al. 2005; Gerardy et al. 2007). Our nearby NIR observations at the CfA with PAIRITEL have been recently augmented by RAISIN: Tracers of cosmic expansion with SN IA in the IR, an ongoing *HST* program (begun in Cycle 20) to observe ~25 SN Ia at $z \sim 0.35$ in the rest-frame NIR with WFC3/IR.

Along with current and future NIR data, CfAIR2 will provide a crucial low-z anchor for future space missions capable of high-z SN Ia cosmology in the NIR, including the *Wide-field Infrared Survey Telescope* (a candidate for JDEM, the NASA/DOE Joint Dark Energy Mission; Gehrels 2010), the European Space Agency's *EUCLID* mission (Beaulieu et al. 2010), and the NASA *James Webb Space Telescope* (Clampin 2011). To fully utilize the standard nature of rest-frame SN Ia in the NIR and ensure the most precise and accurate extragalactic distances, the astronomical community should strongly consider space-based detectors with rest-frame NIR capabilities toward as long a wavelength as possible.

Until the launch of next-generation NIR space instruments, continuing to observe SN Ia in the NIR from the ground with observatories like PAIRITEL and from space with *HST* programs like RAISIN is the best way to reduce the most troubling fundamental uncertainties in SN Ia cosmology as a result of dust extinction and intrinsic color variation. Ultimately, the CfAIR2 sample of nearby, low-redshift, NIR SN Ia will help lay the groundwork for next-generation ground-based cosmology projects and space missions that observe very distant SN Ia at optical and NIR wavelengths to provide increasingly precise and accurate constraints on dark energy and its potential time variation over cosmic history. NIR SN Ia observations thus promise to play a critical role in elucidating the nature of one of the most mysterious discoveries in modern astrophysics and cosmology.

The Peters Automated Infrared Imaging TElescope (PAIRITEL) is operated by the Smithsonian Astrophysical Observatory (SAO) and was enabled by a grant from the Harvard University Milton Fund, the camera loan from the University of Virginia, and continued support of the SAO and UC Berkeley. Partial support for PAIRITEL operations and this work comes from National Aeronautics and Space Administration (NASA) *Swift* Guest Investigator grant NNG06GH50G ("PAIRITEL: Infrared Follow-up for Swift Transients"). PAIRITEL support and processing are conducted under the auspices of a DOE SciDAC grant (DE-FC02-06ER41453), which provides support to J.S.B.'s group. J.S.B. thanks the Sloan Research Fellowship for partial support, as well as NASA grant NNX13AC58G. We gratefully made use of the NASA/IPAC Extragalactic Database (NED). The NASA/IPAC Extragalactic Database (NED) is operated by the Jet Propulsion Laboratory, California Institute of Technology, under contract with NASA. This publication makes use of data products from 2MASS, funded by NASA and the U.S. National Science Foundation (NSF). IAUC/CBET were very useful. A.S.F. acknowledges support from an NSF STS Postdoctoral Fellowship (SES-1056580), an NSF Graduate Research Fellowship, and a NASA Graduate Research Program Fellowship. M.W.V. is funded by a grant from the U.S. National Science Foundation (AST-057475). R.P.K. acknowledges NSF Grants AST 12-11196, AST 09-097303, and AST 06-06772. M.M. acknowledges support in part from the Miller Institute at UC Berkeley, from Hubble Fellowship grant HST-HF-51277.01-A, awarded by STScI, which is operated by AURA under NASA contract

NAS5-26555, and from the NSF CAREER award AST-1352405. A.A.M. acknowledges support for this work by NASA from a Hubble Fellowship grant HST-HF-51325.01, awarded by STScI, operated by AURA, Inc., for NASA, under contract NAS 5-26555. Part of the research was carried out at the Jet Propulsion Laboratory, California Institute of Technology, under a contract with the National Aeronautics and Space Administration. A.S.F., R.P.K., and M.M. thank the Kavli Institute for Theoretical Physics at UC Santa Barbara, which is supported by the NSF through grant PHY05-51164. C.B. acknowledges support from the Harvard Origins of Life Initiative. Computations in this work were run on machines supported by the Harvard Astronomy Computation Facility, including the CfA Hydra cluster and machines supported by the Optical and Infrared Astronomy Division of the CfA. Other crucial computations were performed on the Harvard Odyssey cluster, supported by the Harvard FAS Science Division Research Computing Group. We thank the anonymous referee for a thorough and fair report that significantly helped to improve the paper.

Facilities: FLWO:2MASS, FLWO:PAIRITEL.

APPENDIX
NNT UNCERTAINTIES

We compute the estimated mean flux $\tilde{f}$ and uncertainty $\sigma_{\rm NNT}$ for a given night using the NNT host galaxy subtraction method in the following manner. For a night with $N_{\rm T}$ successful host galaxy template subtractions, we have $N_{\rm T}$ LC points with flux f_i each with corrected DoPHOT flux uncertainties $\sigma_{f_{{\rm do},i}}$, where $i = \{1, 2, \ldots, N_{\rm T}\}$ indexes the $N_{\rm T}$ subtractions that are implicitly summed over for every summation symbol Σ below. The estimated flux on this night is simply given by the weighted mean:

$$\tilde{f} = \frac{\Sigma f_i w_{f_i}}{\Sigma w_{f_i}}, \tag{5}$$

with weights given by $w_{f_i} = 1/\sigma^2_{f_{{\rm do},i}}$. We choose to conservatively estimate the uncertainty on $\tilde{f}$ using the error-weighted sample standard deviation of the $N_{\rm T}$ flux measurements, which has the advantage of being a function of both the input fluxes f_i and corrected DoPHOT flux errors $\sigma_{f_{{\rm do},i}}$ via the weights $w_{f_i} = 1/\sigma^2_{f_{{\rm do},i}}$, given by

$$\sigma_{\tilde{f}} = \sqrt{\frac{\Sigma w_{f_i}\left(f_i - \tilde{f}\right)^2}{\Sigma w_{f_i}}}. \tag{6}$$

However, to correct bias as a result of small sample sizes, which is appropriate here, since $N_{\rm T} \sim 3$–12, we refine Equation (6) and instead use an appropriate unbiased estimator of the weighted sample standard deviation, given by

$$\sigma_{\rm NNT} = \sqrt{\left[\frac{\Sigma w_{f_i}}{\left(\Sigma w_{f_i}\right)^2 - \Sigma w^2_{f_i}}\right] \Sigma w_{f_i}\left(f_i - \tilde{f}\right)^2}. \tag{7}$$

We use Equation (7) to compute our final NNT error estimate $\sigma_{\rm NNT}$ on the flux averaged over several subtractions on an individual night. To account for nights with only $N_{\rm T} = 1$ or 2 successful subtractions, we further implement a systematic error floor with a conservative magnitude cutoff as described in Section 4.2.1 (see Table 6).

REFERENCES

Amanullah, R., Goobar, A., Johansson, J., et al. 2014, ApJL, 788, L21
Astier, P., Guy, J., Pain, R., & Balland, C. 2011, A&A, 525, A7
Astier, P., Guy, J., Regnault, N., et al. 2006, A&A, 447, 31
Bailey, S., Aldering, G., Antilogus, P., et al. 2009, A&A, 500, L17
Barone-Nugent, R. L., Lidman, C., Wyithe, J. S. B., et al. 2012, MNRAS, 425, 1007
Barris, B. J., Tonry, J. L., Novicki, M. C., & Wood-Vasey, W. M. 2005, AJ, 130, 2272
Beaulieu, J. P., Bennett, D. P., Batista, V., et al. 2010, in ASP Conf. Ser. 430, Pathways towards Habitable Planets, ed. V. Coudé du Foresto, D. M. Gelino & I. Ribas (San Francisco, CA: ASP), 266
Becker, A. C., Rest, A., Miknaitis, G., Smith, R. C., & Stubbs, C. 2004, BAAS, 36, 1529
Becker, A. C., Silvestri, N. M., Owen, R. E., Ivezić, Ž., & Lupton, R. H. 2007, PASP, 119, 1462
Benetti, S., Meikle, P., Stehle, M., et al. 2004, MNRAS, 348, 261
Bertin, E., Mellier, Y., Radovich, M., et al. 2002, in ASP Conf. Ser. 281, Astronomical Data Analysis Software and Systems XI, ed. D. A. Bohlender, D. Durand & T. H. Handley (San Francisco, CA: ASP), 228
Betoule, M., Kessler, R., Guy, J., et al. 2014, A&A, 568, A22
Bianco, F. B., Modjaz, M., Hicken, M., et al. 2014, ApJS, 213, 19
Biscardi, I., Brocato, E., Arkharov, A., et al. 2012, A&A, 537, A57
Blondin, S., Mandel, K. S., & Kirshner, R. P. 2011, A&A, 526, A81
Blondin, S., & Tonry, J. L. 2007, ApJ, 666, 1024
Blondin, S., Matheson, T., Kirshner, R. P., et al. 2012, AJ, 143, 126
Bloom, J. S., Starr, D. L., Blake, C. H., Skrutskie, M. F., & Falco, E. E. 2006, in ASP Conf. Ser. 351, Astronomical Data Analysis Software and Systems XV, ed. G. Gabriel, C. Arviset, D. Ponz & S. Enrique (San Francisco, CA: ASP), 751
Boldt, L. N., Stritzinger, M. D., Burns, C., et al. 2014, PASP, 126, 324
Branch, D., Baron, E., Thomas, R. C., et al. 2004, PASP, 116, 903
Brown, P. J., Kuin, P., Scalzo, R., et al. 2014, ApJ, 787, 29
Bryngelson, G. 2012, PhD thesis, Clemson Univ.
Burns, C. R., Stritzinger, M., Phillips, M. M., et al. 2011, AJ, 141, 19
Burns, C. R., Stritzinger, M., Phillips, M. M., et al. 2014, ApJ, 789, 32
Campbell, H., D'Andrea, C. B., Nichol, R. C., et al. 2013, ApJ, 763, 88
Candia, P., Krisciunas, K., Suntzeff, N. B., et al. 2003, PASP, 115, 277
Carpenter, J. M. 2001, AJ, 121, 2851
Cartier, R., Hamuy, M., Pignata, G., et al. 2014, ApJ, 789, 89
Chary, R., Dickinson, M. E., Teplitz, H. I., Pope, A., & Ravindranath, S. 2005, ApJ, 635, 1022
Childress, M., Aldering, G., Aragon, C., et al. 2011, ApJ, 733, 3
Childress, M., Aldering, G., Antilogus, P., et al. 2013, ApJ, 770, 107
Chornock, R., Filippenko, A. V., Branch, D., et al. 2006, PASP, 118, 722
Clampin, M. 2011, Proc. SPIE, 8146, 814605
Cohen, M., Wheaton, W. A., & Megeath, S. T. 2003, AJ, 126, 1090
Conley, A., Carlberg, R. G., Guy, J., et al. 2007, ApJL, 664, L13
Conley, A., Sullivan, M., Hsiao, E. Y., et al. 2008, ApJ, 681, 482
Conley, A., Guy, J., Sullivan, M., et al. 2011, ApJS, 192, 1
Contreras, C., Hamuy, M., Phillips, M. M., et al. 2010, AJ, 139, 519
Cuadra, J., Suntzeff, N. B., Candia, P., Krisciunas, K., & Phillips, M. M. 2002, RMxAA, 27, 121
Cutri, R. M., Skrutskie, M. F., van Dyk, S., et al. 2003, 2MASS All Sky Catalog of Point Sources (The IRSA 2MASS All-Sky Point Source Catalog, NASA/IPAC Infrared Science Archive), http://irsa.ipac.caltech.edu/applications/Gator/
Davis, T. M., Hui, L., Frieman, J. A., et al. 2011, ApJ, 741, 67
Di Paola, A., Larionov, V., Arkharov, A., et al. 2002, A&A, 393, L21
Drout, M. R., Soderberg, A. M., Mazzali, P. A., et al. 2013, ApJ, 774, 58
Elias, J. H., Frogel, J. A., Hackwell, J. A., & Persson, S. E. 1981, ApJL, 251, L13
Elias, J. H., Matthews, K., Neugebauer, G., & Persson, S. E. 1985, ApJ, 296, 379
Elias-Rosa, N., Benetti, S., Cappellaro, E., et al. 2006, MNRAS, 369, 1880
Elias-Rosa, N., Benetti, S., Cappellaro, E., et al. 2008, MNRAS, 384, 107
Filippenko, A. V. 2005, in ASP Conf. Ser. 332, The Fate of the Most Massive Stars, ed. R. Humphreys & K. Stanek (San Francisco, CA: ASP), 33
Fixsen, D. J., Cheng, E. S., Gales, J. M., et al. 1996, ApJ, 473, 576
Folatelli, G., Phillips, M. M., Burns, C. R., et al. 2010, AJ, 139, 120
Foley, R. J., Brown, P. J., Rest, A., et al. 2010a, ApJL, 708, L61

Foley, R. J., McCully, C., Jha, S. W., et al. 2014a, ApJ, 792, 29
Foley, R. J., Van Dyk, S. D., Jha, S. W., et al. 2015, ApJL, 798, L37
Foley, R. J., Chornock, R., Filippenko, A. V., et al. 2009, AJ, 138, 376
Foley, R. J., Rest, A., Stritzinger, M., et al. 2010b, AJ, 140, 1321
Foley, R. J., Challis, P. J., Chornock, R., et al. 2013, ApJ, 767, 57
Foley, R. J., Fox, O. D., McCully, C., et al. 2014b, MNRAS, 443, 2887
Fransson, C., Ergon, M., Challis, P. J., et al. 2014, ApJ, 797, 118
Freedman, W. L., Burns, C. R., Phillips, M. M., et al. 2009, ApJ, 704, 1036
Freedman, W. L., & Carnegie Supernova Project 2005, in ASP Conf. Ser. 339, Observing Dark Energy, ed. S. C. Wolff & T. R. Lauer (San Francisco, CA: ASP), 50
Friedman, A. S. 2012, PhD thesis, Harvard Univ.
Frieman, J. A., Turner, M. S., & Huterer, D. 2008a, ARA&A, 46, 385
Frieman, J. A., Bassett, B., Becker, A., et al. 2008b, AJ, 135, 338
Frogel, J. A., Gregory, B., Kawara, K., et al. 1987, ApJL, 315, L129
Fruchter, A. S., & Hook, R. N. 2002, PASP, 114, 144
Ganeshalingam, M., Li, W., Filippenko, A. V., et al. 2010, ApJS, 190, 418
Garg, A., Stubbs, C. W., Challis, P., et al. 2007, AJ, 133, 403
Garnavich, P. M., Bonanos, A. Z., Krisciunas, K., et al. 2004, ApJ, 613, 1120
Gehrels, N. 2010, arXiv:1008.4936
Gerardy, C. L., Meikle, W. P. S., Kotak, R., et al. 2007, ApJ, 661, 995
Goldhaber, G., Groom, D. E., Kim, A., et al. 2001, ApJ, 558, 359
Goobar, A., & Leibundgut, B. 2011, ARNPS, 61, 251
Goobar, A., Johansson, J., Amanullah, R., et al. 2014, ApJL, 784, L12
Guy, J., Astier, P., Nobili, S., Regnault, N., & Pain, R. 2005, A&A, 443, 781
Guy, J., Astier, P., Baumont, S., et al. 2007, A&A, 466, 11
Guy, J., Sullivan, M., Conley, A., et al. 2010, A&A, 523, A7
Hamuy, M., Phillips, M. M., Suntzeff, N. B., et al. 1996, AJ, 112, 2438
Hamuy, M., Folatelli, G., Morrell, N. I., et al. 2006, PASP, 118, 2
Hernandez, M., Meikle, W. P. S., Aparicio, A., et al. 2000, MNRAS, 319, 223
Hicken, M., Garnavich, P. M., Prieto, J. L., et al. 2007, ApJL, 669, L17
Hicken, M., Wood-Vasey, W. M., Blondin, S., et al. 2009a, ApJ, 700, 1097
Hicken, M., Challis, P., Jha, S., et al. 2009b, ApJ, 700, 331
Hicken, M., Challis, P., Kirshner, R. P., et al. 2012, ApJS, 200, 12
Hicken, M. S. 2009, PhD thesis, Harvard Univ.
Hsiao, E. Y., Conley, A., Howell, D. A., et al. 2007, ApJ, 663, 1187
Jack, D., Hauschildt, P. H., & Baron, E. 2012, A&A, 538, A132
Jha, S., Branch, D., Chornock, R., et al. 2006a, AJ, 132, 189
Jha, S., Riess, A. G., & Kirshner, R. P. 2007, ApJ, 659, 122
Jha, S., Garnavich, P. M., Kirshner, R. P., et al. 1999, ApJS, 125, 73
Jha, S., Kirshner, R. P., Challis, P., et al. 2006b, AJ, 131, 527
Kasen, D. 2006, ApJ, 649, 939
Kattner, S., Leonard, D. C., Burns, C. R., et al. 2012, PASP, 124, 114
Kelly, P. L., Hicken, M., Burke, D. L., Mandel, K. S., & Kirshner, R. P. 2010, ApJ, 715, 743
Kessler, R., Becker, A. C., Cinabro, D., et al. 2009, ApJS, 185, 32
Kirshner, R. P. 2010, in Dark Energy: Observational and Theoretical Approaches, ed. P. Ruiz-Lapuente (Cambridge: Cambridge Univ. Press), 151
Kirshner, R. P. 2013, in IAU Symp. 281, ed. R. Di Stefano, M. Orio, & M. Moe (Cambridge: Cambridge Univ. Press), 1
Kirshner, R. P., Willner, S. P., Becklin, E. E., Neugebauer, G., & Oke, J. B. 1973, ApJL, 180, L97
Klein, C. R., & Bloom, J. S. 2014, arXiv:1404.4870
Kocevski, D., Modjaz, M., Bloom, J. S., et al. 2007, ApJ, 663, 1180
Krisciunas, K., Hastings, N. C., Loomis, K., et al. 2000, ApJ, 539, 658
Krisciunas, K., Phillips, M. M., & Suntzeff, N. B. 2004a, ApJL, 602, L81
Krisciunas, K., Prieto, J. L., Garnavich, P. M., et al. 2006, AJ, 131, 1639
Krisciunas, K., Phillips, M. M., Stubbs, C., et al. 2001, AJ, 122, 1616
Krisciunas, K., Suntzeff, N. B., Candia, P., et al. 2003, AJ, 125, 166
Krisciunas, K., Phillips, M. M., Suntzeff, N. B., et al. 2004b, AJ, 127, 1664
Krisciunas, K., Suntzeff, N. B., Phillips, M. M., et al. 2004c, AJ, 128, 3034
Krisciunas, K., Suntzeff, N. B., Phillips, M. M., et al. 2005a, AJ, 130, 350
Krisciunas, K., Garnavich, P. M., Challis, P., et al. 2005b, AJ, 130, 2453
Krisciunas, K., Garnavich, P. M., Stanishev, V., et al. 2007, AJ, 133, 58
Krisciunas, K., Marion, G. H., Suntzeff, N. B., et al. 2009, AJ, 138, 1584
Krisciunas, K., Li, W., Matheson, T., et al. 2011, AJ, 142, 74
Kromer, M., Fink, M., Stanishev, V., et al. 2013, MNRAS, 429, 2287
Lauer, T. R. 1999, PASP, 111, 227
Leggett, S. K., Currie, M. J., Varricatt, W. P., et al. 2006, MNRAS, 373, 781
Leloudas, G., Stritzinger, M. D., Sollerman, J., et al. 2009, A&A, 505, 265
Li, W., Filippenko, A. V., Chornock, R., et al. 2003, PASP, 115, 453
Li, W. D., Filippenko, A. V., Treffers, R. R., et al. 2000, in AIP Proc. 522, Cosmic Explosions: Tenth Astrophysics Conference, ed. S. S. Holt & W. W. Zhang (New York: AIP), 103
Mandel, K. S., Foley, R. J., & Kirshner, R. P. 2014, ApJ, 797, 75
Mandel, K. S., Narayan, G., & Kirshner, R. P. 2011, ApJ, 731, 120
Mandel, K. S., Wood-Vasey, W. M., Friedman, A. S., & Kirshner, R. P. 2009, ApJ, 704, 629
Margutti, R., Milisavljevic, D., Soderberg, A. M., et al. 2014, ApJ, 780, 21
Marion, G. H., Höflich, P., Gerardy, C. L., et al. 2009, AJ, 138, 727
Marion, G. H., Vinko, J., Kirshner, R. P., et al. 2014, ApJ, 781, 69
Marion, G. H., Sand, D. J., Hsiao, E. Y., et al. 2015, ApJ, 798, 39
Matheson, T., Kirshner, R. P., Challis, P., et al. 2008, AJ, 135, 1598
Matheson, T., Joyce, R. R., Allen, L. E., et al. 2012, ApJ, 754, 19
Maund, J. R., Wheeler, J. C., Wang, L., et al. 2010, ApJ, 722, 1162
McClelland, C. M., Garnavich, P. M., Galbany, L., et al. 2010, ApJ, 720, 704
McCully, C., Jha, S. W., Foley, R. J., et al. 2014a, Natur, 512, 54
McCully, C., Jha, S. W., Foley, R. J., et al. 2014b, ApJ, 786, 134
Meikle, W. P. S. 2000, MNRAS, 314, 782
Miknaitis, G., Pignata, G., Rest, A., et al. 2007, ApJ, 666, 674
Modjaz, M. 2007, PhD thesis, Harvard Univ.
Modjaz, M., Stanek, K. Z., Garnavich, P. M., et al. 2006, ApJL, 645, L21
Modjaz, M., Li, W., Butler, N., et al. 2009, ApJ, 702, 226
Modjaz, M., Blondin, S., Kirshner, R. P., et al. 2014, AJ, 147, 99
Narayan, G., Foley, R. J., Berger, E., et al. 2011, ApJL, 731, L11
Narayan, G. S. 2013, PhD thesis, Harvard Univ.
Nobili, S., Amanullah, R., Garavini, G., et al. 2005, A&A, 437, 789
Parrent, J. T., Thomas, R. C., Fesen, R. A., et al. 2011, ApJ, 732, 30
Pastorello, A., Mazzali, P. A., Pignata, G., et al. 2007a, MNRAS, 377, 1531
Pastorello, A., Taubenberger, S., Elias-Rosa, N., et al. 2007b, MNRAS, 376, 1301
Perlmutter, S., Gabi, S., Goldhaber, G., et al. 1997, ApJ, 483, 565
Perlmutter, S., Aldering, G., Goldhaber, G., et al. 1999, ApJ, 517, 565
Phillips, M. M. 1993, ApJL, 413, L105
Phillips, M. M. 2012, PASA, 29, 434
Phillips, M. M., Lira, P., Suntzeff, N. B., et al. 1999, AJ, 118, 1766
Phillips, M. M., Krisciunas, K., Suntzeff, N. B., et al. 2006, AJ, 131, 2615
Phillips, M. M., Li, W., Frieman, J. A., et al. 2007, PASP, 119, 360
Pignata, G., Benetti, S., Mazzali, P. A., et al. 2008, MNRAS, 388, 971
Plavchan, P., Jura, M., Kirkpatrick, J. D., Cutri, R. M., & Gallagher, S. C. 2008, ApJS, 175, 191
Prieto, J. L., Rest, A., & Suntzeff, N. B. 2006, ApJ, 647, 501
Quillen, A. C., Ciocca, M., Carlin, J. L., Bell, C. P. M., & Meng, Z. 2014, MNRAS, 441, 2691
Quimby, R. M. 2006, PhD thesis, Univ. Texas at Austin
Rest, A., Stubbs, C., Becker, A. C., et al. 2005, ApJ, 634, 1103
Rest, A., Scolnic, D., Foley, R. J., et al. 2014, ApJ, 795, 44
Riess, A. G., Press, W. H., & Kirshner, R. P. 1996, ApJ, 473, 88
Riess, A. G., Filippenko, A. V., Challis, P., et al. 1998, AJ, 116, 1009
Riess, A. G., Kirshner, R. P., Schmidt, B. P., et al. 1999, AJ, 117, 707
Riess, A. G., Macri, L., Casertano, S., et al. 2011, ApJ, 730, 119
Rowe, B., Hirata, C., & Rhodes, J. 2011, ApJ, 741, 46
Sahu, D. K., Tanaka, M., Anupama, G. C., et al. 2008, ApJ, 680, 580
Sanders, N. E., Soderberg, A. M., Foley, R. J., et al. 2013, ApJ, 769, 39
Schechter, P. L., Mateo, M., & Saha, A. 1993, PASP, 105, 1342
Schmidt, B. P., Suntzeff, N. B., Phillips, M. M., et al. 1998, ApJ, 507, 46
Schweizer, F., Burns, C. R., Madore, B. F., et al. 2008, AJ, 136, 1482
Scolnic, D., Rest, A., Riess, A., et al. 2014a, ApJ, 795, 45
Scolnic, D. M., Riess, A. G., Foley, R. J., et al. 2014b, ApJ, 780, 37
Silverman, J. M., Vinko, J., Kasliwal, M. M., et al. 2013, MNRAS, 436, 1225
Skrutskie, M. F., Cutri, R. M., Stiening, R., et al. 2006, AJ, 131, 1163
Sollerman, J., Lindahl, J., Kozma, C., et al. 2004, A&A, 428, 555
Stanishev, V., Goobar, A., Benetti, S., et al. 2007, A&A, 469, 645
Stritzinger, M., & Sollerman, J. 2007, A&A, 470, L1
Stritzinger, M., Hamuy, M., Suntzeff, N. B., et al. 2002, AJ, 124, 2100
Stritzinger, M., Burns, C. R., Phillips, M. M., et al. 2010, AJ, 140, 2036
Stritzinger, M. D., Phillips, M. M., Boldt, L. N., et al. 2011, AJ, 142, 156
Stritzinger, M. D., Hsiao, E., Valenti, S., et al. 2014, A&A, 561, A146
Stritzinger, M. D., Valenti, S., Hoeflich, P., et al. 2015, A&A, 573, A2
Taddia, F., Stritzinger, M. D., Phillips, M. M., et al. 2012, A&A, 545, L7
Taubenberger, S., Hachinger, S., Pignata, G., et al. 2008, MNRAS, 385, 75
Taubenberger, S., Benetti, S., Childress, M., et al. 2011, MNRAS, 412, 2735
Tominaga, N., Tanaka, M., Nomoto, K., et al. 2005, ApJL, 633, L97
Tonry, J. L., Schmidt, B. P., Barris, B., et al. 2003, ApJ, 594, 1
Turnbull, S. J., Hudson, M. J., Feldman, H. A., et al. 2012, MNRAS, 420, 447

Valentini, G., Di Carlo, E., Massi, F., et al. 2003, ApJ, 595, 779
Wang, L., Goldhaber, G., Aldering, G., & Perlmutter, S. 2003, ApJ, 590, 944
Wang, L., Strovink, M., Conley, A., et al. 2006, ApJ, 641, 50
Wang, X., Li, W., Filippenko, A. V., et al. 2008, ApJ, 675, 626
Wang, X., Li, W., Filippenko, A. V., et al. 2009, ApJ, 697, 380
Weinberg, D. H., Mortonson, M. J., Eisenstein, D. J., et al. 2013, PhR, 530, 87
Weyant, A., Wood-Vasey, W. M., Allen, L., et al. 2014, ApJ, 784, 105
Williams, A. J. 1997, PASA, 14, 208
Wood-Vasey, W. M., Miknaitis, G., Stubbs, C. W., et al. 2007, ApJ, 666, 694
Wood-Vasey, W. M., Friedman, A. S., Bloom, J. S., et al. 2008, ApJ, 689, 377
Yamanaka, M., Kawabata, K. S., Kinugasa, K., et al. 2009, ApJL, 707, L118